THEORETICAL STUDIES OF COHERENT OPTIC AND ACOUSTIC PHONONS IN GaN/InGaN HETEROSTRUCTURES

By

RONGLIANG LIU

A DISSERTATION PRESENTED TO THE GRADUATE SCHOOL
OF THE UNIVERSITY OF FLORIDA IN PARTIAL FULFILLMENT
OF THE REQUIREMENTS FOR THE DEGREE OF
DOCTOR OF PHILOSOPHY

UNIVERSITY OF FLORIDA

2004

To Linlin and Bryan.

ACKNOWLEDGMENTS

First and foremost I would like to thank Professor Christopher J. Stanton, my thesis advisor, for his guidance and encouragement throughout the course of my graduate study here at the University of Florida. Among many other things, he taught me how to construct and develop a theory from simple physical ideas and models. I also learned a lot from discussions with his postdocs and graduate students, especially from Dr. Gary Sanders and Yongke Sun.

I am honored and grateful to have Professor Peter J. Hirschfeld, Professor Jeffrey L. Krause, Professor Mark E. Law, Professor David H. Reitze, and Professor David B. Tanner to serve on my supervisory committee.

I want to thank the McLaughlin family for the dissertation fellowship.

Many thanks go to the secretaries of the Physics Department, in particular, Darlene Latimer and Donna Balkum, who gave me much indispensable assistance.

It is a great pleasure to have such wonderful friends as Bob and Janis Jackson. The times we are together are the happiest ones.

I want to thank my parents. They have gone through all kinds of hardships to raise me and my brothers. They always remind me to work hard, to waste nothing, and to be kind to other people.

I also want to thank my parents-in-law. They spent a year with me and my wife, which was one of the happiest times. They help me and my wife to take care of our little son Tianyue during our study.

Lastly, I want to thank my family, especially my wife for all the love, support, and fun she brings to me.

TABLE OF CONTENTS

page

LIST OF FIGURES

Abstract of Dissertation Presented to the Graduate School
of the University of Florida in Partial Fulfillment of the
Requirements for the Degree of Doctor of Philosophy

THEORETICAL STUDIES OF COHERENT OPTIC AND ACOUSTIC PHONONS IN GaN/InGaN HETEROSTRUCTURES

By

Rongliang Liu

May 2004

Chair: Christopher J. Stanton
Major Department: Physics

Coherent phonons are collective lattice oscillations which can periodically modulate the physical properties of the crystal. Three kinds of experimentally observed coherent phonons are discussed in this thesis. They are the coherent optical phonons in bulk semiconductors, the coherent acoustic phonons in GaN/InGaN multiple quantum wells and superlattices, and the propagating coherent phonon wavepackets in GaN/InGaN heterostructures and epilayers.

A phenomenological oscillator model is presented to explain the oscillating changes in the reflection of bulk semiconductors. The proper definition of the coherent phonon amplitude as the quantum-mechanical average of the phonon creation and annihilation operators constitutes the basis of the microscopic theory of the coherent phonons, which justifies the macroscopic oscillator model. The lattice displacement is related to the coherent phonon amplitude through Fourier transform. Since the laser wavelength is much larger than the lattice constant, the photoexcited carriers distribute uniformly and the the carrier density matrix has only the $q \approx 0$ Fourier component. As a result the coupling of the photoexcited carriers to the phonons leads to coherent optical phonons only.

The large piezoelectric fields due to the built-in strain in GaN/InGaN semiconductor superlattices or multiple quantum wells can be partially screened by the photoexcited carriers whose density has the same periodicity of the superlattice. In response the crystal relaxes to a new configuration which triggers the coherent acoustic phonon oscillations. The microscopically derived equation of motion for the coherent phonon amplitude can be mapped onto a one-dimensional wave equation for the lattice displacement which is called the string model. Based on the string model, the coherent control of the coherent acoustic phonons can be carried out theoretically.

The last kind is the coherent acoustic phonon wavepackets generated and detected in InGaN/GaN epilayers and heterostructures. We constructed a theoretical model that fits the experiments well and helps to deduce the strength of the coherent phonon wavepackets. This model shows that localized coherent phonon wavepackets are generated by the femtosecond pump laser in the epilayer near the surface. The wavepackets then propagate through a GaN layer changing the local index of refraction, primarily through the Franz-Keldysh effect, and as a result modulate the reflectivity of the probe beam.

CHAPTER 1
INTRODUCTION

Coherent phonons are collective lattice oscillations. When we shine a laser pulse with duration much shorter than the inverse of a lattice vibration frequency, the lattice mode will be excited coherently, i.e., there will be a large number of phonons in one mode with distinct phase relation [1]. This coherent phonon mode may behave like macroscopic oscillators. The nonzero time-dependent lattice displacement modulates the optical properties of the material through the dielectric constant, which can then be detected by changes in the reflection or transmission of a probe laser pulse.

There are basically two mechanisms for the generation of coherent phonons. One is the impulsive stimulated Raman scattering (ISRS) first observed by Fujimoto and Nelson et al. [2] They excited and detected coherent optic phonons by ISRS in α-perylene crystals in the temperature range 20–30 K. The impulsive stimulated Raman scattering can occur with no laser intensity threshold and with only one ultrafast laser pulse because the Stokes frequency is contained within the bandwidth of the incoming pulse. ISRS is a ubiquitous process through which coherent excitation lattice will happen whenever an ultrafast laser pulse passes through a Raman-active solid.

The other mechanism is the displacive excitation of coherent phonons (DECP). It is first proposed by Dresselhaus group [3]. DECP requires a significant absorption at the pump frequency so that an interband electron excitation occurs, while ISRS does not require absorption in the material [2, 4]. The electronic excitation makes the lattice to relax to a new quasiequilibrium configuration which then triggers coherent phonon oscillations.

With the development of ultra fast laser systems, the generation of coherent phonons in semiconductors, metals, and superconductors by femotosecond excitation of these materials has received considerable attention in recent years because of the potential applications such as non-destructive measurement and the theoretical interests. Shah has given a thorough review of the field [5].

This dissertation discusses three kinds of coherent phonons observed in the experiments:

1. the coherent optical phonons in the bulk semiconductor,
2. the coherent acoustic phonons in multiple quantum wells and superlattices,
3. and the propagating coherent phonons in GaN/InGaN heterostructures and epilayers.

I will present theories about these three kinds of coherent phonons and focus on the coherent acoustic phonons and the propagating coherent acoustic phonon wavepackets.

1.1 GaN/InGaN: Structures and Parameters

In 1995 Shuji Nakamura at Nichia Chemical Industries in Japan reported the successful development of LEDs based on GaN compounds [6]. Since then research and application interests have been intensified on this material.

The distribution of electrons in space and in momentum and their energy levels determine the electronic properties of a material. There are two implicit assumptions with regard to the electronic structure:

1. The electronic motion and nuclear motion are separable,
2. The electrons are independent of each other.

In principle neither of the assumptions is correct. The Hamiltonian of the system includes electron-electron interaction, nucleus-nucleus interaction, and electron-nucleus interaction. It is a complex many-body system.

But these assumptions are still practical approximations. They can be justified by first noticing that the ratio of the electron mass to nuclear mass (10^{-4}–10^{-5} in a typical solids) is so small that the fast moving electrons can adjust to the motion of nuclei almost instantly. And secondly, any one electron experiences an average potential exerted by all the other electrons.

In an infinite and perfect crystal, according to Bloch's theorem, the form of the eigenfunctions of the Schrödinger equation are the product of a plane wave and a periodic function with the same periodicity of the periodic potential. The energy levels are so close that they become bands. The methods for band structure calculations fall into two categories:

- Global methods to obtain the bands on the entire Brillouin zone,
- Local methods describing band structures near some special points (e.g., Γ point) inside the Brillouin zone.

Just a few examples of the first category include the tight binding method, the orthogonalized plane wave method, and the pseudopotential method. The perturbative $\mathbf{k}\cdot\mathbf{p}$ methods belongs to the second category. The methods for the band calculation can also be classified as empirical and ab intio. Most of the techniques are empirical which means that they need experiments to provide input parameters. Slater and Koster [7] were the first to use the tight binding method empirically.

The atomic structure of the elements making up GaN can be described as

$$\begin{aligned} \text{Ga} \quad & 1s^2 2s^2 2p^6 3s^2 3p^6 3d^1 \underbrace{4s^2 4p^1}, \\ \text{N} \quad & 1s^2 \underbrace{2s^2 2p^3}. \end{aligned}$$

The covalent bond between a gallium atom and a nitrogen atom is made by sharing the electrons, as a result, each atom ends up with four electrons. In the ground state these valence electrons occupies the s and p atomic orbitals. When the

gallium and nitrogen atoms come close to form a molecule, the s and p states form bonding and antibonding molecular orbitals, which are s bonding, p bonding, s antibonding, and p antibonding orbitals in the order of increasing energy. These molecule orbitals then evolve into the conduction and valence bands of the GaN semiconductor. Because of the specific ordering of the molecular orbitals, the bottom of the conduction band of a GaN semiconductor is s-type, while the top of the valence band is p-type, which allows electric-dipole transitions between the two bands according to the selection rules.

The band structure of the GaN semiconductor is shown schematically in Fig. 1–1. This four band model was originally developed by Kane for InSb [8], which is typical of direct gap III-V semiconductors. Near the zone center all four bands have parabolic dispersions. Two of the hole bands that are degenerate at $k = 0$ are know as the heavy hole (hh) and the light hole (lh) bands. The third split-off hole (so) band gets its name from the split-off to lower energy by the spin-orbit coupling.

In bulk semiconductors the energy gaps are temperature dependent which can be fitted to the empirical Varshni function [9]

$$E_g(T) = E_g(T = 0) - \frac{\alpha T^2}{T + \beta}, \tag{1.1}$$

where α and β are adjustable and called Varshni parameters. There are other functional forms [10] but the Varshni's is the most widely used one.

GaN is a wide-gap semiconductor. It usually appears in two crystal structures, the wurtzite GaN and the Zinc blende GaN. The wurtzite GaN is the more usual one of the two structures.

The following parameters we used are from Vurgaftman et al. [11] They gave a very rich set of references in the article.

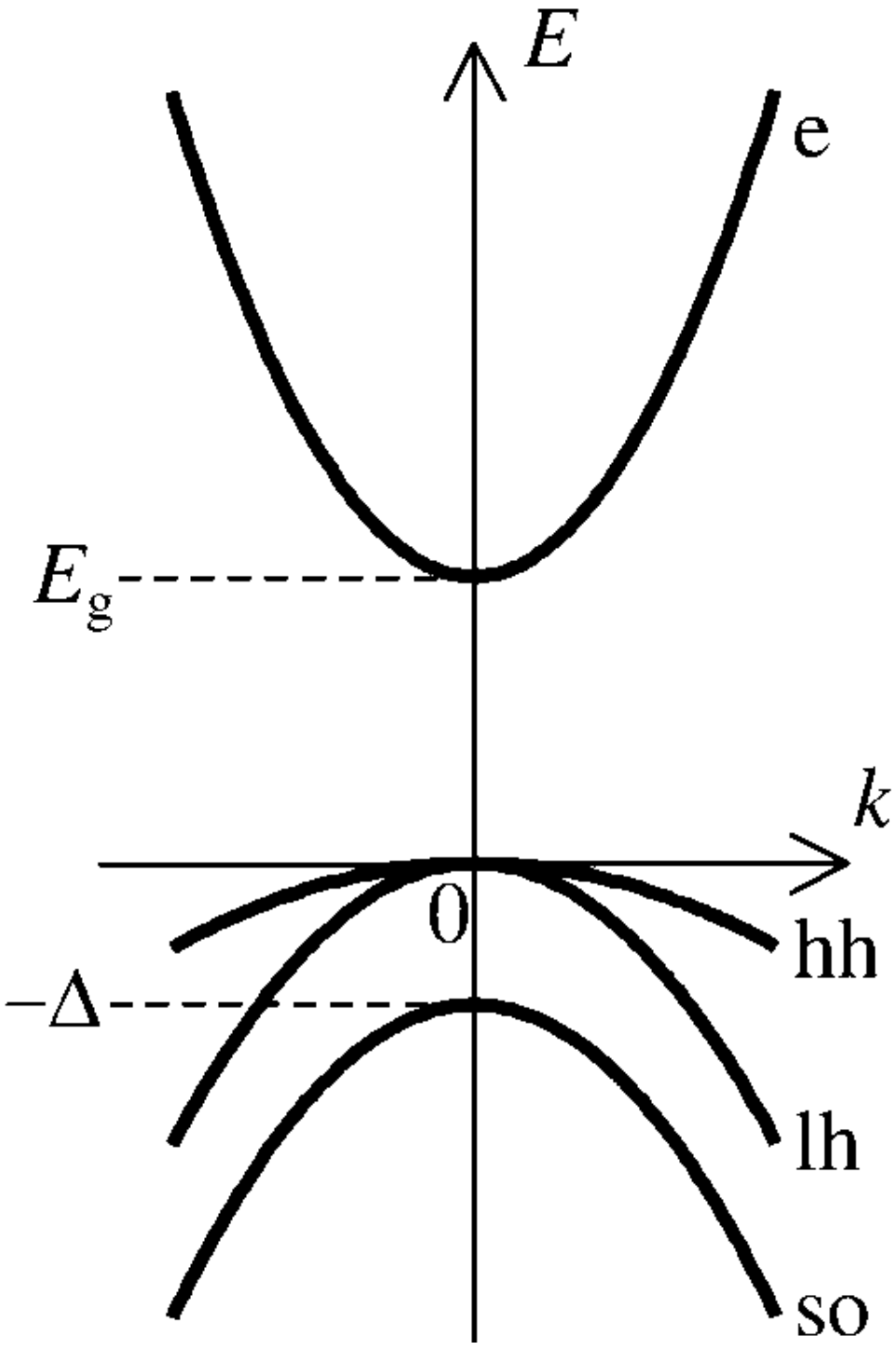

Figure 1–1: Schematic band diagram of a direct gap III-V semiconductor near the Brillouin zone center. The zero energy point is located at the top of the valence band, while $E = E_g$ corresponds to the bottom of the conduction band. The conduction band is an electron (e) band, while the valence bands are: the heavy hole (hh) band, the light hole (lh) band, and the split-off hole (so) band.

Table 1–1: Recommended Band Structure Parameters for wurtzite GaN and InN (for comparison we also listed parameters for GaAs.)

Parameters	GaN	InN	GaAs
$a_{\rm lc}$ (Å) at $T = 300$ K	3.189	3.545	5.653
$c_{\rm lc}$ (Å) at $T = 300$ K	5.185	5.703	-
E_g (eV)	3.507	1.994	1.519(Γ)
α (meV/K)	0.909	0.245	0.5405(Γ)
β (K)	830	624	204(Γ)
$\Delta_{\rm cr}$ (eV)	0.019	0.041	-
$\Delta_{\rm so}$ (eV)	0.014	0.001	0.341
$m_e^{\parallel}$ (eV)	0.20	0.12	0.067(Γ)
$m_e^{\perp}$ (eV)	0.20	0.12	0.067(Γ)
E_P (eV)	14.0	14.6	28.8
c_{11} (GPa)	390	223	1221
c_{12} (GPa)	145	115	566
c_{13} (GPa)	106	92	-
c_{33} (GPa)	398	224	-
c_{44} (GPa)	105	48	600
e_{13} (GPa)	-0.35	-0.57	-
e_{33} (GPa)	1.27	0.97	-
C_L [001] (10^3 m/s)	8.04	5.17	-
C_L [100] (10^3 m/s)	7.96	5.28	4.73
C_T [001] (10^3 m/s)	4.13	1.21	-
C_T [100] (10^3 m/s)	4.13	1.21	3.35
C_T [010] (10^3 m/s)	6.31	2.51	-

For ternary alloys, the dependence of the energy gap on alloy composition is assumed to fit the following quadratic form,

$$E_g(A_xB_{1-x}) = xE_g(A) + (1-x)E_g(B) - x(1-x)C, \tag{1.2}$$

where the bowing parameter C represents the deviation from the linear interpolation between the two binaries A and B. In the case of $In_xGa_{1-x}N$, C is about 3.0 eV. For other parameters, one usually linearly interpolate between the values of two binaries if there are no generally accepted experimental data.

The [001] longitudinal acoustic wave speed of $In_xGa_{1-x}N$ For $x = 0.08$ is about 7800 m/s. The difference of the [001] LA mode speed between GaN and $In_xGa_{1-x}N$ is very small when the In component x is small. For $x = 0.08$ this difference is less than 3%. The reflectivity due to the different sound speeds between GaN and $In_xGa_{1-x}N$ is given by

$$r = \frac{C_s - C_s'}{C_s + C_s'}, \tag{1.3}$$

where C_s and C_s' are sound speeds in GaN and $In_xGa_{1-x}N$ respectively. For $x = 0.08$, r is approximately 0.014 and the reflection constant $R = |r|^2$ is even smaller on the order of 10^{-4}.

1.2 The Dynamics of Photoexcited Carriers and Phonons

Ultrafast femtosecond lasers are indispensable powerful tools for studying the dynamical behavior of photoexcited electrons and holes in semiconductors and other condensed matter systems. These lasers are ideal for obtaining a *snapshot* of the nonequilibrium photoexcited carriers and studying the scattering processes because the scattering time of carriers in semiconductors is about tens to hundreds of femtoseconds.

As mentioned in the last section the periodicity of the semiconductor lattice leads to energy band structure, which forms the basis of understanding most of the optical phenomena in a semiconductor.

Electrons can be excited into the conduction band creating holes in the valence band. The periodicity of the semiconductor lattice also allows the description of the quantized vibrational modes of the lattice in terms of phonon dispersion relations. The dynamics of electrons, holes, and phonons is influenced by their interaction with each other, as well as with defects and interfaces of the system.

Carrier-carrier scattering determines the exchange of energy between carriers and is primarily responsible for the thermalization of photoexcited non-thermal carriers. Carrier-phonon interactions play a major role in the exchange of energy and momentum between carriers and the lattice. Optical phonons interact with carriers through polar coupling and non-polar optical deformation potential, while acoustic phonons interact with carriers through deformation potential and the piezoelectric potential.

After a semiconductor in thermodynamic equilibrium is excited by an ultrashort laser pulse, it undergoes several stages of relaxation before it returns once again to the thermodynamic equilibrium. The carrier relaxation can be classified into four temporally overlapping regimes.

First there is the *coherent stage*. The ultrashort laser pulse creates excitation with a well-defined phase relationship within them and with the laser electromagnetic field. The scattering processes that destroy the coherence are extremely fast so pico- and femtosecond techniques are required to study the coherent regime in semiconductors. The dynamics are described by the semiconductor Bloch equations [12].

Second is the *thermalization stage*. After the destruction of coherence through dephasing the distribution of the excitation is very likely to be non-thermal; that is, the distribution function cannot be characterized by an effective temperature. This regime provides information about various carrier-carrier scattering processes

that bring the non-thermal distribution to a hot, thermalized distribution. This relaxation stage is governed by the Boltzmann transport equation (BTE) [13].

Third is the *hot carrier* or the *carrier cooling stage*. In this regime the carrier distribution is characterized by an effective temperature. The temperature is usually higher than the lattice temperature and may be different for different sub-systems. Investigation of hot carrier regime focuses on the rate of cooling of carriers to the lattice temperature and leads to information concerning various carrier-phonon and phonon-phonon scattering processes.

At the end of the carrier cooling regime, all the carriers and phonons are in equilibrium with each other and can be described by the same temperature. However, there is still an excess of electrons and holes compared to the thermodynamic equilibrium. These excess electron-hole pairs recombine and return the semiconductor to the thermodynamic equilibrium. This is the *recombination stage*.

It should be emphasized that many physical processes in the different regimes can overlap. For example, the processes that destroy coherence may also contribute to the thermalization of carrier distribution functions.

1.3 Experiment Setup For Coherent Phonons

There are many techniques developed to investigate the optical properties of semiconductors using ultrafast lasers, which include pump-probe spectroscopy, four-wave mixing spectroscopy, luminescence spectroscopy, and terahertz spectroscopy. Figure 1–2 shows a schematic setup for a general two laser beam pump-probe experiment.

Pump-probe spectroscopy is the most common setup for the generation and detection coherent phonons. The light source is usually a Titanium:sapphire mode-locked ultrafast laser with a pulse width ranging from a few femtoseconds to hundreds of femtoseconds and a wavelength around 800 nm, the frequency of which can be doubled if photons of higher energy are needed. The light beam from

the ultrafast laser is splitted into a pump and a probe. The time delay between the pump and the probe is controlled by the optical path of the probe. The pump laser pulse excites carriers and coherent phonons in the semiconductor sample, which results in the change in the dielectric function of the material. By measuring differential reflection or transmission which represent changes in the reflected or transmitted probe pulse energy between the pump on and pump off at different time delays, one obtains the response of the dielectric function to the light due to the carriers and lattice vibrations in the material.

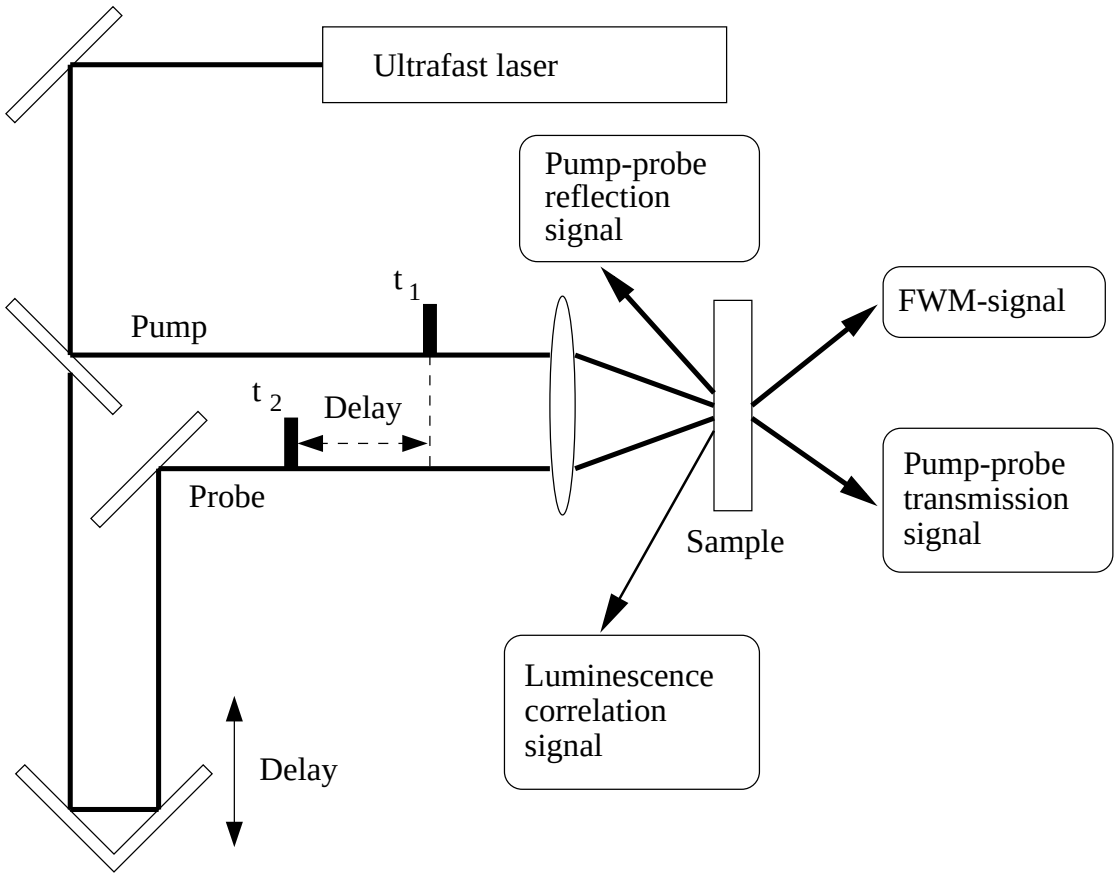

Figure 1–2: Schematic setup for a two-beam nonlinear experiment. It can be used for pump-probe transmission or reflection spectroscopy, four-wave-mixing spectroscopy, or luminescence correlation spectroscopy.

CHAPTER 2
DIPOLE OSCILLATOR MODEL

The description of the interaction between light and matter falls into one of three categories: the classical, the semiclassical, and the fully quantum. In classical models we treat both the light and matter as classical objects that behave according to the laws of classical physics. In semiclassical models we apply quantum mechanics to describe the matter, but treat light as a classical electromagnetic wave. The fully quantum approach belongs to the realm of quantum optics, where both light and matter are treated as quantum objects. When we speak of a light beam in terms of photons and draw Feynman diagram to depict the interaction processes, we are using the fully quantum approach implicitly, even though quantitatively we may have treated the light classically.

The dipole oscillator is a typical example of classical models. It is the basic starting point for understanding the effects due to carriers and phonons. The proper comprehension of this simple classical model is indispensable in appreciating more complicated models.

In the first section of this chapter I will give a general introduction to the optical processes occurring when a light beam is incident on an optical medium and their quantization. The main purpose is to define the notation and collect together the relationships between the optical coefficients.

2.1 Optical Processes and Optical Coefficients

The wide range of optical processes observed in a semiconductor can be organized into several groups of general phenomena. At the macroscopic level all the optical phenomena can be described quantitatively by a small number of parameters or optical coefficients that characterize the properties of the semiconductor.

2.1.1 Classification of Optical Processes

When a light beam is shined on a semiconductor, some of the light is reflected from the front surface, some enters the semiconductor and propagates through it, and some comes out from the back end of the semiconductor. Thus, the intuitive and simplest classification of optical processes is *reflection*, *propagation*, and *transmission*. The light propagation phenomena can be further classified into *refraction*, *absorption*, *luminescence*, and *scattering*.

Refraction happens when a light beam travels obliquely from one optical medium to another, e.g., from free space into a semiconductor, in which its speed changes, e.g., the speed of the light becomes smaller in the semiconductor than in free space. The direction of the light beam changes according to Snell's law of refraction.

Absorption describes the loss of intensity when a beam of light passes through a semiconductor. There are two kinds of absorption processes: *scattering*, which will be discussed below, and absorption of photons by atoms or molecules in the semiconductor. Absorption and transmission are related because only the unabsorbed light will be transmitted.

Luminescence is the spontaneous emission of light by atoms of a semiconductor making transitions from an excited state to the ground state or to another excited state of lower energy. Depending on the causes of excitation, luminescence could be *photoluminescence* if the excitation is caused by a photon, *electroluminescence* if it is an electron, *chemiluminescence* if it is a chemical reaction, etc. *Phosphorescence* or *fluorescence* depends on whether the luminescence persists significantly after the exciting causes is removed. There is some arbitrariness in this distinction, usually a persistence of more than 10 ns is treated as phosphorescence. Thus, photoluminescence accompanies the propagation of light in an absorbing medium. The emitted light beams are in all directions and the frequencies are

different from the incoming beam. The spontaneous emission takes a characteristic amount of time. The excitation energy can dissipate as heat before the radiative re-emission. As a result the efficiency of the luminescence is closely related to the dynamics of the de-excitation mechanism in semiconductors.

Scattering occurs when a light beam is deflected by atoms or molecules in a semiconductor. If the frequency of the scattered light remains unchanged, it is called an *elastic* scattering; otherwise it is called an *inelastic* scattering. The total number of photons does not change in either kind of scattering, but the number in the forward direction decreases because some photons are being redirected into other directions. So scattering also has the attenuating effect as absorption does.

There are other phenomena such as frequency doubling if the intensity of the propagating light beam is very high. These phenomena are described by nonlinear optics.

2.1.2 Quantization of Optical Processes

The Reflection and transmission of a beam of light are described by the *Reflectance* or *reflection coefficient* R and the *transmittance* or *transmission coefficient* T respectively. Reflectance R is defined as the ratio of the reflected power to the incident power on the surface, while transmittance is the ratio of the transmitted power to the incident power. If there is no absorption or scattering, we must have $R + T = 1$ from energy conservation.

The propagation of the light through a semiconductor can be characterized by the *refractive index* n and the *absorption coefficient* α. The refractive index is the ratio of the speed of light in vacuum c to the speed of light in the semiconductor v,

$$n = \frac{c}{v}. \tag{2.1}$$

The frequency dependence of the refractive index is called *dispersion*.

The absorption coefficient α is defined as the fraction of power absorbed after a light beam travels a unit length of the medium. Suppose the light beam travels in the z direction, and denote the intensity at position z as $I(z)$, then the decrease of the intensity in a thin slice of thickness $\mathrm{d}z$ is given by $\mathrm{d}I = -\alpha \mathrm{d}z \times I(z)$. After integrating both sides of the above equation, we obtain Beer's law

$$I(z) = I_0\, e^{-\alpha z}, \tag{2.2}$$

where I_0 is the light intensity at position $z = 0$. The absorption coefficient is strongly related to the frequency of the incident light, which is why materials may absorb the light of one color but not another.

In an absorbing medium the refraction and absorption can also be described by a single quantity, the complex refractive index $\tilde{n}$, which is defined as

$$\tilde{n} = n + i\kappa. \tag{2.3}$$

The real part of $\tilde{n}$, i.e. n, is the same as the refractive index defined in Eq. (2.1). The imaginary part of $\tilde{n}$, i.e. κ, is called the *extinction coefficient* and is related to the absorption coefficient.

We can derive the relationship between α and κ by considering a plane electromagnetic wave propagating through an absorbing medium. Let the z axis be the direction of propagation and let the electric field be given by

$$\mathcal{E}(z,t) = \mathcal{E}_0 e^{i(kz-\omega t)}, \tag{2.4}$$

where k is the wave vector and ω is the angular frequency, which are related in a non-absorbing medium through

$$k = \frac{2\pi}{\lambda/n} = \frac{n\omega}{c}. \tag{2.5}$$

Here λ is the vacuum wavelength of the light. Eq. (2.5) can be generalized to the case of an absorbing medium by way of the complex refractive index,

$$k = \tilde{n}\frac{\omega}{c} = (n + i\kappa)\frac{\omega}{c}. \tag{2.6}$$

On substituting Eq. (2.6) into Eq. (2.16) and after rewriting Eq. (2.16), we obtain

$$\mathcal{E}(z,t) = \mathcal{E}_0 e^{-\kappa\omega z/c} e^{i(\omega n z/c - \omega t)}. \tag{2.7}$$

Comparing Beer's law in Eq. (2.2) with the intensity of the light wave, which is proportional to the square of the electric field, i.e. $I \propto \mathcal{E}\mathcal{E}^*$, we obtain

$$\alpha = \frac{2\kappa\omega}{c} = \frac{4\pi\kappa}{\lambda}, \tag{2.8}$$

which shows that the absorption coefficient α at a given wavelength is proportional to the extinction coefficient κ.

We still have one last optical coefficient to introduce, that is the relative dielectric constant ϵ. Sometimes it is simply called the dielectric constant or dielectric function. The relationship between the refractive index and the dielectric constant is a standard result derived from Maxwell's equations (cf. any electrodynamics textbook, e.g. Jackon's [14]),

$$n = \sqrt{\epsilon}. \tag{2.9}$$

Corresponding to the complex refractive index $\tilde{n}$, we have the complex dielectric constant,

$$\tilde{\epsilon} = \epsilon_1 + i\epsilon_2 = \tilde{n}^2, \tag{2.10}$$

where ϵ_1 is the real part of the complex dielectric constant and ϵ_2 the imaginary part. The relationships between the real and imaginary parts of $\tilde{n}$ and $\tilde{\epsilon}$ are not difficult to derive from Eq. (2.10). They are

$$\epsilon_1 = n^2 - \kappa^2, \tag{2.11a}$$

$$\epsilon_2 = 2n\kappa, \tag{2.11b}$$

and

$$n = \frac{1}{\sqrt{2}}\left(\epsilon_1 + \sqrt{\epsilon_1^2 + \epsilon_2^2}\right)^{1/2}, \tag{2.12a}$$

$$\kappa = \frac{1}{\sqrt{2}}\left(-\epsilon_1 + \sqrt{\epsilon_1^2 + \epsilon_2^2}\right)^{1/2}. \tag{2.12b}$$

Thus, we can calculate n and κ from ϵ_1 and ϵ_2, and *vice versa*. In the weakly absorbing case, i.e. $\kappa \ll n$, Equation (2.12) can be simplified to

$$n = \sqrt{\epsilon_1}, \tag{2.13}$$

$$\kappa = \frac{\epsilon_2}{2n}. \tag{2.14}$$

2.2 The Dipole Oscillator Model

The originator of the classical dipole oscillator model is Lorentz, so it is also called the *Lorentz model*. In this model, the light is treated as electromagnetic waves and the atoms or molecules are treated as classical dipole oscillators. There are different kinds of oscillators. The atomic oscillator at optical frequencies is due to the oscillations of the bound electrons within the atoms. The vibrations of charged atoms within the crystal lattice give rise to the vibrational oscillators in the infrared spectral region. There are also free electron oscillators in metals. Based on the model we can calculate the frequency dependence of the complex dielectric function and obtain the reflection and the transmission coefficient.

2.2.1 The Atomic Oscillator

Let us consider first the atomic oscillator in the context of a light wave interacting with an atom with a single resonant frequency ω_0 due to a bound electron. We assume the mass of the nucleus m_n is much greater than the mass of the electron m_0 so that the motion of the nucleus can be ignored, then the

displacement x of the electron is governed by the classical equation of motion,

$$m_0\frac{\mathrm{d}^2x}{\mathrm{d}t^2}+m_0\gamma\frac{\mathrm{d}x}{\mathrm{d}t}+m_0\omega_0^2x=-e\mathcal{E}, \tag{2.15}$$

where γ is the damping constant and e is the charge of an electron . The electric field $\mathcal{E}$ of a monochromatic light wave of angular frequency ω is given by

$$\mathcal{E}(t)=\mathcal{E}_0e^{-i\omega t}. \tag{2.16}$$

If we substitute Eq. (2.16) into Eq. (2.15) and look for solutions of the form $x(t)=x_0e^{-i\omega t}$, then we have

$$x_0=\frac{-e\mathcal{E}_0/m_0}{\omega_0^2-\omega^2-i\gamma\omega}. \tag{2.17}$$

The resonant polarization due to the displacement of the electrons from their equilibrium position is

$$\mathcal{P}_\mathrm{r}=-Nex=\frac{Ne^2}{m_0}\frac{1}{\omega_0^2-\omega^2-i\gamma\omega}\mathcal{E}, \tag{2.18}$$

where N is the number of atoms per unit volume.

The electric displacement $\mathcal{D}$, the electric field $\mathcal{E}$, and the polarization $\mathcal{P}$ are related through

$$\mathcal{D}=\epsilon_0\epsilon\mathcal{E}=\epsilon_0\mathcal{E}+\mathcal{P}. \tag{2.19}$$

We split the total polarization into the resonant term $\mathcal{P}_\mathrm{r}$ we discussed above and a non-resonant background term $\mathcal{P}_\mathrm{b}=\epsilon_0\chi\mathcal{E}$, then from Eq. (2.19) we can obtain the complex dielectric constant

$$\epsilon(\omega)=1+\chi+\frac{Ne^2}{\epsilon_0m_0}\frac{1}{\omega_0^2-\omega^2-i\gamma\omega}. \tag{2.20}$$

We can also write this complex dielectric constant in terms of its real and imaginary parts:

$$\epsilon_1(\omega)=1+\chi+\frac{Ne^2}{\epsilon_0m_0}\frac{\omega_0^2-\omega^2}{(\omega_0^2-\omega^2)^2+(\gamma\omega)^2}, \tag{2.21}$$

$$\epsilon_2(\omega) = \frac{Ne^2}{\epsilon_0 m_0} \frac{\gamma\omega}{(\omega_0^2 - \omega^2)^2 + (\gamma\omega)^2}. \tag{2.22}$$

We define two dielectric constant in the low and high frequency limits,

$$\epsilon(\omega = 0) \equiv \epsilon_s = 1 + \chi + \frac{Ne^2}{\epsilon_0 m_0 \omega_0^2}, \tag{2.23}$$

and

$$\epsilon(\omega = \infty) \equiv \epsilon_\infty = 1 + \chi. \tag{2.24}$$

Thus, we have

$$\epsilon_s - \epsilon_\infty = \frac{Ne^2}{\epsilon_0 m_0 \omega_0^2} = \frac{\omega_p^2}{\omega_0^2}, \tag{2.25}$$

where $\omega_p^2 = \frac{Ne^2}{\epsilon_0 m_0}$ is called the plasma frequency.

Close to resonance, where $\omega \approx \omega_0 \gg \gamma$ and $\omega_0^2 - \omega^2 \approx 2\omega_0\Delta\omega$ with $\Delta\omega = \omega - \omega_0$ as the detuning from ω_0, we can rewrite the real and imaginary parts of the complex dielectric constant as

$$\epsilon_1(\Delta\omega) = \epsilon_\infty - (\epsilon_s - \epsilon_\infty)\frac{2\omega_0\Delta\omega}{4\Delta\omega^2 + \gamma^2}, \tag{2.26}$$

$$\epsilon_2(\Delta\omega) = (\epsilon_s - \epsilon_\infty)\frac{\omega_0\gamma}{4\Delta\omega^2 + \gamma^2}. \tag{2.27}$$

The frequency dependence of ϵ_1 and ϵ_2 is called Lorentzian named after the originator of the dipole oscillator model. The imaginary part ϵ_2 is strongly peaked with a maximum value at ω_0 and a full width γ at half maximum. The real part ϵ_1 first gradually rises from the low frequency value ϵ_s when we approach ω_0 from below. After reaching a peak at $\omega_0 - \gamma/2$, it falls sharply, going through a minimum at $\omega_0 + \gamma/2$, then rising again to the high frequency limit ϵ_∞. The frequency range over which these drastic changes occur is determined by γ.

2.2.2 The Free Electron Oscillator

Both metals and doped semiconductors contain large densities of free carriers such as electrons or holes. Both of them can be treated as plasmas, i.e. a neutral gas of heavy ions and light electrons, because they contain equal number of positive

ions and free electrons. Unlike bound electrons, the free electrons have no restoring force acting on them. The free electron model of metals was first proposed by Drude in 1900. The Drude model treats the valence electrons of the atoms as free electrons. A detailed discussion of the Drude model can be found in e.g. Ashcroft & Mermin [15]. These free electrons accelerate in an electric field and undergo collisions with a characteristic scattering time τ. The free electron oscillator is actually a combination of the *Drude model* of free electron conductivity and the Lorentz dipole oscillator model.

The equation of motion for electrons in the Drude model is given by

$$\frac{\mathrm{d}\mathbf{p}}{\mathrm{d}t} = -\frac{\mathbf{p}}{\tau} - e\mathcal{E}. \tag{2.28}$$

Comparing it with the equation of motion for the displacement x of a free electron oscillator

$$m_0\frac{\mathrm{d}^2x}{\mathrm{d}t^2} + m_0\gamma\frac{\mathrm{d}x}{\mathrm{d}t} = -e\mathcal{E}, \tag{2.29}$$

we have a relation between the damping constant and scattering time

$$\gamma = \frac{1}{\tau}. \tag{2.30}$$

We can solve Eq. (2.29) in the same way as we did in the atomic oscillator and obtain the complex dielectric constant for the free electron oscillators,

$$\epsilon(\omega) = 1 - \frac{Ne^2}{\epsilon_0 m_0}\frac{1}{\omega^2 + i\gamma\omega}, \tag{2.31}$$

where we did not take into account the background polarization. If we define

$$\omega_p^2 = \frac{Ne^2}{\epsilon_0 m_0}, \tag{2.32}$$

where ω_p is known as the *plasma frequency*, we can write Eq. (2.31) in a more concise form

$$\epsilon(\omega) = 1 - \frac{\omega_p^2}{\omega^2 + i\gamma\omega}. \tag{2.33}$$

The AC conductivity $\sigma\omega$ in Drude model is obtained by solving Eq. (2.28),

$$\sigma(\omega) = \frac{\sigma_0}{1 - i\omega\tau}, \tag{2.34}$$

where $\sigma_0 = Ne^2\tau/m_0$ is the DC conductivity. Comparing Eq. (2.31) and (2.34), we have

$$\epsilon(\omega) = 1 + \frac{i\sigma(\omega)}{\epsilon_0\omega}, \tag{2.35}$$

which tells us that optical measurements of the dielectric constant are equivalent to AC conductivity measurements. Again we can split the dielectric constant into its real and imaginary parts as

$$\epsilon_1 = 1 - \frac{\omega_p^2\tau^2}{1 + \omega^2\tau^2}, \tag{2.36}$$

$$\epsilon_2 = \frac{\omega_p^2\tau}{\omega(1 + \omega^2\tau^2)}. \tag{2.37}$$

The plasma frequency ω_p typically lies in the visible or ultraviolet spectral region, which corresponds to $\omega_p > 10^{15}$ sec^{-1}. The mean free collision time for electrons in metals is typically $\tau \approx 10^{-14}$ sec. So for metals in the region of plasma frequency, $\omega\tau \gg 1$.

2.2.3 The Vibrational Oscillator

The atoms in a crystal solid vibrate at characteristic frequencies determined by the phonon modes of the crystal. The resonant frequencies of phonons usually occur in the infrared spectral region, which results in strong absorption and reflection of light. Since a longitudinal optical (LO) phonon has no effect on a light wave because the longitudinal electric field induced by an LO phonon is perpendicular to that of the light wave, we will consider the interaction between an electromagnetic wave and a transverse optical (TO) phonon, which is easily visualized by a linear chain. The chain is made up of a series of unit cells with each cell containing a positive ion of mass m_+ and a negative ion of mass m_-. If we

assume the waves propagate in the z direction and the displacement of the positive and negative ions in a TO mode is denoted by x_+ and x_- respectively, then the equations of motion are given by

$$m_+\frac{\mathrm{d}^2x_+}{\mathrm{d}t^2} = -K(x_+ - x_-) + q\mathcal{E}, \tag{2.38a}$$

$$m_-\frac{\mathrm{d}^2x_-}{\mathrm{d}t^2} = -K(x_- - x_+) - q\mathcal{E}, \tag{2.38b}$$

where K is the restoring constant and $\pm q$ is the effective charge per ion. Combining equations of motion (2.38a) and (2.38b), we obtain

$$\mu\frac{\mathrm{d}^2x}{\mathrm{d}t^2} = -Kx + q\mathcal{E}, \tag{2.39}$$

where μ is the reduced mass given by $1/\mu = 1/m_+ + 1/m_-$ and $x = x_+ - x_-$ is the relative displacement of the positive and negative ions within the same cell. We can introduce a phenomenological damping constant γ to account for the finite life time of a phonon mode. Following the same procedures as the forgoing two subsections, we can solve the motion of equation for x to obtain the dielectric constant

$$\epsilon(\omega) = 1 + \chi + \frac{Nq^2}{\epsilon_0\mu}\frac{1}{\omega_{\mathrm{TO}}^2 - \omega^2 - i\gamma\omega}, \tag{2.40}$$

where χ is the non-resonant background susceptibility and N is the number of unit cells per unit length. Similar to the definitions of ϵ_s and ϵ_∞ in subsection 2.2.1 we can also write the dielectric constant as

$$\epsilon(\omega) = \epsilon_\infty + (\epsilon_s - \epsilon_\infty)\frac{\omega_{\mathrm{TO}}^2}{\omega_{\mathrm{TO}}^2 - \omega^2 - i\gamma\omega}. \tag{2.41}$$

As we said before usually an LO phonon does not interact with light waves, but in special cases it will. In a medium without free charges, Gauss's law gives

$$\nabla\cdot\mathcal{D} = \nabla\cdot(\epsilon_0\epsilon\mathcal{E}) = 0. \tag{2.42}$$

There are two ways to satisfy the equation, one of them is a transverse wave with$\mathbf{k} \cdot \mathcal{E} = 0$. The other is longitudinal waves but with $\epsilon = 0$. In a weakly damped system we can set $\gamma = 0$. There is a special frequency called ω_{LO} at which the dielectric constant is zero and the longitudinal modes interact with light waves. We can solve Eq. (2.41) to obtain the so called Lyddane-Sachs-Teller (LST) relationship

$$\frac{\omega_{\mathrm{LO}}^2}{\omega_{\mathrm{TO}}^2} = \frac{\epsilon_s}{\epsilon_\infty}. \tag{2.43}$$

The dielectric constant is below zero when $\omega_{\mathrm{TO}} < \omega < \omega_{\mathrm{LO}}$, which leads to 100% reflectance so no light can propagate into the medium. The frequency range between ω_{TO} and ω_{LO} is called the *restrahlen* (German word for "residual rays") band.

2.2.4 A Series Of Oscillators

In a semiconductor, the atomic oscillator, the free electron oscillator, and the lattice vibrational oscillator may be all present. For a specific type of oscillator there can be several different resonant frequencies. The dielectric constant due to these multiple oscillators can be written as

$$\epsilon(\omega) = 1 + \frac{Ne^2}{\epsilon_0 m_0} \sum_j \frac{f_j}{\omega_j^2 - \omega^2 - i\gamma_j \omega}, \tag{2.44}$$

where ω_j and γ_j are the frequency and damping constant of a particular oscillator. The phenomenological parameter f_j is called the *oscillator strength*, which has no explanation in classical physics. In quantum physics the oscillator strengths satisfy the sum rule

$$\sum_j f_j = 1. \tag{2.45}$$

In classical physics we just take $f_j = 1$ for each oscillator.

2.3 Reflectance And Transmission Coefficient

For normal incidence the reflectance is given by

$$R = \left|\frac{\tilde{n}-1}{\tilde{n}+1}\right|^2 = \frac{(n-1)^2+\kappa^2}{(n+1)^2+\kappa^2}. \tag{2.46}$$

The change of reflectance comes from several different sources. It can be due to the change of carrier density N, the scattering time τ, the restoring force ω_0, etc. The differential reflection can be expressed in terms of the change of the real and imaginary part of the dielectric constant respectively,

$$\begin{aligned}
\frac{\Delta R}{R} &= \frac{1}{R}\left(\frac{\partial R}{\partial \epsilon_1}\right)_{\epsilon_2}\delta\epsilon_1 + \frac{1}{R}\left(\frac{\partial R}{\partial \epsilon_2}\right)_{\epsilon_1}\delta\epsilon_2, && (2.47)\\
&\equiv \beta_1\,\delta\epsilon_1 + \beta_2\,\delta\epsilon_2, && (2.48)\\
\delta\epsilon_1 &= \delta\epsilon_1^{\mathrm{D}} + \delta\epsilon_1^{\mathrm{O}}, \quad \delta\epsilon_2 = \delta\epsilon_2^{\mathrm{D}} + \delta\epsilon_2^{\mathrm{O}}, && (2.49)
\end{aligned}$$

where the superindex D and O indicate the contribution from the intraband Drude term and interband oscillator term respectively. β_1 and β_2 are called the Seraphin coefficients and are given by the following equation:

$$\begin{aligned}
\beta_1 &= \frac{\sqrt{2}\left[(\epsilon_1-1)(\sqrt{\epsilon_1^2+\epsilon_2^2}+\epsilon_1)-\epsilon_2^2\right]}{[(\epsilon_1-1)^2+\epsilon_2^2]\sqrt{\epsilon_1^2+\epsilon_2^2}\sqrt{\sqrt{\epsilon_1^2+\epsilon_2^2}+\epsilon_1}}, && (2.50)\\
\beta_2 &= \frac{\sqrt{2}\epsilon_2(\sqrt{\epsilon_1^2+\epsilon_2^2}+2\epsilon_1-1)}{[(\epsilon_1-1)^2+\epsilon_2^2]\sqrt{\epsilon_1^2+\epsilon_2^2}\sqrt{\sqrt{\epsilon_1^2+\epsilon_2^2}+\epsilon_1}}. && (2.51)
\end{aligned}$$

From the Drude formula in Eqs. (2.37) and (2.37) we can obtain the change of the dielectric function,

$$\begin{aligned}
\delta\epsilon_1^{\mathrm{D}} &= N_0\frac{\partial\epsilon_1^{\mathrm{D}}}{\partial N_0}\frac{\delta N_0}{N_0} + \tau\frac{\partial\epsilon_1^{\mathrm{D}}}{\partial\tau}\frac{\delta\tau}{\tau}, && (2.52)\\
&\equiv D_{N_1}\frac{\delta N_0}{N_0} + D_{\tau_1}\frac{\delta\tau}{\tau}, && (2.53)\\
\delta\epsilon_2^{\mathrm{D}} &= N_0\frac{\partial\epsilon_2^{\mathrm{D}}}{\partial N_0}\frac{\delta N_0}{N_0} + \tau\frac{\partial\epsilon_2^{\mathrm{D}}}{\partial\tau}\frac{\delta\tau}{\tau}, && (2.54)\\
&\equiv D_{N_2}\frac{\delta N_0}{N_0} + D_{\tau_2}\frac{\delta\tau}{\tau}. && (2.55)
\end{aligned}$$

The coefficients are shown below:

$$D_{N_1} = -\frac{4\pi N_0 e^2}{m}\frac{\tau^2}{1+\omega^2\tau^2} = \epsilon_1^{\mathrm{D}} - 1, \tag{2.56}$$

$$D_{N_2} = \frac{4\pi N_0 e^2}{m}\frac{\tau}{\omega(1+\omega^2\tau^2)} = \epsilon_2^{\mathrm{D}}, \tag{2.57}$$

$$D_{\tau_1} = -\frac{8\pi N_0 e^2}{m}\frac{\tau^2}{(1+\omega^2\tau^2)^2} = \frac{2(\epsilon_1^{\mathrm{D}}-1)}{1+\omega^2\tau^2}, \tag{2.58}$$

$$D_{\tau_2} = \frac{4\pi N_0 e^2}{m}\frac{\tau(1-\omega^2\tau^2)}{\omega(1+\omega^2\tau^2)^2} = \frac{1-\omega^2\tau^2}{1+\omega^2\tau^2}\epsilon_2^{\mathrm{D}}. \tag{2.59}$$

For most semiconductors $\omega\tau \gg 1$ thus we have,

$$D_{\tau_1} \approx 0, \tag{2.60}$$

$$D_{\tau_2} \approx -\epsilon_2^{\mathrm{D}}, \tag{2.61}$$

$$\frac{|\epsilon_1^{\mathrm{D}} - 1|}{|\epsilon_2^{\mathrm{D}}|} = \omega\tau \gg 1. \tag{2.62}$$

For weak absorbing material the imaginary part of the dielectric function is small $\epsilon_2^{\mathrm{D}} \to 0$. The Seraphin coefficient can be simplified as

$$\beta_1 \to \frac{2}{(\epsilon_1 - 1)\sqrt{\epsilon_1}} + O(\epsilon_2^2), \tag{2.63}$$

$$\beta_2 \to \frac{3\epsilon_1 - 1}{(\epsilon_1 - 1)^2\epsilon_1^{3/2}}\epsilon_2 + O(\epsilon_2^3), \tag{2.64}$$

$$\beta_1/\beta_2 \to \omega\tau\frac{2\epsilon_1}{1-3\epsilon_1} \gg 1. \tag{2.65}$$

Therefore in the Drude model the differential reflectivity is dominated by the real part of the Seraphin coefficient and is more sensitive to the change of the carrier density.

Now let us turn to the transmission. Right at the interface the transmission coefficient is

$$T_0 = 1 - R = \frac{4n}{(n+1)^2 + \kappa^2}. \tag{2.66}$$

Inside the media the transmittance decreases as described by Beer's law in Eq. (2.2). For a film of thickness L the differential transmission as defined below is

$$\frac{\Delta T}{T} \equiv \left.\frac{T(z,\alpha)-T(z,\alpha_0)}{T(z,\alpha_0)}\right|_{z=L} \tag{2.67}$$

$$= -\delta\alpha \cdot L, \tag{2.68}$$

where α_0 and α are the absorption coefficient before and after the excitation respectively and $|\delta\alpha \cdot L| \ll 1$ is required. From the relationship between the absorption coefficient and the extinction coefficient in Eq. (2.8) we can obtain the change of the absorption coefficient,

$$\delta\alpha = \frac{2\omega}{c}\delta\kappa. \tag{2.69}$$

The change of extinction coefficient can be described similarly as the differential reflectivity,

$$\delta\kappa = \mu\delta\epsilon_1 + \nu\delta\epsilon_2, \tag{2.70}$$

with

$$\mu \equiv \left(\frac{\partial\kappa}{\partial\epsilon_1}\right)_{\epsilon_2} \tag{2.71}$$

$$= \frac{1}{2}\frac{\epsilon_1 - \sqrt{\epsilon_1^2+\epsilon_2^2}}{\sqrt{\epsilon_1^2+\epsilon_2^2}\sqrt{2(\sqrt{\epsilon_1^2+\epsilon_2^2}-\epsilon_1)}} \to -\frac{\epsilon_2}{4\epsilon_1^{3/2}} + O(\epsilon_2^3), \tag{2.72}$$

$$\nu \equiv \left(\frac{\partial\kappa}{\partial\epsilon_2}\right)_{\epsilon_1} \tag{2.73}$$

$$= \frac{1}{2}\frac{\epsilon_2}{\sqrt{\epsilon_1^2+\epsilon_2^2}\sqrt{2(\sqrt{\epsilon_1^2+\epsilon_2^2}-\epsilon_1)}} \to \frac{1}{2\sqrt{\epsilon_1}} + O(\epsilon_2^2), \tag{2.74}$$

and

$$\mu/\nu = \frac{\epsilon_1 - \sqrt{\epsilon_1^2+\epsilon_2^2}}{\epsilon_2} \to -\frac{1}{2}\frac{\epsilon_2}{\epsilon_1} \ll 1. \tag{2.75}$$

The change of the absorption coefficient in terms of the change of carrier density and scattering time is given by the following,

$$\delta\alpha = D_N \frac{\delta N}{N} + D_\tau \frac{\delta\tau}{\tau}, \tag{2.76}$$

with

$$D_N \approx \frac{\epsilon_1 + 1}{4\epsilon_1^{3/2}}\epsilon_2 + O(\epsilon_2^3), \tag{2.77}$$

$$D_\tau \approx -\frac{1}{2\sqrt{\epsilon_1}} + O(\epsilon_2^3). \tag{2.78}$$

Therefore the differential transmission is dominated by the change of the imaginary part of the dielectric function and the change of carrier density and scattering time have the same order of effect.

Following the same procedure we can discuss the differential reflectivity and differential transmission in the oscillator model. Some results are shown in Fig. 2–1 and Fig. 2–2.

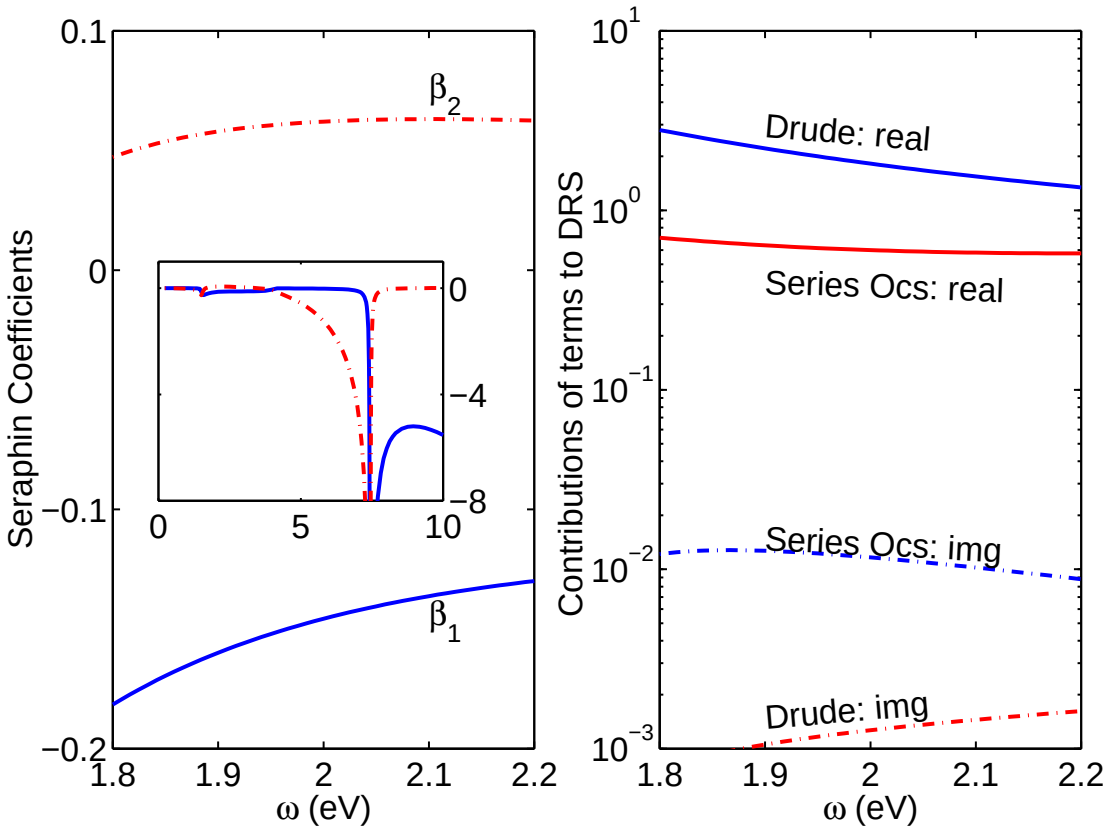

Figure 2–1: Spectral dependence of Seraphin coefficients and differential reflectivity.

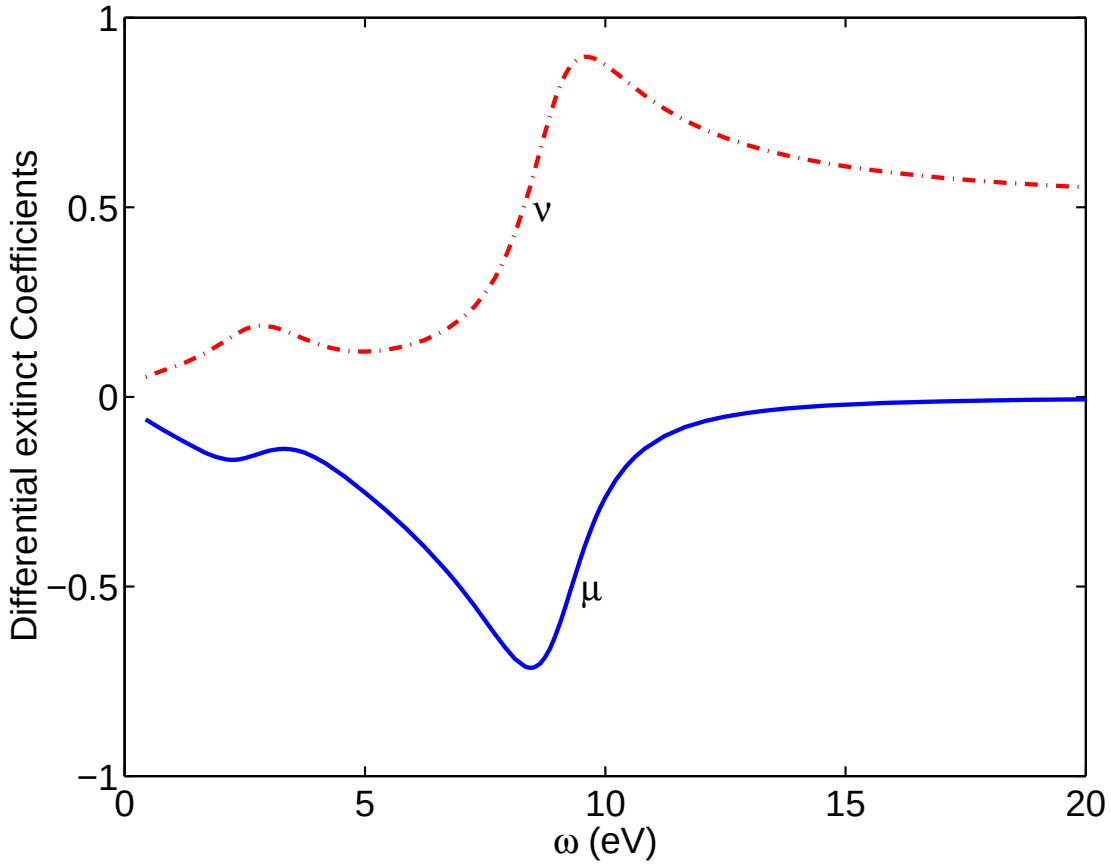

Figure 2–2: Spectral dependence of the coefficient of real and imaginary part of the dielectric function for differential transmission.

CHAPTER 3
GENERAL THEORY OF COHERENT PHONON

3.1 Phenomenological Model

The coherent phonon motion can be described in a phenomenological model of a driven harmonic oscillator [3]. The evolution of a coherent phonon amplitude Q in the presence of a driving force exerted by ultrafast laser pulse is governed by the differential equation

$$\frac{\partial^2 Q}{\partial t^2} + 2\gamma \frac{\partial Q}{\partial t} + \omega_0^2 Q = \frac{F(t)}{m}, \tag{3.1}$$

where ω_0 is the frequency of the phonon mode, γ is the damping parameter, m is the mass of the oscillator, and F is the driving force, which may depend on carrier density, temperature, and other parameters of the system. The damping parameter γ is the inverse of the dephasing time T_2 of the coherent phonon mode [16]. The dephasing time T_2 comes from a combination of phase-destroying processes with relaxation time T_p and population decreasing processes with relaxation time T_1. Examples of the latter are anharmonic decay processes such as the decay of LO phonons into acousitc phonons and electron-phonon interaction processes where a phonon can be absorbed by an electron. Ultrafast generation of carriers by femtosecond lasers causes the driving force to rapidly turn on and trigger the oscillations.

Oscillator Eq. (3.1) can be solved formally by using either Green's functions or Laplace transforms with the initial condition that both Q and $\partial Q/\partial t$ are zero before the force F is applied with the result [17],

$$Q(t) = \int_{-\infty}^{t} \frac{F(\tau)}{m} \frac{e^{-\gamma(t-\tau)} \sin\left(\sqrt{\omega_0^2 - \gamma^2}(t-\tau)\right)}{\sqrt{\omega_0^2 - \gamma^2}} \, \mathrm{d}\tau. \tag{3.2}$$

We consider two kinds of forcing functions [17]. The first kind is impulsive forces, which have the form

$$F_i(t) = I\,\delta(t), \tag{3.3}$$

where $\delta(t)$ is a Dirac delta function in time.

After integrating Eq. (3.2) directly we have

$$Q(t) = \frac{I}{m\sqrt{\omega_0^2 - \gamma^2}}\, e^{-\gamma t} \sin\left(\sqrt{\omega_0^2 - \gamma^2}t\right)\theta(t). \tag{3.4}$$

The solution shows that an impulsive force starts oscillations about the current equilibrium position, which will damp out exponentially .

The other kind of forcing function is displacive with a form given by

$$F_d(t) = D\,\theta(t), \tag{3.5}$$

where $\theta(t)$ is a Heaveside step function.

Again we can integrate Eq. (3.2) directly to get the coherent phonon amplitude

$$Q(t) = \frac{D}{m\omega_0^2}\,\theta(t)\left\{1 - e^{-\gamma t}\left[\cos\left(\sqrt{\omega_0^2 - \gamma^2}t\right) + \frac{\gamma}{\sqrt{\omega_0^2 - \gamma^2}}\sin\left(\sqrt{\omega_0^2 - \gamma^2}t\right)\right]\right\}. \tag{3.6}$$

The solution in the case of a displacive forcing function shows oscillations and exponential damping too, but compared to the impulsive case, a displacive force will move the oscillator to a new equilibrium position with a different initial phase.

3.2 Microscopic Theory

The phenomenological oscillator model captures the essential physics. However it leaves open the question of exact definition of coherent phonon amplitude. The microscopic quantum mechanical justification of the oscillator model is given by Kuznetsov and Stanton [18].

In a simplified system consisting of two electronic bands interacting with phonon modes, the Hamiltonian consists three parts: free Bloch electrons and

holes in a perfect static crystal lattice, the free phonons, and the electron-phonon interaction.

$$H = \sum_{\alpha,\mathbf{k}} \epsilon_{\alpha\mathbf{k}} c^\dagger_{\alpha\mathbf{k}} c_{\alpha\mathbf{k}} + \sum_{\mathbf{q}} \hbar\omega_{\mathbf{q}} b^\dagger_{\mathbf{q}} b_{\mathbf{q}} + \sum_{\alpha,\mathbf{k},\mathbf{q}} M^\alpha_{\mathbf{kq}} \left(b_{\mathbf{q}} + b^\dagger_{-\mathbf{q}} \right) c^\dagger_{\alpha\mathbf{k}} c_{\alpha\mathbf{k}+\mathbf{q}} \tag{3.7}$$

The Lattice displacement operator $\hat{u}(\mathbf{r})$ is expressed in terms of the phonon creation and annihilation operators:

$$\hat{u}(\mathbf{r}) = \sum_{\mathbf{q}} \sqrt{\frac{\hbar}{2\rho V \omega_{\mathbf{q}}}} \{ b_{\mathbf{q}} e^{i\mathbf{q}\cdot\mathbf{r}} + b^\dagger_{\mathbf{q}} e^{-i\mathbf{q}\cdot\mathbf{r}} \}. \tag{3.8}$$

The coherent phonon amplitude of the $\mathbf{q}$th mode is defined as:

$$D_{\mathbf{q}} \equiv \langle b_{\mathbf{q}} \rangle + \langle b^\dagger_{-\mathbf{q}} \rangle \equiv B_{\mathbf{q}} + B^*_{-\mathbf{q}}. \tag{3.9}$$

Therefore the coherent amplitude is proportional to the Fourier components of the displacement in Eq. (3.8)

The average of the coherent amplitude will vanish in a phonon oscillator eigenstate. The average displacement of the lattice vanishes, but there are fluctuations: $\langle u^2 \rangle \propto \langle bb^\dagger + b^\dagger b \rangle$. These phonons are incoherent phonons in the mode. A nonzero displacement requires that the wave function of the oscillator be in a coherent superposition of more than one phonon eigenstate. In a general state there can be a number of both coherent and incoherent phonons.

The canonical coherent states are defined for each complex number z in terms of eigenstate of harmonic oscillator.

$$\Psi^{coh} = |z\rangle \equiv e^{(zb^\dagger - z^* b)} |0\rangle = \sum_n \frac{z^n}{\sqrt{n!}} e^{-z^2} |n\rangle \tag{3.10}$$

They have two important properties. Firstly, they are eigenvector of the annihilation operator with eigenvalue z, therefore in a canonical coherent state, the

coherent amplitude defined in Eq. (3.9) is

$$B_{\mathbf{q}}^{coh} \equiv \langle z|b_{\mathbf{q}}|z\rangle = z. \tag{3.11}$$

Secondly, canonical coherent states are minimum-uncertainty wave-packets. When the amplitude z is large, they behave like a macroscopic harmonic oscillator. So they are called "quasi-classical" states.

Using the operator form of the Schrödinger equation

$$i\hbar\frac{\partial}{\partial t}\langle\hat{A}\rangle = \langle[\hat{A},\hat{H}]\rangle + i\hbar\langle\frac{\partial\hat{A}}{\partial t}\rangle, \tag{3.12}$$

we can obtain the dynamic equation of motion for the coherent phonon amplitude

$$\frac{\partial^2 D_{\mathbf{q}}}{\partial t^2} + \omega_{\mathbf{q}}^2 D_{\mathbf{q}} = \frac{-2\omega_{\mathbf{q}}}{\hbar}\sum_{\alpha,\mathbf{k}} M_{\mathbf{k}-\mathbf{q}}^{\alpha} n_{\mathbf{k},\mathbf{k}-\mathbf{q}}^{\alpha}. \tag{3.13}$$

Here $n_{\mathbf{k},\mathbf{k}-\mathbf{q}}^{\alpha} \equiv \langle c_{\alpha\mathbf{k}}^{\dagger} c_{\alpha\mathbf{k}-\mathbf{q}}\rangle$ is the electronic density matrix. The electronic density matrix $n_{\mathbf{k},\mathbf{k}-\mathbf{q}}^{\alpha}$ in the right hand side of Eq. (3.13) is nonzero only after excitation with an ultrafast laser pulse.

This equation is written in momentum space. Because of the Fourier transform relation between the coherent amplitude and the lattice displacement, we have obtained the phenomenological Eq. (3.1). However there is no dampening term because we neglected anharmonic terms in the lattice potential.

In bulk materials since the laser wavelength is much larger than the lattice constant, the created carriers are in a macroscopically uniform state, so that the electronic density matrix is diagonal. So the only phonon mode that is coherently driven by the optical excitation is the $q \approx 0$ mode.

In superlattice and multiple quantum well systems, the carriers are created in the wells only. Because of the periodicity of the superlattice structure, the electronic density matrix has a $q \neq 0$ element which can excite the coherent acoustic phonon mode.

3.3 Interpretation Of Experimental Data

In the pump-probe experiment the measured quantities are usually the differential reflectivity or differential transmission. This section discusses the relation between the lattice displacement and the measured physical quantity.

Assume the only motion is parallel to the z axis and the only nonzero component of the elastic strain is η_{33}. The strain is related to the lattice displacement $U(z,t)$ in the z direction through the following equation,

$$\eta_{33} = \frac{\partial U(z,t)}{\partial z}. \tag{3.14}$$

The change of reflection or transmission is due to strain induced variation of the optical constants of the material under consideration. In the linear approximation we have

$$\Delta n(z,t) = \frac{\partial n}{\partial \eta_{33}}\eta_{33}, \tag{3.15}$$

$$\Delta \kappa(z,t) = \frac{\partial \kappa}{\partial \eta_{33}}\eta_{33}, \tag{3.16}$$

where Δn and $\Delta \kappa$ are the changes in the real and imaginary part of the complex index of refraction.

For normally incident light the Maxwell's equation for electric field gives

$$\frac{\partial^2 \mathcal{E}(z,t)}{\partial z^2} - \frac{1}{c^2}[\epsilon + \Delta\epsilon(z,t)]\frac{\partial^2 \mathcal{E}(z,t)}{\partial t^2} = 0, \tag{3.17}$$

where the change of the dielectric constant is related to the change of the index of refraction through

$$\epsilon(z,t) = (n+\kappa)^2, \tag{3.18}$$

$$\begin{aligned} \Delta\epsilon(z,t) &= 2(n+\kappa)\Delta(n+i\kappa), \\ &= 2\sqrt{\epsilon}\Delta(n+i\kappa). \end{aligned} \tag{3.19}$$

We write the probe electric field as

$$\mathcal{E} = F(z,t)e^{i\omega t}, \tag{3.20}$$

where $F(z,t)$ is a slowly varying envelope function.

Substituting Eq. (3.20) into Eq. (3.17) we obtain the following equation for the envelope function $F(z,t)$,

$$\frac{\partial^2 F(z,t)}{\partial z^2} + \frac{\omega^2}{c^2}\left[\epsilon + \Delta\epsilon(z,t)\right]\left\{F - \frac{2i}{\omega}\frac{\partial F}{\partial t} - \frac{1}{\omega^2}\frac{\partial^2 F}{\partial t^2}\right\} = 0. \tag{3.21}$$

Since we assumed that F is slowly varying we can neglect the derivative of F with respect to time and rewrite the above equation as

$$\frac{\partial^2 F(z,t)}{\partial z^2} + \frac{\omega^2}{c^2}\left[\epsilon + \Delta\epsilon(z,t)\right]F = 0, \tag{3.22}$$

which is analogous to Eq. (3.26) in Thomsen's paper [19] where he calculated the change of reflection. The result is

$$\Delta R(t) = \int_0^\infty f(z)\eta_{33}\,\mathrm{d}z, \tag{3.23}$$

where $f(z)$ is the "sensitivity function", which determines how strain at different depths below the interface contributes to the change in the reflectivity and is given by

$$f(z) = f_0\left[\frac{\partial n}{\partial \eta_{33}}\sin\left(\frac{4\pi n z}{\lambda} - \phi\right) + \frac{\partial \kappa}{\partial \eta_{33}}\cos\left(\frac{4\pi n z}{\lambda} - \phi\right)\right]e^{-z/\zeta}, \tag{3.24}$$

$$f_0 = 8\frac{\omega\sqrt{n^2(n^2+\kappa^2-1)^2 + \kappa^2(n^2+\kappa^2+11)^2}}{c[(n+1)^2+\kappa^2]^2}, \tag{3.25}$$

$$\phi = \arctan\frac{\kappa(n^2+\kappa^2+1)}{n(n^2+\kappa^2-1)}, \tag{3.26}$$

and λ is the laser wavelength, ζ is the absorption length defined as the reciprocal of the absorption coefficient.

In the following we will carry out the calculation for the differential transmission. If we set the probe electric field of a normal incident laser at $z = 0$ as a Gaussian function

$$\mathcal{E}(z=0,t) = \mathcal{E}_0 e^{-\gamma(t-\tau)^2} e^{i\omega t}, \tag{3.27}$$

where τ is the probe delay with respect to the pump, then in the absence of strain we have the wave equation solution of the field as

$$\begin{aligned} \mathcal{E}_0(z,t) &= \mathcal{E}(z=0, t-\frac{z}{v}), \quad \text{where } v = \frac{c}{n}, & (3.28)\\ &= \mathcal{E}_0 e^{-\gamma(t-z/v-\tau)^2} e^{i\omega(t-z/v)}. & (3.29) \end{aligned}$$

Comparing the above equation with Eq. (3.20) we can obtain the envelope function for the field without the strain

$$F_0(z,t) = \mathcal{E}_0 e^{-\gamma(t-\tau-z/v)^2} e^{-i\omega z/v}. \tag{3.30}$$

With strain present the probe electric field will change to

$$\begin{aligned} \mathcal{E}(z,t) &= \mathcal{E}_0(z,t) + \mathcal{E}_1(z,t), & (3.31)\\ &= [F_0(z,t) + F_1(z,t)] e^{i\omega t}, & (3.32) \end{aligned}$$

where $F_1(z,t)$ is the correction due to the change of optical constants caused by the strain that resulted from the pump field.

Substituting Eq. (3.32) into the partial differential Eq. (3.22) for the envelope function we find the equation for the correction to the envelope function

$$\frac{\partial^2 F_1(z,t)}{\partial z^2} + \frac{\omega^2}{v^2} F_1(z,t) = -\frac{\omega^2}{v^2} \frac{\Delta\epsilon(z,t)}{\epsilon} F_0(z,t). \tag{3.33}$$

For the forward propagating wave at the boundary conditions are

$$\begin{aligned} F_1(z, t=-\infty) &= 0, & (3.34)\\ F_1(z=-\infty, t) &= 0. & (3.35) \end{aligned}$$

The Green's function for $F_1(z,t)$ satisfies

$$\frac{\partial^2 G(z)}{\partial z^2} + \frac{\omega^2}{v^2} G(z) = \delta(t). \tag{3.36}$$

The solution with the boundary condition (3.35) taken into consideration is

$$G(z) = 0 \quad (z < 0), \tag{3.37}$$

$$G(z) = C \sin(\omega z/v) + D \cos^{\omega z/v} \quad (z > 0). \tag{3.38}$$

From the continuity condition at $z = 0$ we have $D = 0$. Integrating Eq. (3.36) about $z = 0$ we have

$$\frac{\partial G(0^+)}{\partial z} - \frac{\partial G(-0^-)}{\partial z} = 1, \tag{3.39}$$

which gives $C = v/\omega$. Therefore the Green's function is

$$G(z-\zeta) = \frac{v}{\omega} \sin\left(\frac{\omega}{v}(z-\zeta)\right). \tag{3.40}$$

Using the above Green's function we can obtain the correction to the envelope function

$$F_1(z,t) = \int_{-\infty}^{\infty} G(z-\zeta) \left\{ -\frac{\omega^2}{v^2} \frac{\Delta\epsilon(\zeta,t)}{\epsilon} F_0(\zeta,t) \right\} \mathrm{d}\zeta, \tag{3.41}$$

$$= -\mathcal{E}_0 \frac{\omega}{v} \int_{-\infty}^{z} \mathrm{d}\zeta \, \sin\left[\frac{\omega}{v}(z-\zeta)\right] \frac{\Delta\epsilon(\zeta,t)}{\epsilon} e^{-i\omega\zeta/v} e^{-\gamma(t-\tau-\zeta/v)^2}. \tag{3.42}$$

Before the pump laser is turned on the transmission intensity is

$$T_0(z,\omega) = |\mathcal{E}_0^0(z,\omega)|^2. \tag{3.43}$$

After the pump laser excitation the transmission intensity becomes

$$T_{\mathrm{P}}(z,\omega) = |\mathcal{E}_0^{\mathrm{P}}(z,\omega) + \mathcal{E}_1(z,\omega)|^2, \tag{3.44}$$

where $\mathcal{E}_0^{\rm P}(z,\omega)$ is the probe electric field in the absence of strain but with the pump on.

By definition, the differential transmission is given by

$$\begin{aligned}
\frac{\Delta T}{T}(z,\omega) &= \frac{T_{\rm P}(z,\omega)-T_0(z,\omega)}{T_0(z,\omega)}, && (3.45)\\
&= \frac{|\mathcal{E}_0^{\rm P}(z,\omega)+\mathcal{E}_1(z,\omega)|^2-|\mathcal{E}_0^0(z,\omega)|^2}{|\mathcal{E}_0^0(z,\omega)|^2}, && (3.46)\\
&\approx \frac{|\mathcal{E}_0^{\rm P}(z,\omega)|^2-|\mathcal{E}_0^0(z,\omega)|^2}{|\mathcal{E}_0^0(z,\omega)|^2}+\frac{2{\rm Re}\left(\mathcal{E}_0^{\rm P}(z,\omega)^*\mathcal{E}_1(z,\omega)\right)}{|\mathcal{E}_0^0(z,\omega)|^2}, && (3.47)\\
&= \left(\frac{\Delta T}{T}\right)_0+\left(\frac{\Delta T}{T}\right)_1, && (3.48)
\end{aligned}$$

where in the last line we neglected the second order term of $\mathcal{E}_1$. The first term is that part of the differential transmission without the strain which can be calculated using Fermi's golden rule

$$\left(\frac{\Delta T}{T}\right)_0=\frac{4\pi^2e^2\omega}{n_rc}\sum_{nn'}\frac{1}{A}\sum_{\mathbf{k}}\left(1+f_n^c(\mathbf{k},\tau)-f_{n'}^v(\mathbf{k},\tau)\right)|\hat{\epsilon}\cdot\mathbf{d}_{nn'}^{cv}(\mathbf{k})|^2\delta\left(E_n^c(k)-E_{n'}^v(k)-\hbar\omega\right). \quad (3.49)$$

The contribution of strain to the differential transmission is

$$\begin{aligned}
\left(\frac{\Delta T}{T}\right)_1 &= \frac{2{\rm Re}\left(\mathcal{E}_0^{\rm P}(z,\omega)^*\mathcal{E}_1(z,\omega)\right)}{|\mathcal{E}_0^0(z,\omega)|^2}, && (3.50)\\
&= {\rm Re}\left\{-\frac{4\omega\sqrt{\gamma}}{v\sqrt{\pi\epsilon}}\left(\frac{\partial n}{\partial\eta_{33}}+i\frac{\partial\kappa}{\partial\eta_{33}}\right)\int_{-\infty}^{z}{\rm d}\zeta\sin\left(\frac{\omega}{v}(z-\zeta)\right)e^{-i\omega(z-\zeta)/v}\right.\\
&\qquad \left.\int_{-\infty}^{\infty}{\rm d}te^{-\gamma(t-\tau-\zeta/v)^2}\frac{\partial u}{\partial z}(\zeta,t)\right\}, && (3.51)
\end{aligned}$$

where the first term of the differential transmission gives the background and the coherent phonon oscillation comes from the strain induced second term.

3.4 Three Kinds Of Coherent Phonons

In the experiment three kinds of different coherent phonons have been observed. They are the optical coherent phonons in bulk semiconductors, the acoustic coherent phonons in superlattices or MQWs, and the propagating coherent phonon wavepackets in epilayer systems.

The coherent optical phonons have been observed in many different materials. In layered or low-symmetry materials such as Sb, Bi, Te, and Ti_2O_3 [20, 3] the A1 phonon modes can be excited by the deformational phonon coupling mechanism. In cubic materials such as Ge [21], the driving force vanishes for deformational potential coupling. What causes the driving force not to vanish is the finite absorption depth of the ultrafast laser pulse and band structure effects. But the oscillations are weaker than that of the other systems. In polar materials like GaAs [22] the coupling between electrons and phonons can be both deformational and polar with the latter stronger and being the dominant effect.

As an example Cho et. al. measured the differential reflection of (100)-oriented bulk GaAs for three different angles θ between the probe beam polarization and the [010] crystal axis. The orthogonally polarized beams are kept close to normal incidence. In the case of $\theta = 90°$ the reflectivity rises during and peaks towards the end of the excitation pulse. After passing through a minimum at a time delay of 200 fs the reflectivity rises again to a quasistationary value on a picosecond time scale, without any periodic oscillations. The temporal evolution of the reflection transient is entirely due to susceptibility changes induced by the optically excited electronic carriers, their thermalization, and relaxation down to the band edges as well as intervalley transfer. Rotating the sample to $\theta = 45°$ results in a shift of the entire reflectivity signature to higher values. The signal response for positive time delays shows a periodic modulation with an oscillation frequency of 8.8 ± 0.15 THz, exactly matching the frequency of the Γ_{15} LO phonon in GaAs. In the case of $\theta = 135°$ a complementary shift to lower reflectivity changes together with an additional phase shift of π in the phonon-induced oscillations is observed. The distinct dependence of reflection modulation on probe beam polarization shows the electro-optic nature of this effect, which is well known for cubic zinc-blende group materials with $\bar{4}$3m crystal symmetry.

In a bulk semiconductor the laser wavelength is much larger than the lattice spacing, so the photo-generated carriers are typically excited by the optical pump over spatial areas that are much larger than the lattice unit cell, which means the excited carrier populations are generated in a macroscopic state and the carrier density matrix has only a $q \approx 0$ Fourier component. As a result only the $q \approx 0$ phonon mode is coupled to the photoexcited carriers. Since the frequency of the $q \approx 0$ acoustic phonon is zero, only the coherent optic phonons are excited in bulk semiconductors.

Now the case is different for semiconductor multiple quantum wells and superlattices. The pump can preferentially generate electron-hole pairs only in the wells even though the laser pump has a wavelength large compared to the lattice spacing. So the photoexcited carrier distributions have the periodicity of the superlattice. Since the density matrix of the photo-excited carrier populations now have a $q \neq 0$ Fourier component, the photo-excited carriers can not only couple to the optical phonon modes, but they can also generate coherent acoustic phonon modes with a nonzero frequency and wavevector $q \approx 2\pi/L$ where L is the superlattice period.

In the next chapter I will discuss the coherent acoustic phonons in multiple quantum wells. The experimental data and theory of propagating coherent phonon in GaN/InGaN epilayer system will be presented in chapter 5.

CHAPTER 4
THE COHERENT ACOUSTIC PHONON

The second type of coherent phonon is the acoustic one. The earlier experimental observations of zone-folded acoustic phonons are made by Colvard et al. [23] They used a photoelastic continuum model to predict the scattering intensities of the folded acoustic modes.

The acoustic branch of semiconductor superlattices folds within the mini-Brillouin zone because of the artificial periodicity of the superlattices. This leads to the observation of coherent oscillation of the zone folded acoustic phonons in AlAs/GaAs superlattices [24, 25]. The observed differential reflection oscillation was very small, however, on the order of $\Delta R/R \sim 10^{-5} - 10^{-6}$. The detection mechanism was based on interband transitions due to the acoustic deformation potential [25].

In the year 2000 Sun et al. reported huge coherent acoustic phonon oscillations in wurtzite (0001) InGaN/GaN multi-quantum well samples with strain induced piezoelectric fields [26]. The oscillations were very strong with differential transmission $\Delta T/T \sim 10^{-2} - 10^{-3}$ compared to the usual differential reflection on the order of 10^{-5}–10^{-6}. The oscillation frequency, in the THz range, corresponded to the LA phonon frequency with $q \approx 2\pi/l$, where l is the period of MQWs.

The experiments of Sun et al. were done at room temperature on samples of 14 period InGaN/GaN MQWs with barrier widths fixed at 43 Å, well widths varying from 12 to 62 Å, and In composition varying between 6–10%. The oscillation period for 50 Å MQW was 1.38 ps, which corresponds to a frequency of 0.72 THz. By changing the period widths of MQWs, Sun et al. obtained a linear relation between the observed oscillation frequency ω and the wavevector $q = 2\pi/l$ of

photogenerated carriers. The slope of this dispersion, 6820 m/s, agrees well with the sound velocity of GaN.

In this chapter, I will discuss briefly a microscopic theory [27] for coherent acoustic phonons in strained wurtzite InGaN/GaN MQWs. This microscopic theory can be simplified and mapped onto a *loaded string model* instead of a forced oscillator model [1] as in the case for coherent optical phonons in bulk systems. Based on the string model the simulation will show the strain, energy density, and other physical quantities. I will also discuss the coherent control of the acoustic coherent phonon.

4.1 Microscopic Theory

The microscopic theory for coherent acoustic phonons in multiple quantum well system has many details and is very convoluted, so I will just give an outline of the theory. The basic approach is the same as that used for coherent optic phonons in bulk semiconductors, i.e. to obtain the total Hamiltonian of the system and then to derive the equations of motion for the coherent phonon amplitudes, which are coupled to the equations of motion for the electron density matrices.

First of all one wants to obtain the energy dispersion relation and wavefunctions for carriers moving in a multiple quantum well system so that one can write down the electronic part of the Hamiltonian for the independent and free carriers.

The GaN/InGaN multiple quantum wells is shown schematically in Fig. 4–1. The intrinsic active region consists of a left GaN buffer region, several pseudomorphically strained (0001) $In_xGa_{1-x}N$ quantum wells sandwiched between GaN barriers, and a right GaN buffer region. The total length of the MQWs between the P and N regions is L, across which a voltage drop, ΔV, is maintained. Photoexcitation of carriers is done using an ultrafast laser pulse incident normally along the (0001) growth direction, taken to coincide with the z-axis.

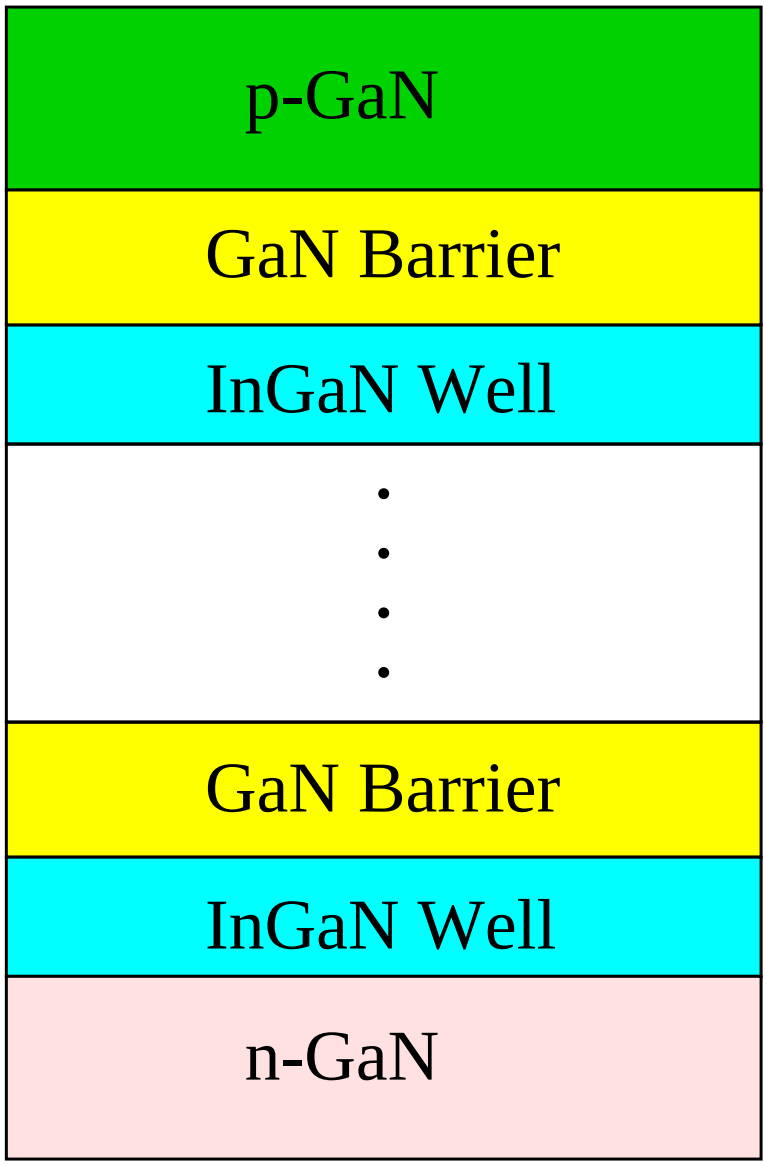

Figure 4–1: Schematic diagram of the $In_xGa_{1-x}N$ MQW diode structure.

The offsets and effects of the built-in piezoelectric field are shown in Fig. 4–2 from which we can see that the built-in piezoelectric field is responsible for the spatial separation of the photoexcited electrons and holes so that the density distribution of these two kinds of carriers differ from each other which results in a non-zero non-uniform driving force for the coherent phonon oscillations.

In bulk systems, the conduction and valence bands in wurtzite crystals including the effects of strain can be treated by effective mass theory. Near the band edge, the conduction band Hamiltonian is a 2×2 matrix because of the electron spin, while the Hamiltonian for the valence bands is a 6×6 matrix due to the heavy holes, light holes, and split-off holes. [28, 29]

In quantum confined systems shown in Fig. 4–1, the bulk Hamiltonian is modified. The finite MQW structure breaks translational symmetry along the z direction but not in the xy plane. The quantum confinement potentials comes from three sources: (i) bandgap discontinuities between well and barrier regions, (ii) the strain-induced piezoelectric field, and (iii) the time-dependent electric field due to photoexcited electrons and holes.

$$V_\alpha(z,t) = V_{\alpha,\text{gap}}(z) + V_{\text{piezo}}(z) + V_{\text{photo}}(z,t), \tag{4.1}$$

where $\alpha = \{c, v\}$ refers to conduction or valence subbands.

The confinement of carriers in the MQW leads to a set of two-dimensional subbands. In envelope function approximation, the wavefunction consists of factors of a slowly varying real envelope function in the superlattice direction and a rapidly varying Bloch wavefunction.

Solving Schrödinger equations, one obtains the eigenvalues as the subband energies, $E_n^\alpha(k)$, with n the subband index, and the corresponding eigenvectors as the envelope functions. With this energy dispersion, one can write down the second

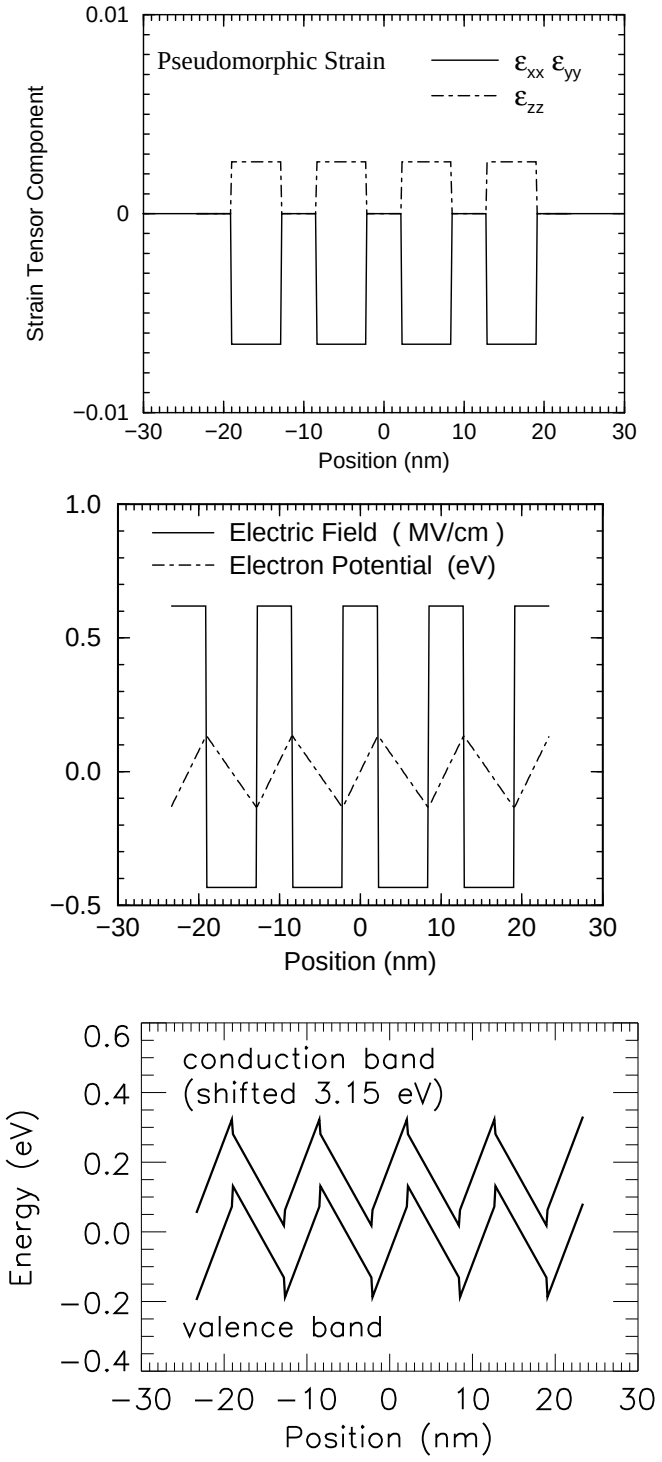

Figure 4–2: Effects of the built-in piezoelectric field to the bandgap of the MQWs. The upper figure shows strain tensor components for pseudomorphically strained InGaN MQW diode as a function of position. The middle figure shows the electric field and potential due to the the above built-in strain field. The lower figure shows the conduction and valence band edges. The applied dc bias has been adjusted so flat-band biasing is achieved, i. e., so that band edges are periodic functions of position. [See Sanders et al., PRB, 64:235316, 2001]

quantized Hamiltonian for free electrons and holes in the multiple quantum well,

$$\mathcal{H}_{e0} = \sum_{\alpha,n,\mathbf{k}} E_n^{\alpha}(k)\ c^{\dagger}_{\alpha,n,\mathbf{k}} c_{\alpha,n,\mathbf{k}}, \tag{4.2}$$

where $c^{\dagger}_{\alpha,n,\mathbf{k}}$ and $c_{\alpha,n,\mathbf{k}}$ are electron creation and destruction operators in conduction and valence subbands respectively.

The acoustic phonons in the multiple quantum well are taken as plane-wave states with wave vector $\mathbf{q}$. Due to the cylindrical symmetry of the system, one need consider only longitudinal acoustic phonons with $\mathbf{q} = q\ \hat{\mathbf{z}}$ because these are the ones coupled by the electron-phonon interaction. The free LA phonon Hamiltonian is given by

$$\mathcal{H}_{A0} = \sum_{q} \hbar\omega_q\ b^{\dagger}_q b_q. \tag{4.3}$$

where $b^{\dagger}_q$ and b_q are creation and destruction operators for LA phonons with wavevector $\mathbf{q} = q\ \hat{\mathbf{z}}$ and $\omega_q = c\ |q|$ is the linear dispersion of the acoustic phonons with c being the LA phonon sound speed.

Statistical operators are normally defined in terms of the electron and phonon eigenstates. So one can write down the electron density matrix as

$$N^{\alpha,\alpha'}_{n,n'}(\mathbf{k},t) \equiv \left\langle\ c^{\dagger}_{\alpha,n,\mathbf{k}}(t)\ c_{\alpha',n',\mathbf{k}}(t)\ \right\rangle \tag{4.4}$$

where $\langle\ \rangle$ denotes the statistical average of the non-equilibrium state of the system.

The diagonal component of the electron density matrix is the distribution function for electrons in the subband, while other components describe the coherence between carriers in different subbands, including both intraband and interband components.

The coherent phonon amplitude of the q-th phonon mode, $|q\rangle$, is defined the same as in the last chapter [1]

$$D_q(t) \equiv \left\langle\ b^{\dagger}_q(t) + b_{-q}(t)\ \right\rangle \tag{4.5}$$

Note again that the coherent phonon amplitude is related to the the macroscopic lattice displacement $U(z,t)$ through

$$U(z,t) = \sum_q \sqrt{\frac{\hbar^2}{2\rho_0\ (\hbar\omega_q)\ V}}\ e^{iqz}\ D_q(t) \tag{4.6}$$

To derive the equations of motion for the electron density matrix and the coherent phonon amplitude, one must know the total Hamiltonian of the system, which in this case is given by

$$\mathcal{H} = \mathcal{H}_{e0} + \mathcal{H}_{ee} + \mathcal{H}_{eL} + \mathcal{H}_{A0} + \mathcal{H}_{eA}. \tag{4.7}$$

The first term is just free electrons and holes as in Eq. (4.2). The second term describes the Coulomb interaction between carriers, including screening and neglecting the Coulomb-induced interband transitions because they are energetically unfavorable [30]. The third term describes the creation of electron-hole pairs by the pump laser, the electric field of which is treated in the semiclassical dipole approximation.

The last two terms are related to the acoustic phonons. One is the free longitudinal acoustic phonons given by Eq. (4.3) and the other is the electron-LA phonon interaction, which describes the scattering of an electron from one subband to another by absorption or emission of an LA phonon. $\mathcal{H}_{eA}$ has the same form as that of the bulk semiconductor. The interaction matrix includes both deformation and screened piezoelectric scattering.

In the end one obtains a closed set of coupled partial differential equations for the electron density matrices and coherent phonon amplitudes. The equation of motion for the coherent phonon amplitude $D_q(t)$, which is similar to the case of bulk semiconductor, is given by a driven harmonic oscillator equation ,

$$\frac{\partial^2 D_q(t)}{\partial t^2} + \omega_q^2 D_q(t) = f(N, \omega_q, q, t), \tag{4.8}$$

where N is the electron density matrix defined in Eq. (4.4), and the initial conditions are

$$D_q(t=-\infty) = \frac{\partial D_q(t=-\infty)}{\partial t} = 0. \tag{4.9}$$

4.2 Loaded String Model

The microscopic theory is very detailed. However we are more interested in the lattice displacement $U(z,t)$. It is both more insightful and much easier to deal with the lattice displacement directly. Given the linear acoustic phonon dispersion relation, we can do Fourier transformation on the equation of motion for the coherent phonon amplitude $D_q(t)$. The result is the following equation for the lattice displacement $U(z,t)$,

$$\frac{\partial^2 U(z,t)}{\partial t^2} - c^2 \frac{\partial^2 U(z,t)}{\partial z^2} = S(z,t), \tag{4.10}$$

subject to the initial conditions

$$U(z,t=-\infty) = \frac{\partial U(z,t=-\infty)}{\partial t} = 0. \tag{4.11}$$

The forcing function $S(z,t)$ packages all the microscopic details.

Since the absorption occurs only in the wells, the forcing function is not uniform. It normally has the same period as the superlattice. The sound speeds of GaN and InGaN are almost the same as discussed in the introduction chapter. The difference of sound speed for a typical In component of $x = 0.08$ is about 2%, which causes an even smaller reflection on the order of 10^{-4}, so this difference can be safely neglected. Thus, Eq. 5.17 describes a uniform string with a nonuniform forcing function. We call this one-dimensional wave equation of the lattice displacement the "string model".

Note the difference between a bulk system and a MQW or superlattice. In a bulk semiconductor, both the amplitude U and the Fourier transform of the amplitude $D_q(t)$ for an $q \approx 0$ optic mode satisfy a forced oscillator equation.

For the nonuniform, multiple quantum well case, one can excite acoustic modes with $q \neq 0$. The Fourier transform of the amplitude D_q obeys a forced oscillator equation, but owing to the linear dependence of $\omega(q)$ on q , the amplitude itself U obeys a 1-D wave equation with a forcing term $S(z,t)$.

Under ideal conditions the forcing function takes a simple form [27]

$$S(z,t) = \sum_{\nu} S_{\nu}(z,t), \tag{4.12}$$

where the index, ν, is for different kinds of carriers and the forcing function satisfies the sum rule

$$\int_{-\infty}^{\infty} \mathrm{d}z \; S(z,t) = 0, \tag{4.13}$$

which requires that the average force on the string be zero so that the center of mass of the string would have no accelerating motion.

The partial driving functions, $S_{\nu}(z,t)$, are given by [27]

$$S_{\nu}(z,t) = \pm \frac{1}{\rho_0} \left\{ a_{\nu} \frac{\partial}{\partial z} + 4\pi \frac{|e| \; e_{33}}{\epsilon_{\infty}} \right\} \rho_{\nu}(z,t) \tag{4.14}$$

where the plus sign is for conduction electrons and the minus sign for holes. The photogenerated electron or hole number density is $\rho_{\nu}(z,t)$ and ρ_0 is the mass density. The partial forcing function has two terms, the first due to deformation potential scattering and the second to piezoelectric scattering. The piezoelectric coupling constant, e_{33}, is the same for all carrier species, while the deformation potential, a_{ν}, depends on the species.

Another interesting point is that Planck's constant cancels out in the string model. It does not appear in either the string equation (5.17), or in its related forcing function defined in Eqs. (4.12) and (4.14). So essentially, coherent LA phonon oscillations in an MQW is also an classical phenomenon, like the coherent LO phonon oscillations in bulk semiconductors [1].

4.3 Solution of The String Model

Using Green's function method, we can solve the wave equation (5.17) for a given forcing function with the initial conditions in Eq. (4.11). The general solution is given by

$$U(z,t) = \int_{-\infty}^{\infty} \mathrm{d}\tau \int_{-\infty}^{\infty} \mathrm{d}\zeta \; G(z-\zeta, t-\tau) \; S(\zeta,\tau). \tag{4.15}$$

In performing the above integration of the forcing function $S(z,t)$ over time we differentiate between two cases of the forcing function. One case is for the impulsive force, which is a delta function in time,

$$f_i(z,t) = \delta(z)\,\delta(t). \tag{4.16}$$

The Green's function is given by

$$G_i(z,t) = \frac{1}{2c}\theta(t)\left[\underbrace{\theta(z+ct)}_{\Leftarrow} - \underbrace{\theta(z-ct)}_{\Rightarrow}\right], \tag{4.17}$$

where the two terms in the solution stands for the wave propagating along the positive and negative direction of z axis respectively.

The other case is for the displacive force, which is a Heaviside step function in time,

$$f_d(z,t) = \delta(z)\,\theta(t). \tag{4.18}$$

The Green's function is readily obtained by integrating G_i in Eq. (4.17),

$$G_d(z,t) = \frac{1}{2c^2}\theta(t)\left[\underbrace{g(z+ct)}_{\Leftarrow} - \underbrace{2g(z)}_{\Downarrow} + \underbrace{g(z-ct)}_{\Rightarrow}\right], \tag{4.19}$$

where function $g(z)$ is defined as

$$g(z) = z\,\theta(z). \tag{4.20}$$

In addition to the two propagation terms as in the case of impulsive force, there is also a third term which is constant in time and sits right in the range of the multiple quantum well where the force function is nonzero.

In our multiple quantum well system, the photogenerated carriers will persist for a certain amount of time to give a displacive forcing function $S(z,t) = f(z)\theta(t - t_0)$. Thus the lattice displacement can be written as

$$U(z,t) = \int_{-\infty}^{\infty} \mathrm{d}\zeta \, G_d(z-\zeta, t-t_0)\, f(\zeta). \tag{4.21}$$

The only nonzero component of the elastic strain η_{33} is obtained from the derivative of the lattice displacement with respect to space coordinate z,

$$\eta_{33}(z,t) = \frac{\partial U(z,t)}{\partial z}. \tag{4.22}$$

The kinetic and potential energy density u_k and u_p according to definition can be obtained from the derivatives of the lattice displacement with respect to time and space coordinate respectively,

$$u_k(z,t) \;\propto\; \left(\frac{\partial U(z,t)}{\partial t}\right)^2, \tag{4.23}$$

$$u_p(z,t) \;\propto\; \eta_{33}^2(z,t) = \left(\frac{\partial U(z,t)}{\partial z}\right)^2. \tag{4.24}$$

If we substitute the displacive Green's function into the displacement equation and then calculate the kinetic energy density, we will obtain for $t_0 = 0$

$$u_k(z,t) \propto \theta(t) \left\{ \int_{-\infty}^{\infty} \mathrm{d}\zeta \, [\theta(z+ct-\zeta) - \theta(z-ct-\zeta)] f(\zeta) \right\}^2, \tag{4.25}$$

where only two propagating term appear because

$$\frac{\mathrm{d}}{\mathrm{d}z} g(z) = z\,\delta(z) + \theta(z) \tag{4.26}$$

and the integral of the first term with a Dirac δ-function is zero.

We can calculate the following integral

$$\begin{aligned} & \int_{-\infty}^{\infty} \mathrm{d}\zeta\, \theta(z-\zeta)\, f(\zeta) \\ = & \int_{-\infty}^{\infty} \mathrm{d}\zeta\, \theta(\zeta)\, f(z-\zeta) \\ = & \int_{0}^{\infty} \mathrm{d}\zeta\, f(z-\zeta) \\ \equiv & \; F(z), \end{aligned}$$

and the kinetic energy density will be

$$u_k(z,t) \propto \theta(t)\left[F(z+ct) - F(z-ct)\right]^2. \tag{4.27}$$

Similarly we can obtain the potential energy density

$$u_p(z,t) \propto \theta(t)\left[F(z+ct) - 2F(z) + F(z-ct)\right]^2. \tag{4.28}$$

From the above equations we can see that if $F(z)$ is an oscillating function with a certain frequency then the kinetic energy density will oscillate with a doubled frequency because it is the square of two oscillating functions, but the potential energy will have the same frequency as $F(z)$ due to the interferenc term between the static $F(z)$ and the propagating $F(z+ct)$ and $F(z-ct)$.

The total energy density is just the sum of the kinetic and potential part,

$$u(z,t) = u_k(z,t) + u_p(z,t). \tag{4.29}$$

The total energy E as a function of time is obtained by integrating the total energy density over the whole z axis,

$$E(t) = E_k(t) + E_p(t) = \int_{-\infty}^{\infty} \left[u_k(z,t) + u_p(z,t)\right] \mathrm{d}z. \tag{4.30}$$

If the forcing function is limited in some region with length L, then the kinetic energy will remain constant after $t = L/2c$ at which time the two oppositely

propagating parts does not cover each other anymore. The wave form does not change with the propagation, so the integral over the whole z-axis will remain constant $t = L/2c$. However the potential energy density will not become a constant until $t = L/c$ which is twice the time of the kinetic energy density because the static part combined with the propagating part will keep changing until the propagating part is totally outside the forcing function region which gives the time L/c.

Since the numerical calculation of microscopic theory [27] uses a multiple quantum well of four periods, we will first consider the four-period case for comparison.

Figure 4–3 shows the forcing function obtained from the microscopic model [27] and a simple sinusoidal forcing function used in the string model. The common features of both forcing function are their oscillations and periodicity in the range of the multiple quantum wells.

In Fig. 4–4 we show the displacement of the lattice calculated from the string model using the simple four-period sinusoidal function shown in Fig. 4–3. It shows clearly the propagating parts of the motion and the static part inside the multiple quantum well system that remains behind when the dynamic parts travel outside the quantum wells region.

From the displacement we can calculate the strain, which is shown in Fig. 4–5. The image of strain again shows clearly the propagation of the wave motion.

Figure 4–6 shows the total energy density calculated from the string model. It has the very similar wave propagating features as shown in the lattice displacement and strain figures.

We plot the energy as a function of time from the string model in Fig. 4–7. It has four peaks and four periods of oscillation, which is the same as the number of multiple quantum well periods. It also shows that the kinetic energy oscillates

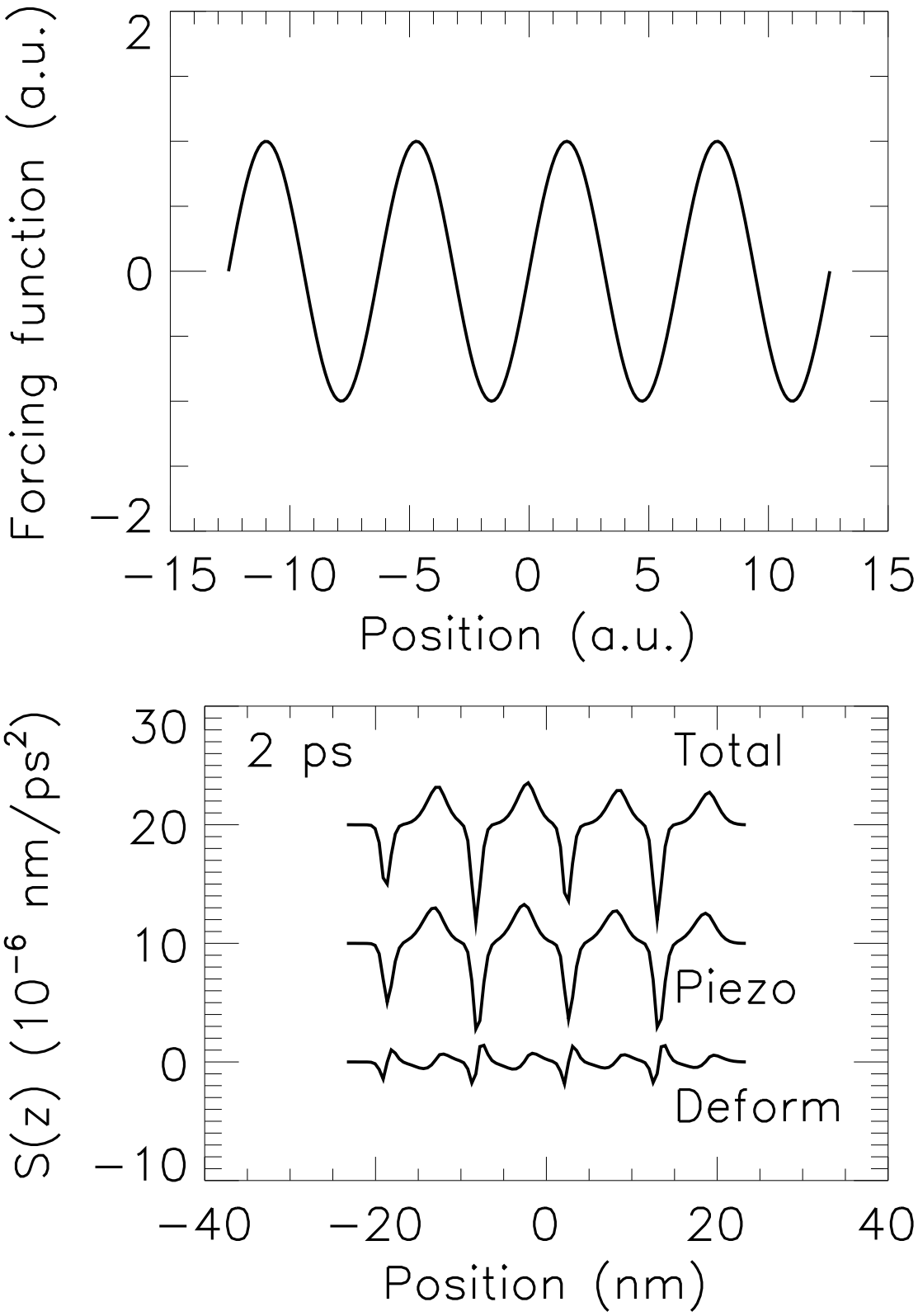

Figure 4–3: Forcing functions. The upper one is a sinusoidal function of four periods corresponding to a four-period MQW. The lower one is from the numerical calculation of the microscopic theory, [See Sanders et al., PRB, 64:235316, 2001].

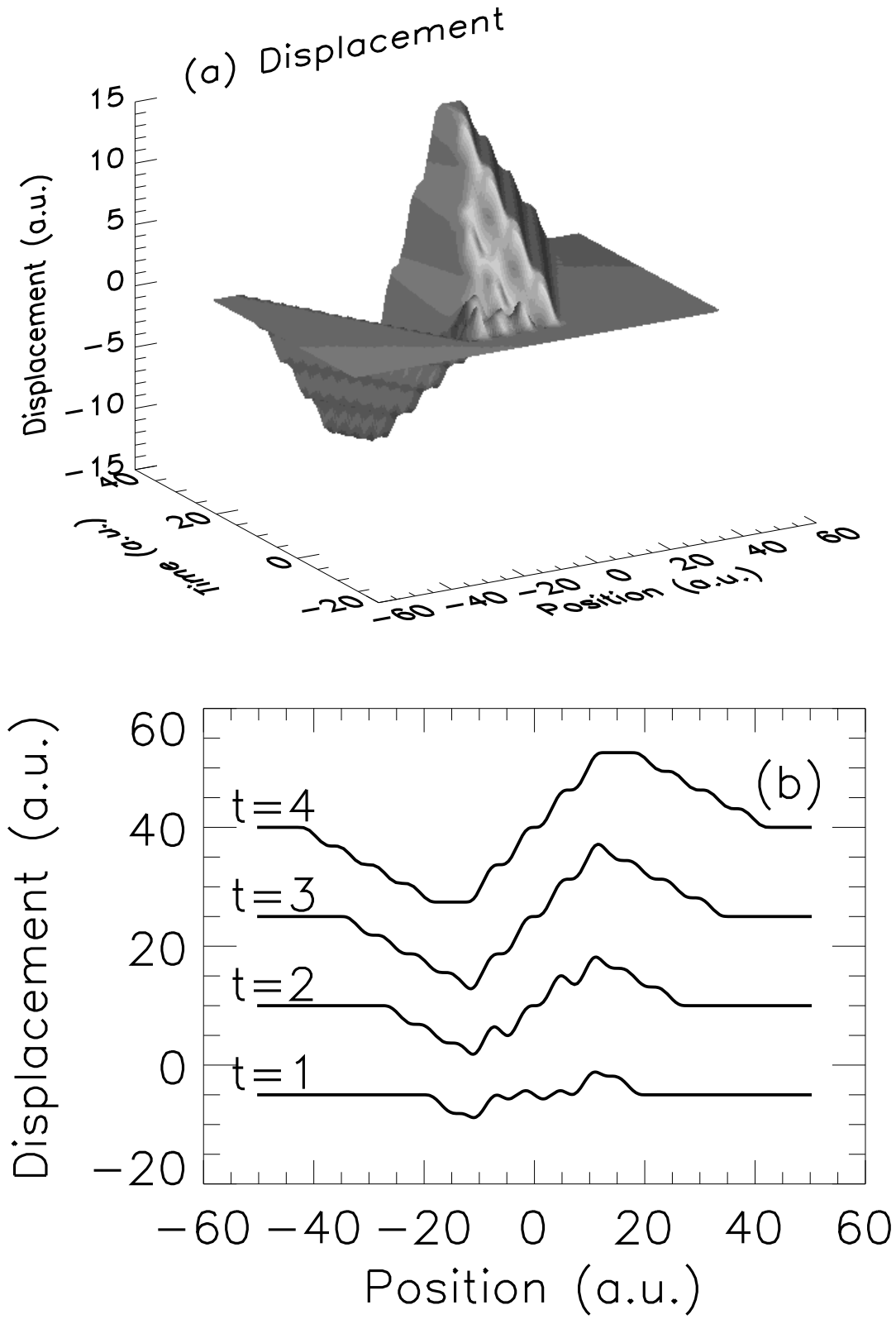

Figure 4–4: Displacement as a function of position and time. It is the solution of wave equation with the simple four-period sinusoidal force shown in Fig. 4–3

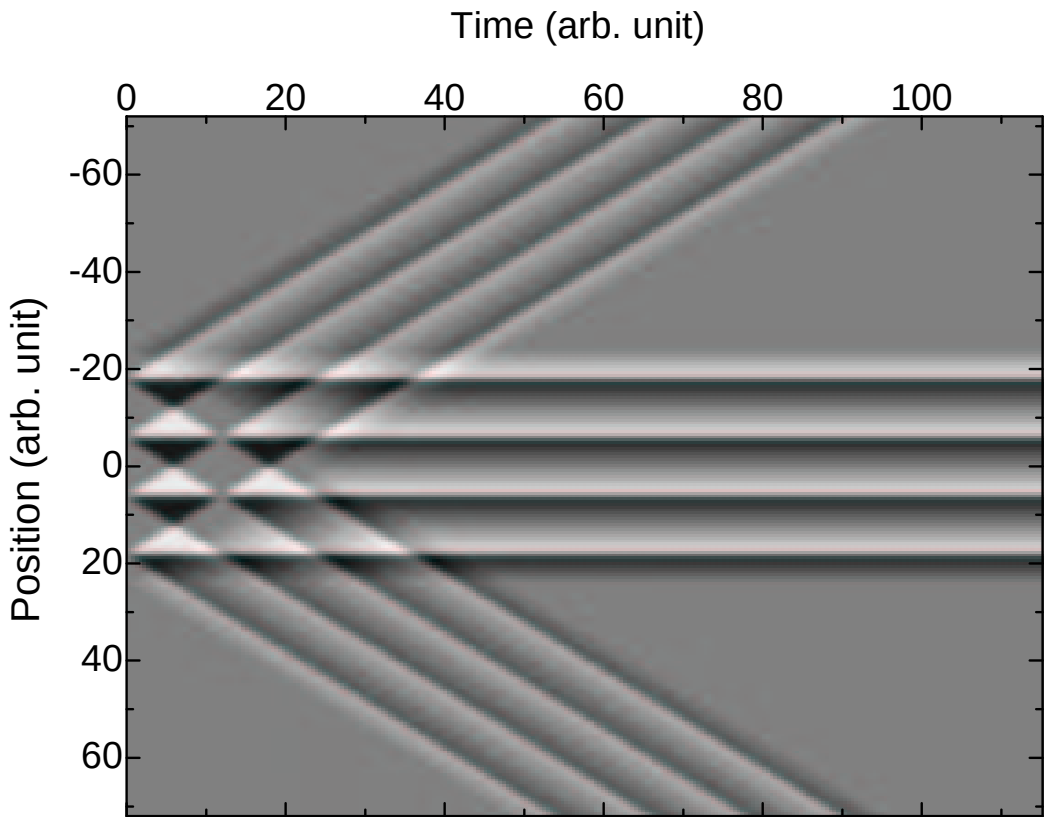

Figure 4–5: The image of strain as a function of position and time from the string model.

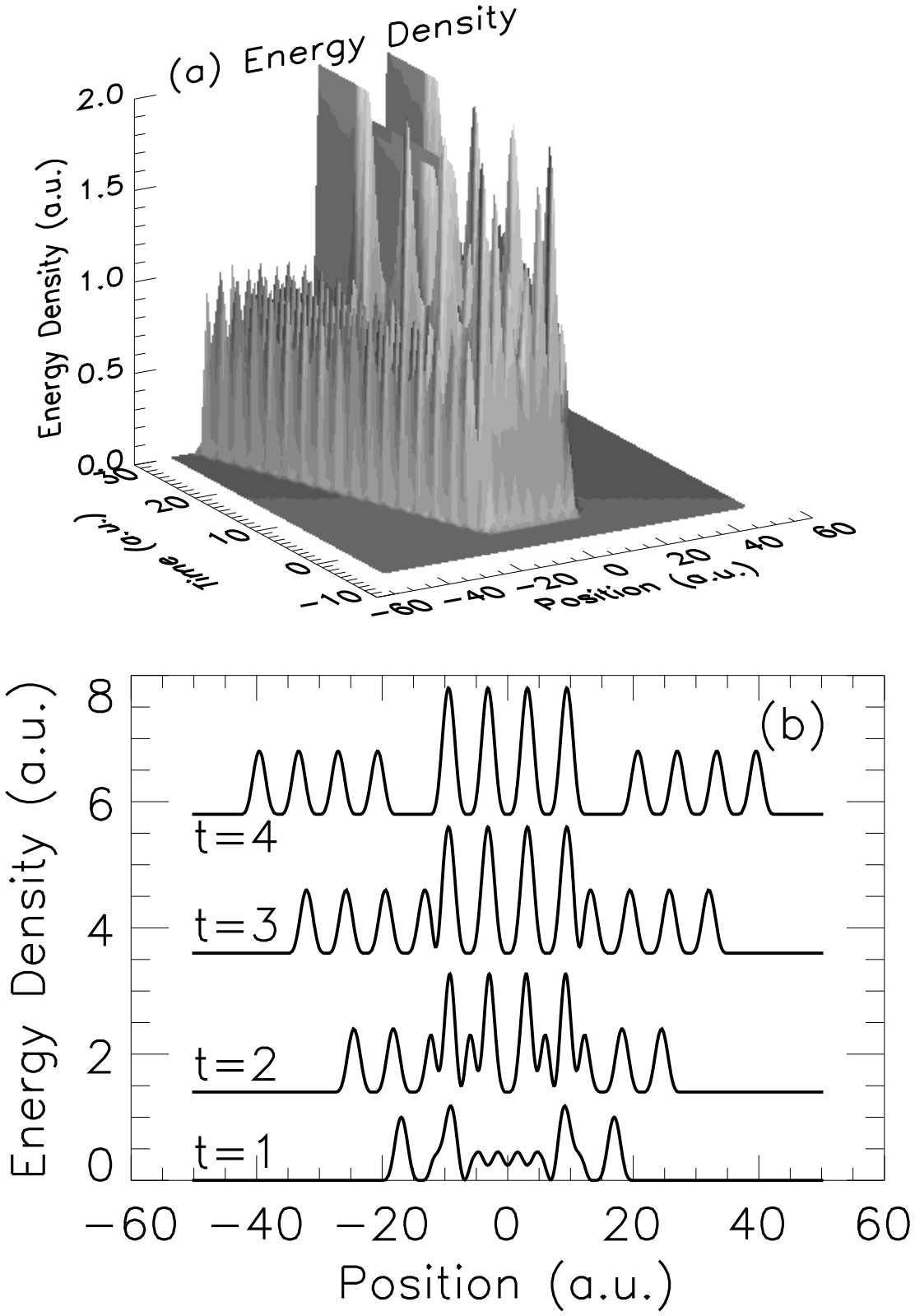

Figure 4–6: Energy Density as a function of position and time. After a long time (t=4 here), the energy density divides into a static part and a traveling part

at twice the frequency of the potential energy and the time for the oscillation to die out of kinetic energy is half of the potential energy as discussed in Eq. (4.30). The total energy changes with time because we have treated the driving force as an external one. If we treat the driving force as internal, then the system will have a new equilibrium configuration, around which the calculated energy will be conserved.

For the case of a multiple quantum well system of fourteen periods, the energy is plotted in Fig. 4–8. The energy plot has fourteen peaks and it dies out after fourteen periods of oscillation. Again the number of peaks and the number of oscillations is the same as the number of periods in the multiple quantum well system.

The energy plot can be viewed in two ways. In the real space the wave will propagate with the acoustic sound speed in both directions of the z axis. After the wave travels totally out of the range of the multiple quantum well, the energy stops changing and remains constant, which explain the die out of the oscillation. The number of wells is like the number of sources of force. The waves they induce superimpose and gives the number of oscillations in the energy.

In the wavevector space, because the periodic forcing function is confined in a limited range of multiple quantum wells, the wavevector q will have some uncertainty Δq. Thus the angular frequency ω of the coherent acoustic phonon oscillation will also have an uncertainty $\Delta\omega$ with $\Delta\omega/\omega = \Delta q/q$. It is this uncertainty $\Delta\omega$ that leads to a dephasing of the oscillation. Since the more periods of quantum wells and the greater extent of the system will produce a smaller uncertainty Δq. So the die-out time of oscillation is related to the number of quantum wells, more specifically it is related to the total length of MQWs divided by the sound velocity in the MQWs.

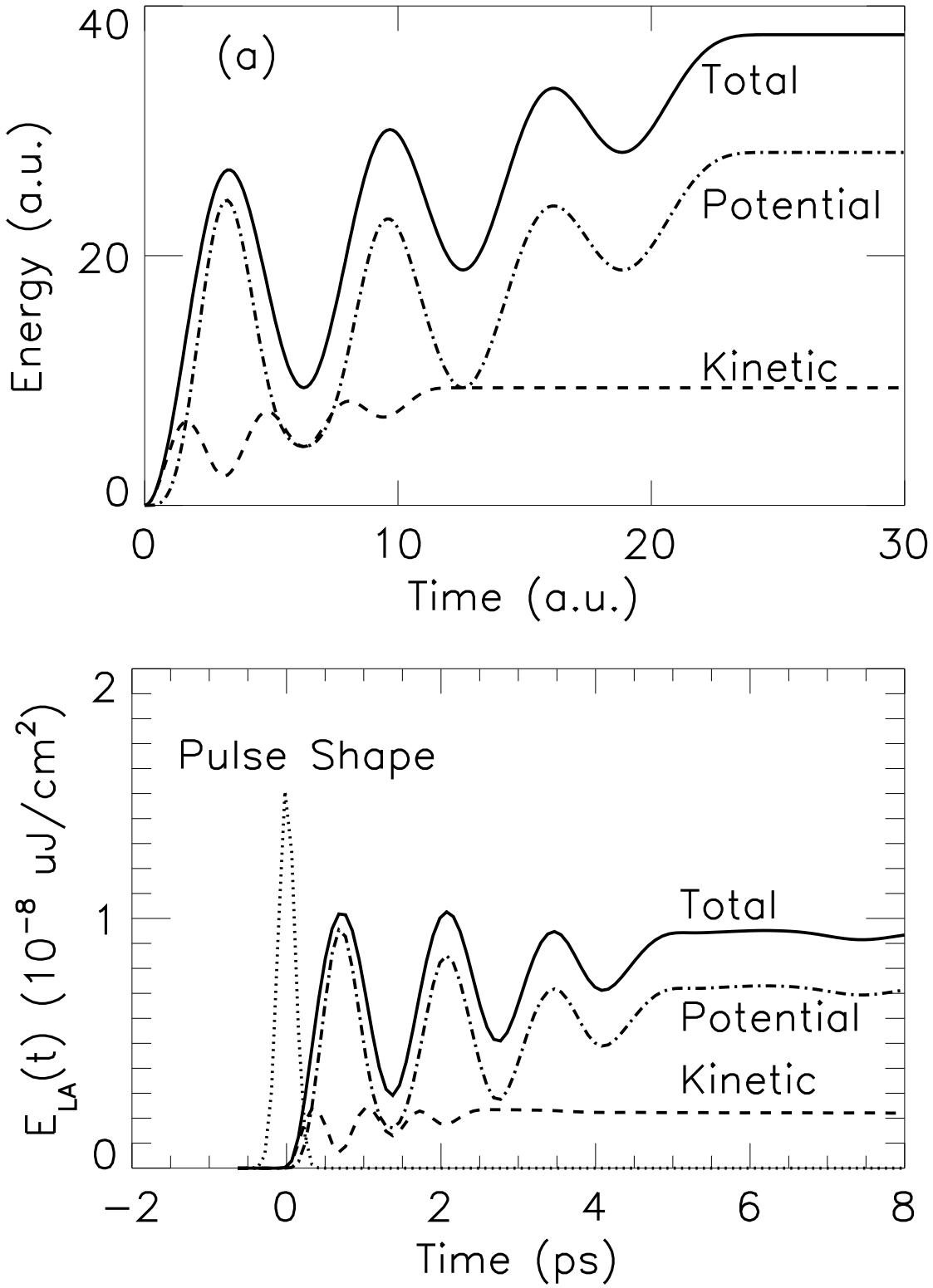

Figure 4–7: Energy as a function of time for 4 quantum wells. The number of peaks of total energy equals the number of wells. The kinetic energy oscillates twice fast as the potential energy. (b) is from calculation of microscopic theory, see [See Sanders et al., PRB, 64:235316, 2001].

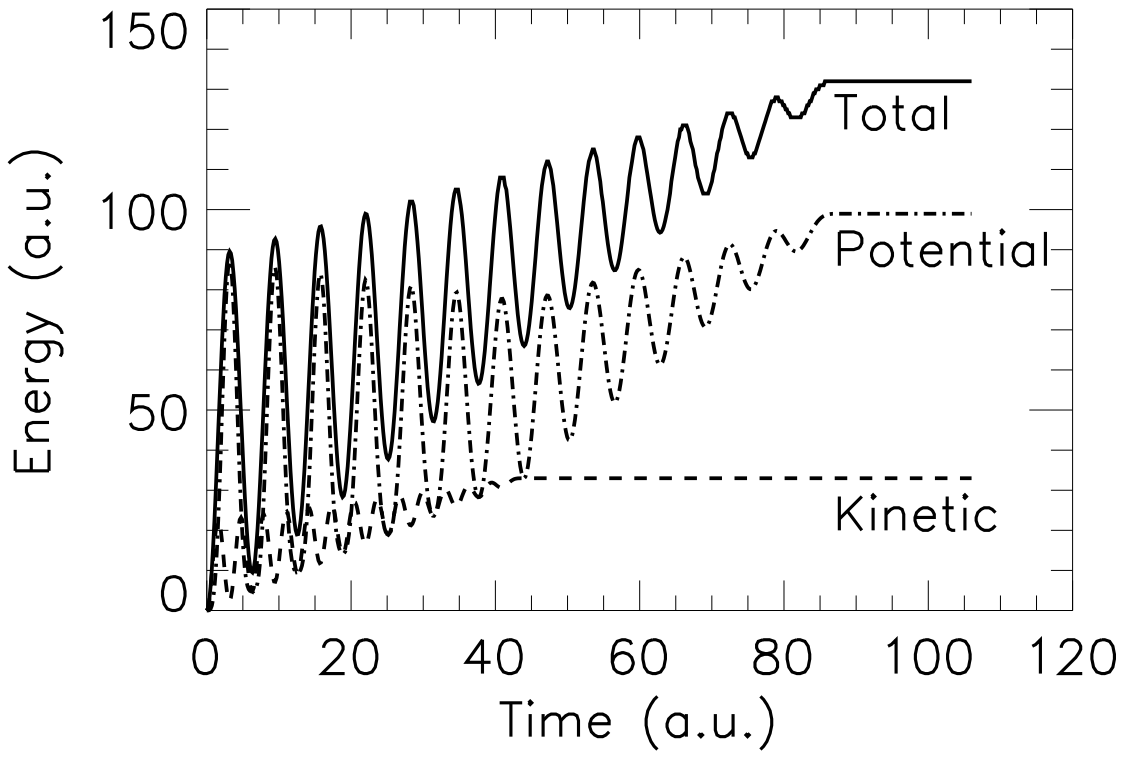

Figure 4–8: Energy as a function of time for 14 quantum wells. This figure shows the same features as that of figure 4–7(a).

4.4 Coherent Control

In recent years there are quite a few coherent control experiments with multiple quantum wells from several different groups such as Sun [31], Özgür [32], and Nelson [33]. In InGaN/GaN multiple quantum wells the effect is more prominent because of the stronger piezoelectric field.

By using double-pulse pump excitation Dekorsy et al. showed the controlling of the amplitude of the coherent optical phonons in GaAs [34]. Hase et al. conducted this kind of optical control of coherent optical phonons in bismuth films [35]. Bartels et al. reported coherent control of acoustic phonons in semiconductor superlattices [36].

In these experiments, the pulse train of pump laser was splited into two or more beams that travels different optical path distances by means such as Michelson interferometer. The sample will excited twice or more at different times. The changes in reflectivity were measured the same as the pump-probe setup.

The results from these experiments show that the coherent phonons can interfere with each other and can be coherently controlled by using multiple optical pump trains. Depending on different phase delays of pump pulses, the coherent oscillation can be enhanced or annihilated.

In this section I will use the string model to analyze the coherent control of coherent acoustic phonons. In the generation of coherent acoustic phonons, the ultrafast laser pump generates electron-hole pairs, which is the source of the forcing function. In the string model we use a simplified sinusoidal forcing function to replace the microscopic one. The coherent control uses two pump pulses, which mean we will have two forcing functions. In experiments, one can control the time interval between the two pump pulses. Theoretically, we can control not only the time interval between the start time of the two forcing function but also the phase difference between them. Based on the string model, we can try coherent control

theoretically by using a forcing function with two terms. The first forcing term takes effect at time $t = 0$ and the second forcing term appears at a later time $t = t_0$ with a relative spatial phase z_0 and amplitude A with respect to the first term. Note that while the first forcing term corresponds directly to the excitation pump, the relation between the second forcing term and the control pulse is not so direct and clear because the second forcing term will depend on both the excitation pump and the control pulse.

The forcing functions have the form $A\,\sin(z - z_0)\,\theta(t - t_0)$, describing displacive forces starting at time t_0 and having an initial phase of z_0. The amplitude A is taken as unit for the first force. But the second force may have a relative larger or smaller amplitude.

The phase effects have two aspects. One is the temporal phase effect due to the time interval between the two forcing terms. The other is the spatial effect caused by the relative initial phase difference between the spatial parts of the two forcing terms.

First let us consider the effects of the temporal phase and the relative amplitude. The total forcing function can be written down as

$$S(z, t) = \sin(z)\,\theta(t) + A\,\sin(z)\,\theta(t - t_0). \tag{4.31}$$

When the time intervals t_0 are even multiples of π, the two terms in the forcing function will be temporally in phase. In the cases of $t_0 = (2n + 1)\pi$ with n being an integer, the two terms will be temporally out of phase. To save numerical computation time without losing any features we calculate the potential energies only which are proportional to the square of the strain.

Figure 4–9 shows the temporally in-phase *constructive* enhancement of the oscillations. The time interval in this case is 4π, the relative amplitudes of the second forcing term are 1.5, 1, and 0 respectively. The lowest curve with zero

relative amplitude means that there is only one forcing term. We see that no matter what the relative amplitudes are the constructive enhancement effects are always there.

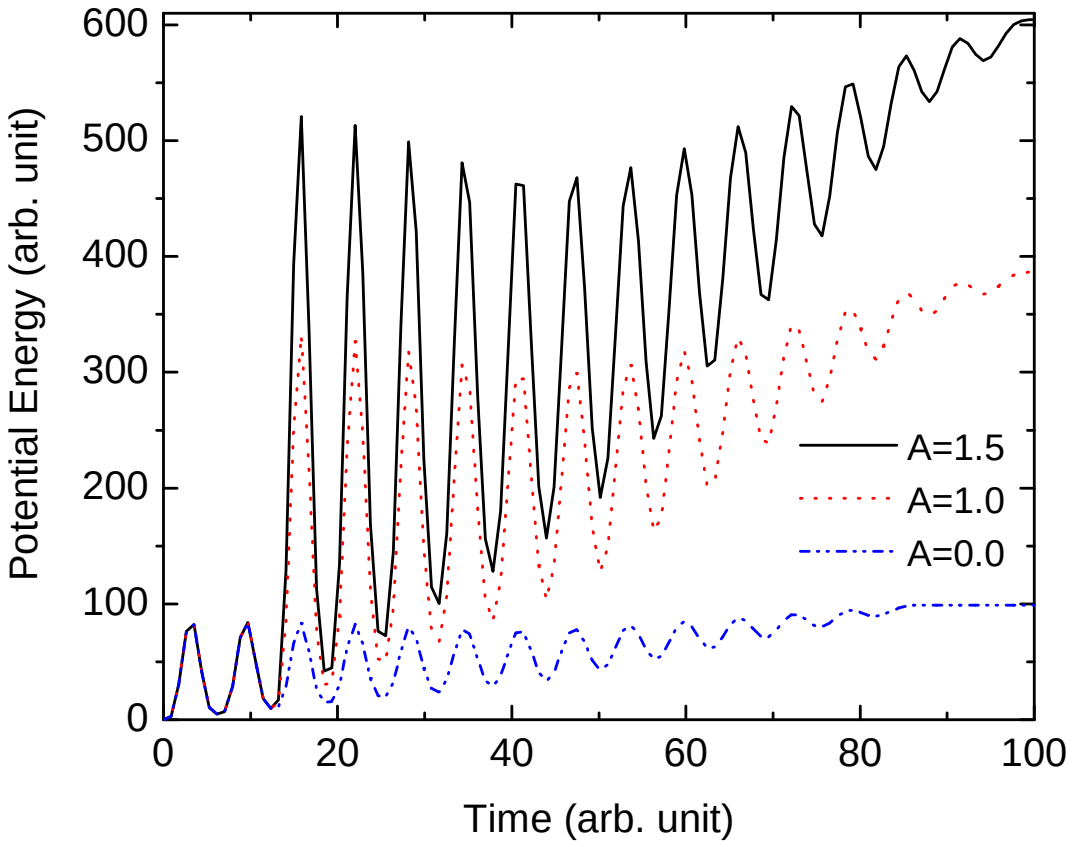

Figure 4–9: Potential energy as a function of time for 14 quantum wells with two forcing terms delayed by an in-phase time interval of 4π. This figure shows the constructive enhancement of the oscillations as a result of coherent effect of the two forcing terms.

The *destructive* effects of two temporally out of phase forcing terms are plotted in Fig. 4–10. The lowest curve is for one forcing term only. The other three curves have the relative amplitudes 0.7, 1, and 1.5 respectively. The destructive effect is most obvious when the relative amplitude of the second force is smaller than the first, while for larger amplitudes the oscillations reduces but does not disappear. Since the coherent phonon oscillations have a tendency to dephase, the oscillations

will become smaller with time. To further reduce the oscillation amplitudes the second pump pulse does not need to be stronger. It does not need even to reach the same strength as the first one. This is why the case of a force with relative amplitude $A = 0.7$ has the strongest destructive effect.

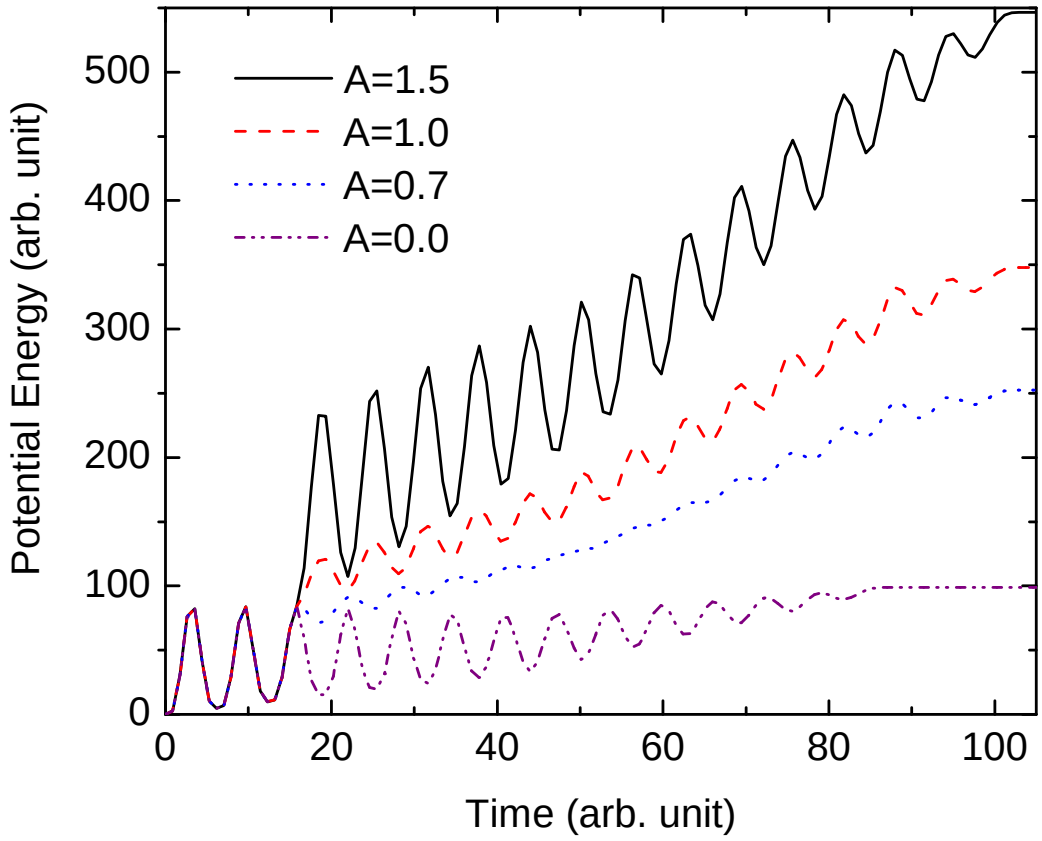

Figure 4–10: Potential energy as a function of time for 14 quantum wells with two forcing terms delayed by an out of phase time interval of 5π. This figure shows the destructive effect of the oscillations as a result of coherent control by two forcing terms.

Using the formalism discussed in Chapter 3 we can calculate the differential transmission. To further simplify the matter, the sensitivity function is taken to be a constant in the wells. Outside of the wells it is zero. Fig. 4–11 shows the constructive and destructive effects of the two forcing terms as discussed above.

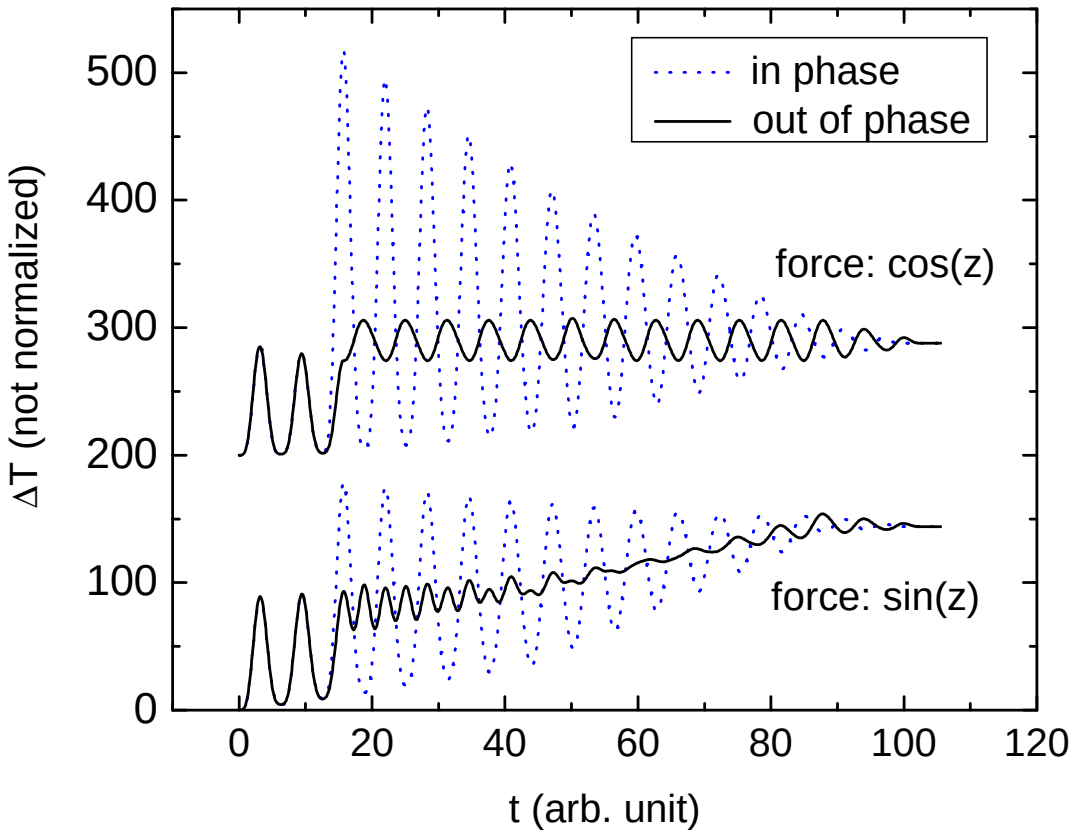

Figure 4–11: The change of transmission as a function of time for 14 quantum wells with two forcing terms delayed by an in phase time interval of 4π and an out of phase time interval of 5π. The upper and lower two sets of curves are displaced with regard to each other for a better view.

The temporal phases, i.e. the time intervals between the two forces, are easy to control experimentally by varying the optical path of the two pump pulses, but the control of the spatial phases z_0 is not so obvious. In theory, however, it is not hard to observe the effects of spatial phases z_0 on the coherent control.

We will take the amplitudes of the two forces to be the same. If we keep the temporally in phase time interval as $t_0 = 4\pi$, then we can have four typical cases of the two forcing term.

Case I1: $S(z,t) = \cos(z)\,\theta(t) + \cos(z - \frac{\pi}{2})\,\theta(t - 4\pi)$.

Case I2: $S(z,t) = \cos(z)\,\theta(t) + \cos(z - \pi)\,\theta(t - 4\pi)$.

Case I3: $S(z,t) = \cos(z)\,\theta(t) + \cos(z - \frac{3\pi}{2})\,\theta(t - 4\pi)$.

Case I4: $S(z,t) = \cos(z)\,\theta(t) + \cos(z)\,\theta(t - 4\pi)$.

These cases are plotted in Fig. 4–12.

We have already discussed case (I4) in the above, which is the constructive temporally in phase enhancement of the oscillations. For case (I2) at time $t > 4\pi$, the sum of the two forcing terms will give a zero total forcing function. As a result, the oscillation will totally disappear.

In cases (I1) and (I3) the spatial part of the total forcing function is given by $\cos(z) \pm \sin(z)$. The amplitudes of the oscillations for these two cases are not as big as the coherent case (I4) where the phases lock in both temporally and spatially. Thus for temporally in phase time interval, if the spatial phases are between the two extremes of in phase and out of phase as shown in case (I4) and (I2) respectively, the enhancement of the oscillations will also vary between the totally coherent and the totally destructive.

There are four similar cases for the temporally out of phase time interval. Again we take $t_0 = 5\pi$. The four cases are listed below.

Case O1: $S(z,t) = \cos(z)\,\theta(t) + \cos(z - \frac{\pi}{2})\,\theta(t - 5\pi)$.

Case O2: $S(z,t) = \cos(z)\,\theta(t) + \cos(z - \pi)\,\theta(t - 5\pi)$.

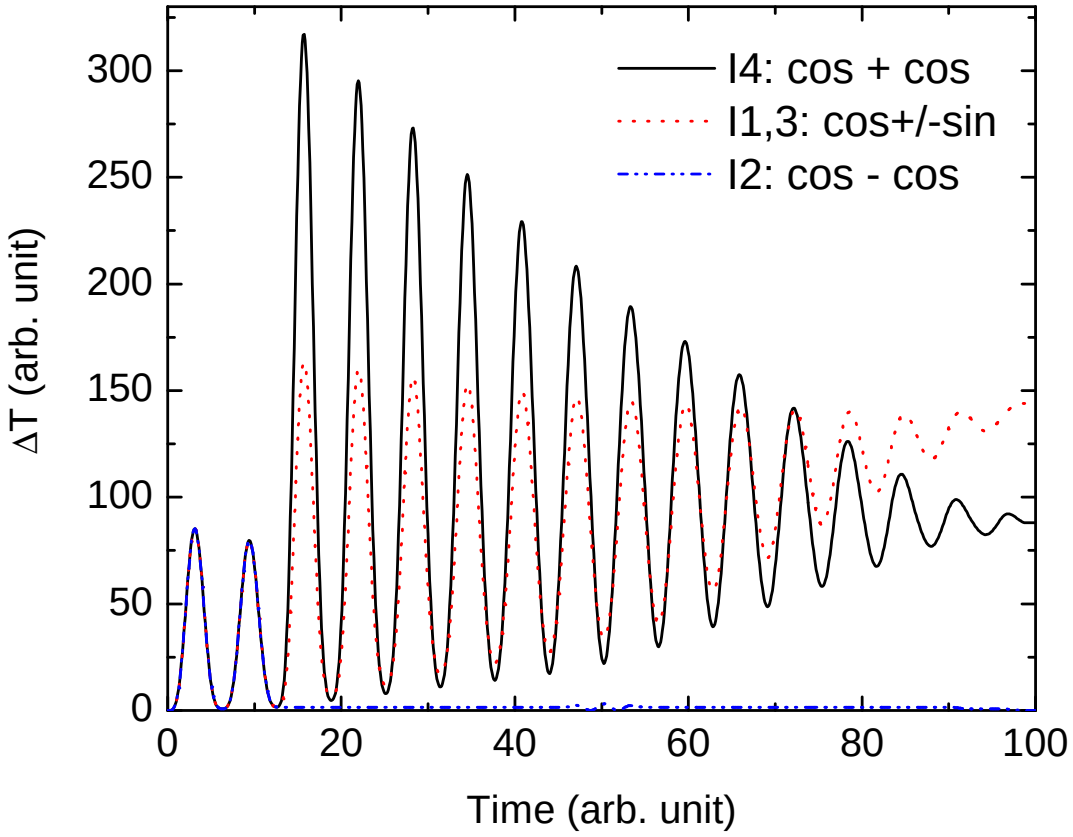

Figure 4–12: Effects of phase z_0 on the change of transmission as a function of time for 14 quantum wells. The two forcing terms are delayed by an in phase time interval of 4π. The different curves are for different combination of phases z_0 as discussed in the text.

Case O3: $S(z,t) = \cos(z)\,\theta(t) + \cos(z - \frac{3\pi}{2})\,\theta(t - 5\pi)$.

Case O4: $S(z,t) = \cos(z)\,\theta(t) + \cos(z)\,\theta(t - 5\pi)$.

Figure 4–13 shows the changes of transmissions for these four temporally out of phase cases. In cases (O1), O(3), and (O4) the spatial part of the total forcing function is the same as the corresponding temporally in phase cases, i.e., $\cos(z) \pm \sin(z)$ and we see the expected destructive effects of the oscillations, although the reduction is not drastic because the relative amplitude of the second forcing term is as big as the first.

For the spatially out of phase case (O2) the total forcing function is identically zero at times $t > t_0 = 5\pi$, but the oscillation persists, which is a distinct contrast to the corresponding case (I2). In case (I2) the oscillation almost totally disappear after the second temporally in phase force comes in because at time $t = t_0 = 4\pi$ the oscillation reaches one of its lowest points the value of which is nearly zero. However, in case (O2) at the starting time $t = t_0 = 5\pi$ the oscillation is at one of its highest point. Although from then on there is no forces any more, the oscillation will keep on like a free oscillator. Note that we have not taken into consideration of any damping force, but the oscillation still dies out. The dephasing time is about a half of that of the one forcing term case. This dephasing effect, as we mentioned before, is due to the limited range of the multiple quantum well system.

4.5 Summary

We have discussed briefly a microscopic theory for the generation and detection of coherent acoustic phonons in GaN/InGaN multiple quantum well system. Following the outlined procedures we arrive at a set of coupled differential equations of motion for the electron density matrices and coherent phonon amplitude. The latter ones can be mapped onto a one-dimensional wave equation called the

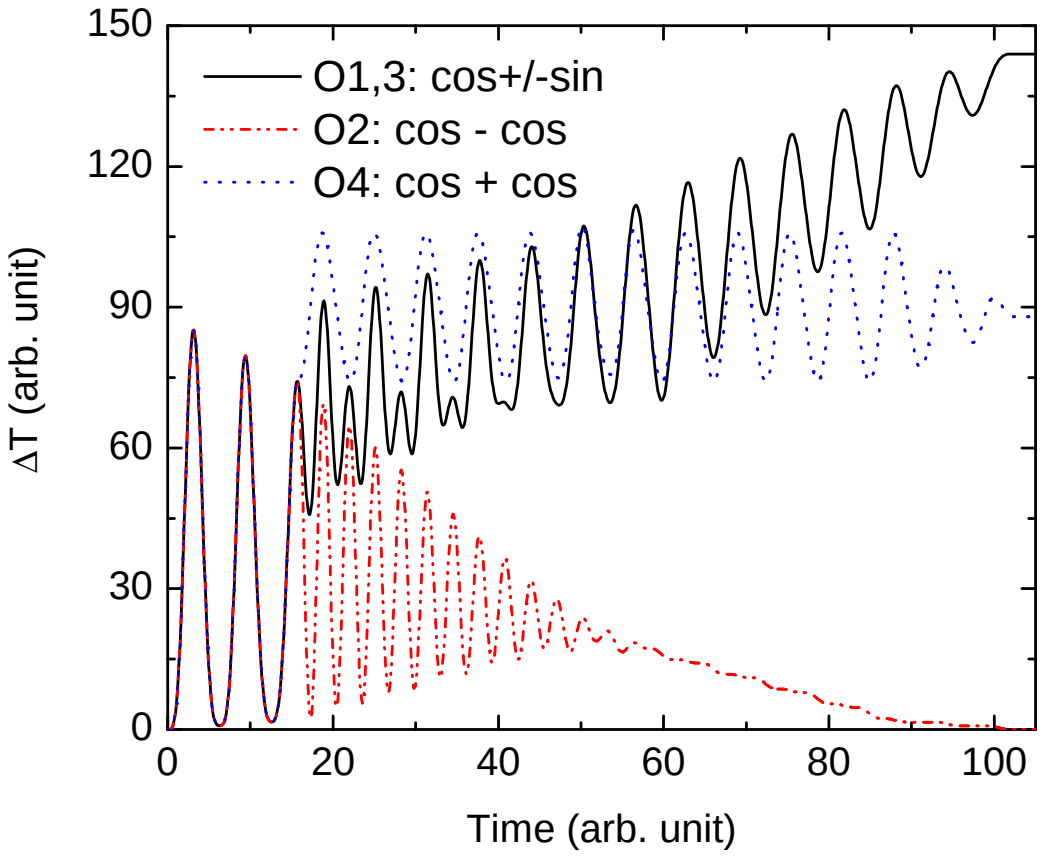

Figure 4–13: Effects of phase z_0 on the change of transmission as a function of time for 14 quantum wells. The two forcing terms are delayed by an out of phase time interval of 5π. The different curves are for different combination of phases z_0 as discussed in the text.

string model, which describes the motion of a uniform string under a non-uniform forcing function.

We can solve the string model using Green's function method to obtain the lattice displacement and other related physical quantities such as strain, energy density, energy, and the differential transmission. All these quantities have the oscillating property. The strain and energy density propagate in both directions along the superlattice growth axis z. The oscillations of energy and differential transmission have the same number of peaks as the number of the wells and they dies out because of the limited range of the multiple quantum well system.

Another interesting application of the string model is coherent control of these coherent acoustic phonons. By using two forcing terms corresponding to two pump pulses, we can change three elements of the second forcing term with respect to the first, the temporal phase, the spatial phase, and the relative amplitude. The temporal phase is the most effective control. We have shown both the temporally in phase constructive and out of phase destructive enhancement. To get better destructive effect the relative amplitude of the second forcing term should be small than the first. In spatially out of phase cases the total forcing function will be zero after the starting time of the second forcing term, but there is a distinctive contrast between the temporally in phase and out of phase cases. In the former case the oscillation almost disappear, while in the latter case the oscillation persists with a dephasing time a half of the case when there is only one forcing term.

CHAPTER 5
PROPAGATING COHERENT PHONON

Heterostructures of GaN and InGaN are important materials owing to their applications to blue laser diodes and high power electronics [6]. Strong coherent acoustic phonon oscillations have recently been detected in InGaN/GaN multiple quantum wells [26, 37]. These phonon oscillations were much stronger than folded acoustic phonon oscillations observed in other semiconductor superlattices [24, 25, 38].

InGaN/GaN heterostructures are highly strained at high In concentrations giving rise to large built-in piezoelectric fields [39, 40, 41, 42], and the large strength of the coherent acoustic phonon oscillations was attributed to the large strain and piezoelectric fields [26].

In this chapter, we discuss the generation of strong localized coherent phonon wave-packets in strained layer $In_xGa_{1-x}N$/GaN epilayers and heterostructures grown on GaN and Sapphire substrates [43]. This work was done in cooperation with Gary D. Sanders, Christopher J. Stanton, and Chang Sub Kim. The experiments were performed by J. S. Yahng, Y. D. Jho, K. J. Yee, E. Oh and D. S. Kim. (See cond-mat/0310654.)

By focusing high repetition rate, frequency-doubled femtosecond Ti:Sapphire laser pulses onto strongly strained InGaN/GaN heterostructures, we can, through the carrier-phonon interaction, generate coherent phonon wavepackets which are initially localized near the epilayer/surface but then propagate away from the surface/epilayer and through a GaN layer. As the wavepackets propagate, they modulate the local index of refraction and can be observed in the time-dependent differential reflectivity of the probe pulse. There is a sudden drop in the amplitude

of the reflectivity oscillation of the probe pulse when the phonon wave-packet reaches a GaN-sapphire interface below the surface. Theoretical calculations as well as experimental evidences support this picture; the sudden drop of amplitude when the wave encounters the GaN-sapphire interface cannot be explained if the wave-packet had large spatial extent. When the wave-packet encounters the GaN-sapphire interface, part of the wave gets reflected while most of it gets transmitted into the sapphire substrate, depending on the interface properties and the excess energy of the exciting photons. This experiment illustrates a non-destructive way of generating high pressure tensile waves in strained heterostructures and using them to probe semiconductor structure below the surface of the sample. Since the strength of this non-destructive wave is determined by the strain between GaN and InGaN, it is likely that even stronger coherent phonons can be generated in InGaN/GaN digital alloys grown on a GaN substrate.

5.1 Experimental Results

In the experiments, frequency-doubled pulses of mode-locked Ti:sapphire lasers are used to perform reflective pump-probe measurements on four different sample types which are shown in Fig. 5–1: Type (I) InGaN epilayers; Type (II) InGaN/GaN double quantum wells (DQWs); Type (III) InGaN/GaN single quantum well (SQW); and Type (IV) InGaN/GaN light-emitting diode (LED) structures. The peak pump power is estimated to be 400 MW/cm^2, corresponding to a carrier density of 10^{19} cm^{-3} and the doubled pulse width is 250 fs. All samples were grown on a *c*-plane sapphire substrate by metal organic chemical vapor deposition. The InGaN epilayers shown in Fig. 5–1(a) consist of 1 μm GaN grown on a sapphire substrate and capped with 30 nm of $In_xGa_{1-x}N$ with In composition, x, varying from 0.04 to 0.12. The DQW sample shown in Fig. 5–1(b) consists of GaN (1 μm), double quantum wells of $In_{0.12}Ga_{0.88}N$ (1–16 nm) and barrier of GaN (1–16 nm), and a GaN cap layer (0.1 μm). The SQW sample in Fig. 5–1(c) consists

of GaN (2 μm), $In_{0.12}Ga_{0.88}N$ (24 nm), and GaN cap layer (0.1 μm). The blue LED structure shown in Fig. 5–1(d) consists of n-GaN (4 μm), 5 quantum wells of $In_{0.15}Ga_{0.85}N$ (2 nm) and 4 barriers of GaN (10 nm), p-$Al_{0.1}Ga_{0.9}N$ (20 nm), and p-GaN (0.2 μm).

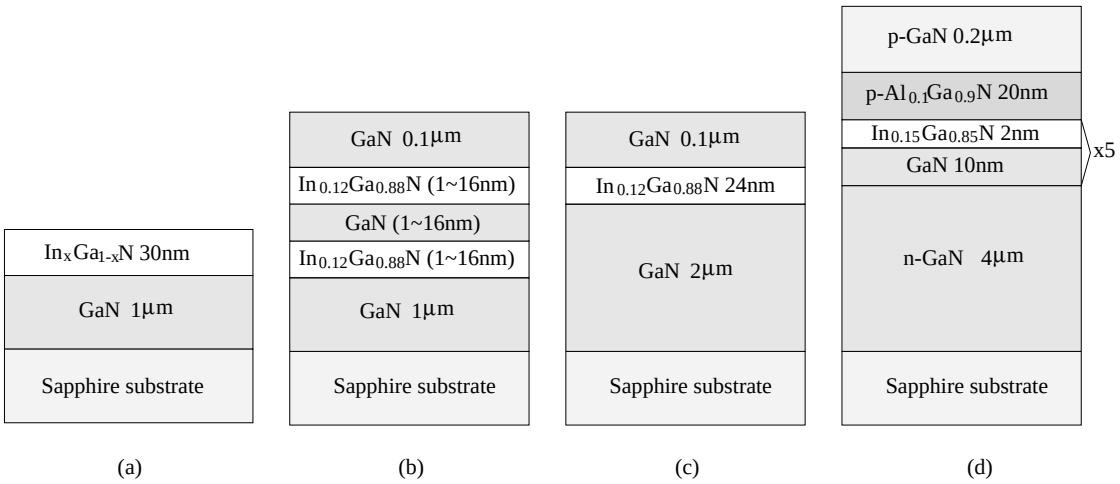

Figure 5–1: The simple diagram of the sample structures used in these experiments. (a)InGaN epilayer (type I), (b)InGaN/GaN double quantum wells (type II), (c)GaN single quantum well (type III), (d)InGaN/GaN blue light-emitting diode structure (type IV).

Differential reflection pump-probe measurements for the $In_xGa_{1-x}N$ epilayers are shown in Fig. 5–1(a). Fig. 5–2 shows the oscillatory component of the measured probe differential reflectivity for the InGaN epilayers (type I) with various In concentrations, x. For comparison purposes, differential reflectivity was measured on a pure GaN HVPE grown sample in order to show that no differential reflectivity oscillations are present in the absence of strain and an epilayer. The energy of the pump laser was varied between 3.22 and 3.35 eV, to keep the excess carrier energy above the InGaN band gap but below the GaN band gap. We note that if the laser energy was below the InGaN band gap, no signal was detected. *Therefore, carrier generation is essential to observing the oscillations, unlike a recent coherent optical phonon experiment in GaN* [44]. The inset shows the pump-probe signal prior to the background subtraction for $x = 0.12$. The background results from the

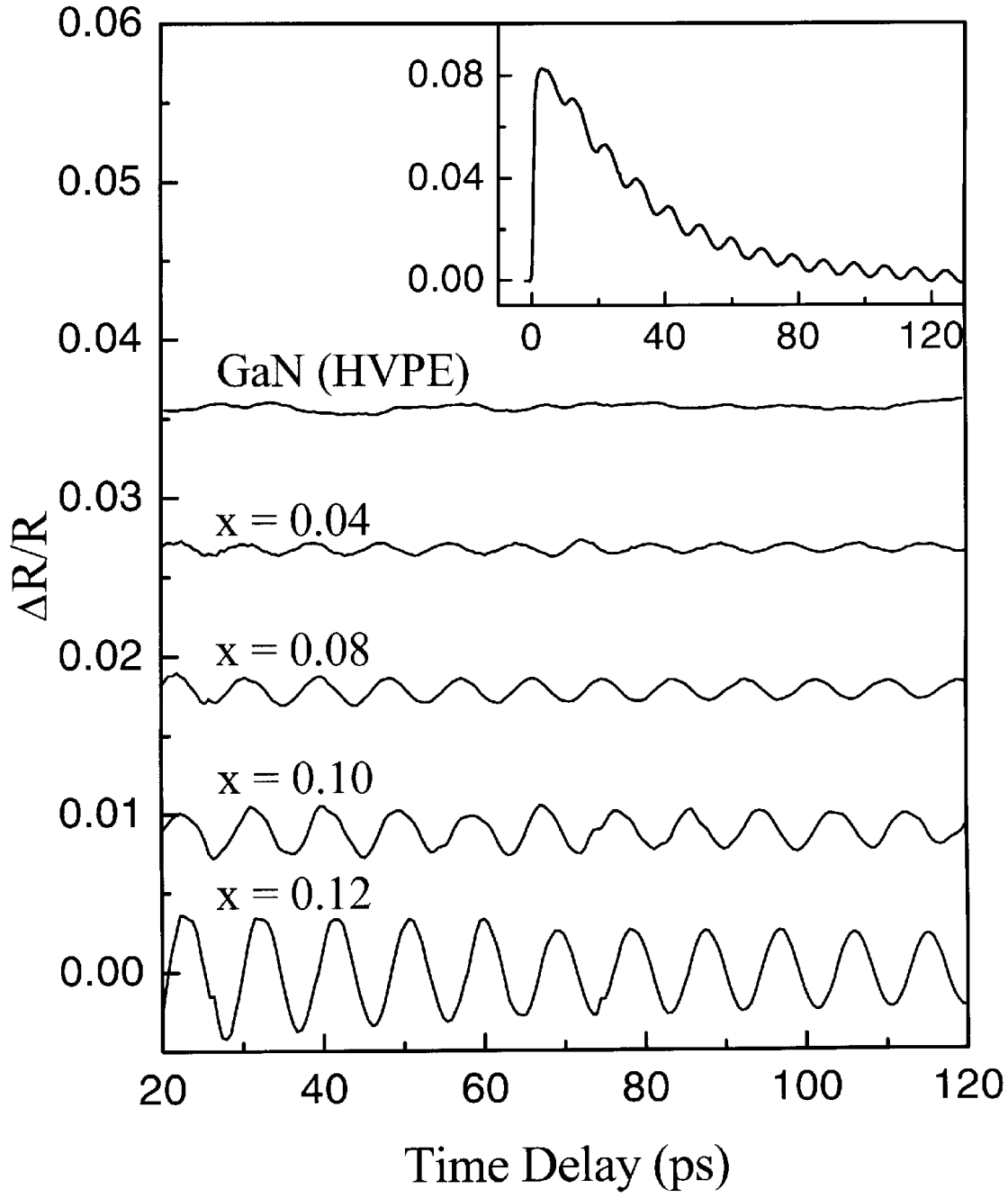

Figure 5–2: The oscillatory component of the differential reflection pump-probe data for the $In_xGa_{1-x}N$ epilayers with various In composition (x=0.04, 0.08, 0.10, and 0.12). For comparison, differential reflection in a pure GaN HPVE grown sample is shown. The reflection signal prior to the background subtraction for $x = 0.12$ is shown in the inset.

relaxation of the photoexcited electrons and holes. The oscillations are quite large, on the order of 10^{-2}–10^{-3} and the period is 8–9 ps, *independent* of the In composition but *dependent* on the probe photon energy. The amplitude of the oscillation is approximately proportional to the In concentration indicating that the strain at the InGaN/GaN interface is important. The observed period is approximately $\tau = \lambda/2C_s n$, where λ is the probe beam wavelength, C_s the longitudinal acoustic sound velocity, and n the refractive index of GaN [19].

Two-color pump-probe experiments were performed for a type III InGaN SQW sample as shown in Fig. 5–1(b). Fig. 5–3 shows the differential reflectivity oscillations for different probe energies. Note that the period of the oscillation changes *and is proportional to the probe wavelength*. In addition, the amplitude of the differential reflectivity oscillation decreases as the detuning (with respect to the pump) becomes larger. The inset shows the oscillation amplitude as a function of the probe energy in a logarithmic scale and there is an ∼2-order-of magnitude decrease in differential reflectivity when the probe energy changes from 3.26 eV to 1.63 eV.

Interestingly, Fig. 5–4 shows that the amplitude of the oscillatory component of the differential reflectivity is independent of the bias voltage, even though the carrier lifetime changes dramatically with voltage bias. Fig. 5–4 shows the bias dependent acoustic phonon differential reflectivity oscillations in a type IV blue LED structure (see Fig. 5–1(d)) at a pump energy of 3.17 eV. The lifetime of the background signal drastically decreases as the bias increases as shown in Fig. 5–4(a). This is due to the carrier recombination time and the decrease in the tunneling escape time in the strong external bias regime [45]. On the other hand, the amplitude and frequency of the oscillatory component of the differential reflectivity doesn't change much with bias voltage [Fig. 5–4(b)]. Since the observed reflectivity oscillation is independent of the carrier lifetime for lifetimes as short as

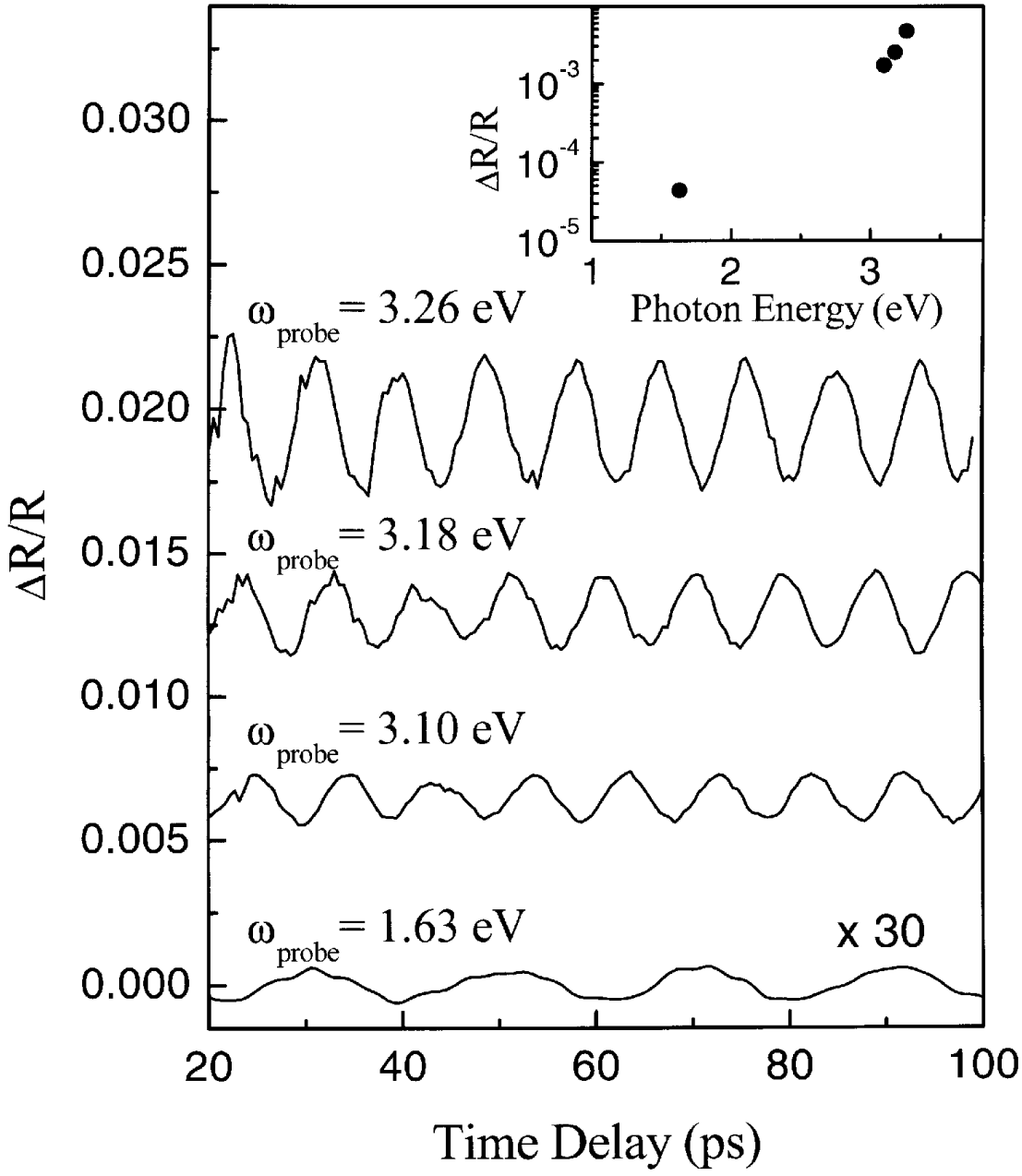

Figure 5–3: The oscillation traces of a SQW (III) at different probe energies. The pump energy is centered at 3.26 eV. The bottom curve has been magnified 30 times. The inset shows the oscillation amplitude as a function of probe photon energy on a logarithmic scale.

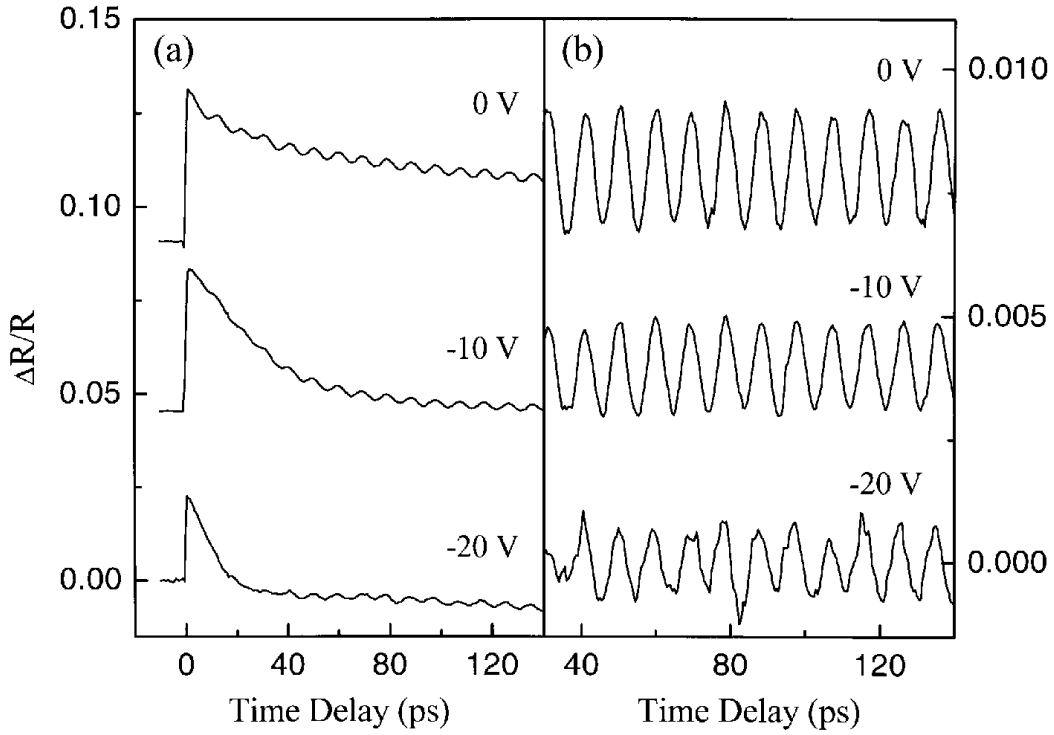

Figure 5–4: Pump-probe differential reflectivity for the blue LED structure (type IV). (a) External bias varies at a pump energy of 3.17 eV. The decay time of the background signal is drastically reduced as the bias increases. (b) The oscillatory amplitude does not change much with bias.

1 ps due to ultrafast tunneling [bottom curve of Fig. 5–4(a)], it implies that once the source that modulates the experimentally observed reflectivity is launched by the sub-picosecond generation of carriers, the remaining carriers do little to affect the source. This suggests that the reflectivity oscillation is due to the strain pulse which is generated at short times once the pump excites the carriers and modulates the lattice constant.

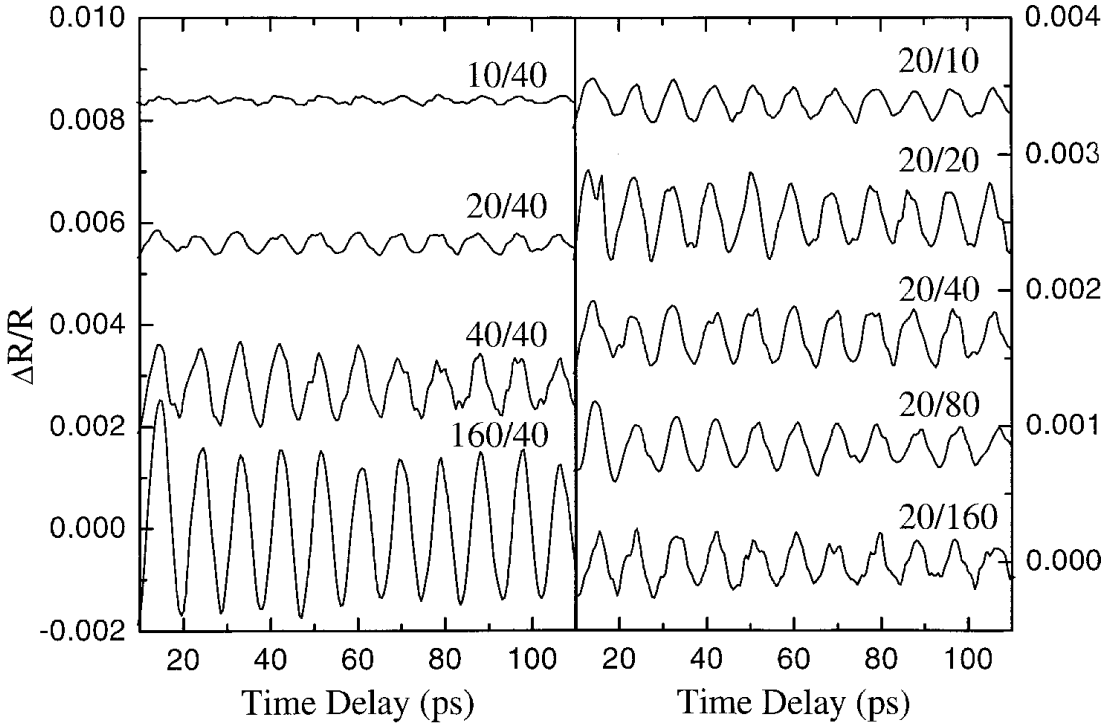

Figure 5–5: The oscillatory component of the pump-probe differential transmission traces of DQW's (II) at 3.22 eV. The left figure shows the well width dependence and the right figure shows the barrier width dependence.

Fig. 5–5 shows the well- and barrier-dependent acoustic phonon differential reflectivity oscillations in the type II DQW samples (see Fig. 5–1(b)) at a pump energy of 3.22 eV. The amplitude increases as the well width increases. However, the oscillation amplitude of the differential reflectivity doesn't change much with the barrier width. This means that the generation of the acoustic phonons is due

to the InGaN layer (well) and not GaN layer (barrier). This also verifies that the oscillation is due to the strain in InGaN layer.

Interesting results are seen in the long time behavior of the reflectivity oscillations shown in Fig. 5–6(a). The long time scale reflectivity oscillation is plotted for the epilayer (I), DQW (II), SQW (III), and the blue LED structure (IV) at 3.29 eV (below the GaN band gap). Astonishingly, the oscillation amplitude abruptly decreases within one cycle of an oscillation at a critical time which appears to scale with the thickness of the GaN layer in each sample. In addition, the slope of the GaN thickness vs. the critical time is very close to the known value of the sound velocity in GaN [inset of Fig. 5–6(a)] [26]. Fig. 5–6(b) shows results when the probe laser energy is changed to 3.44 eV which is above the GaN band gap. Then the laser probe is sensitive to coherent phonon oscillations only within an absorption depth of the surface. We see that the amplitude of the reflectivity oscillation exponentially decays with a decay time of 24.2 ps corresponding to a penetration depth in GaN of about 0.17 micron (=24.2 ps$\times$7000 m/s). The oscillation reappears at 260 ps for epilayer (I) and 340 ps for DQW (II). This is twice the critical time for the oscillations to disappear when the photon energy is 3.29 eV. This further shows that the probe pulse is sensitive to the coherent acoustic wave. The "echo" in the probe signal results from the partial reflection of the coherent phonon off the GaN/sapphire interface.

5.2 Theory

To explain the experimental results discussed in the last section, we have developed a theoretical model of the generation, propagation and detection of coherent acoustic phonons in strained GaN/InGaN heterostructures. The pump laser pulse generates a strain field that propagates through the sample which, in turn, causes a spatio-temporal change in the index of refraction. This change is responsible for the oscillatory behavior seen in the probe-field reflectivity in various

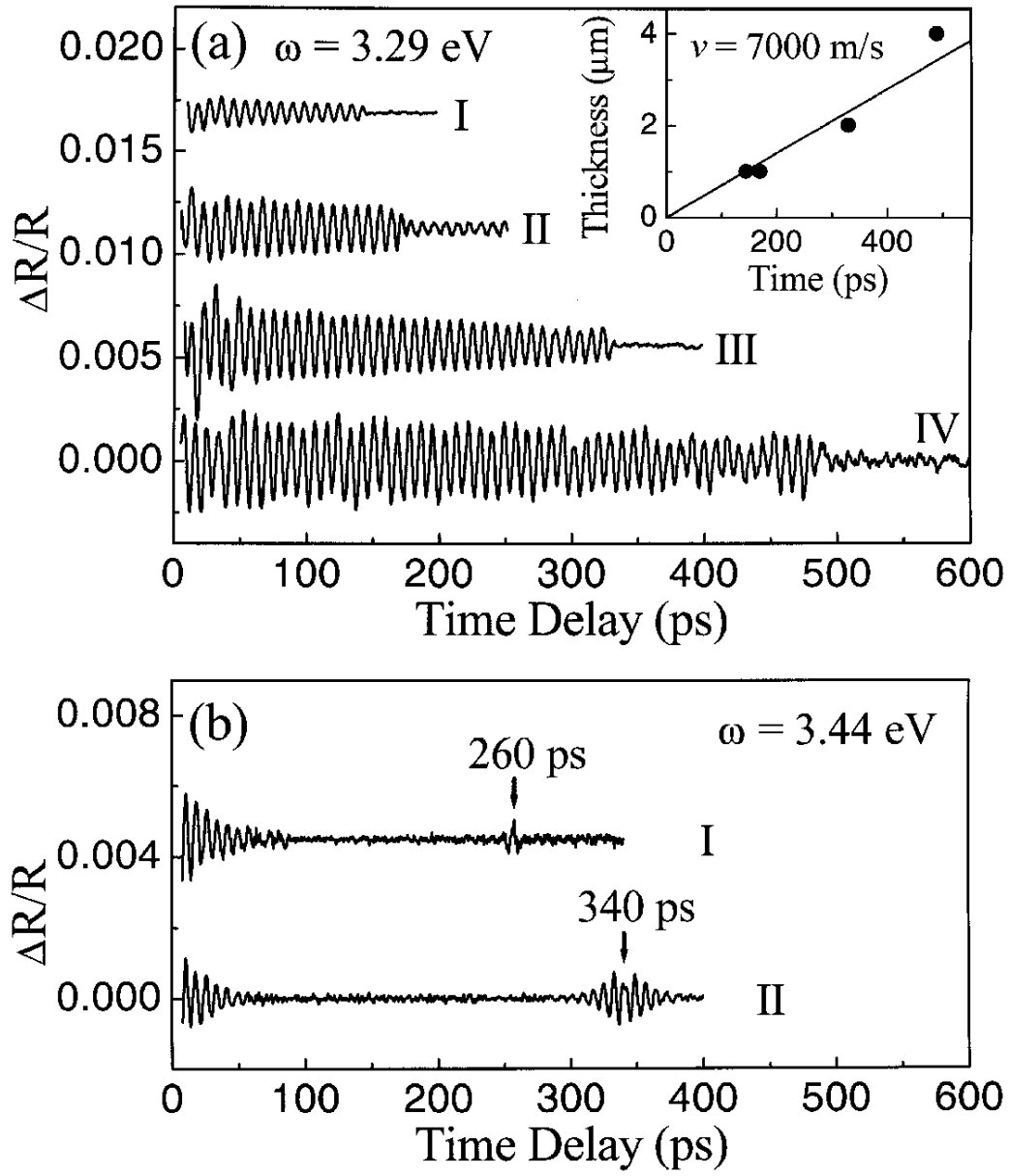

Figure 5–6: The long time-scale differential reflectivity traces. (a) Differential reflectivity oscillation traces of an epilayer (I), a DQW (II), a SQW (III), and blue LED structure (IV). The inset shows the GaN thickness between the sapphire substrate and InGaN active layer of the sample as a function of the die out time of the oscillations. The solid line indicates that the velocity of the wavepacket in the GaN medium is about 7000 m/s. (b) The oscillation traces of epilayer and DQW [top two curves in (a)]at 3.44 eV which corresponds to a probe laser energy above the band gap of GaN. Experimental data are from the group of D. S. Kim. [APL, **80** 4723, 2002]

semiconductor heterostructures. An approximate method of solving Maxwell's equations in the presence of spatio-temporal disturbances in the optical properties and obtaining the reflectivity of the probe field in thin films excited by picosecond pump pulses can be found in Thompsen [19].

The spatio-temporal disturbance of the refractive index is caused by the propagating coherent phonon wavepackets. Thus, an essential ingredient in the understanding the probe reflectivity is a model for the generation and propagation of the very short strain pulse in the sample. Recently, a microscopic theory explaining the generation and propagation of such a strain pulse was reported by Sanders et al. [27, 46] where it was shown that propagating coherent acoustic phonon wavepackets are created by the nonequilibrium carriers excited by the ultrafast pump pulse. The acoustic phonon oscillations arise through the electron-phonon interaction with the photoexcited carriers. Both acoustic deformation potential and piezoelectric scattering were considered in the microscopic model. It was found that under typical experimental conditions, the microscopic theory could be simplified and mapped onto a loaded string model. Here, we use the string model of coherent phonon pulse generation to obtain the strain field seen by the probe pulse.

First, we solve Maxwell's equations to obtain the probe reflectivity in the presence of a generalized spatio-temporal disturbance of the index of refraction. Let $n_{\rm b}$ be the index of refraction without the strain which is real because initially the absorption can be neglected and let $\delta\tilde{n} = \delta n + i\kappa$ be the propagating change in the index of refraction due to the strain. When the effect of the change of the index of refraction is taken into account, the probe field with energy ω can be described by the following generalized wave equation

$$\frac{\partial^2 E(z,t)}{\partial z^2} + \frac{\omega^2}{c^2}[n_{\rm b} + \delta\tilde{n}(z,t)]^2 E(z,t) = 0 \tag{5.1}$$

where $E(z,t)$ is the probe field in the slowly varying envelope function approximation and ω is the central frequency of the probe pulse. Eq. (5.1) is obtained from Maxwell's equations assuming that the polarization response is instantaneous and that the probe pulse obeys the slowly varying envelope function approximation. Since $|\delta\tilde{n}| \ll n_{\rm b}$ under typical conditions, Eq. (5.1) can be cast into

$$\frac{\partial^2 E(z,t)}{\partial z^2} + (n_{\rm b}k)^2 E(z,t) = -\,2n_{\rm b}k^2\delta\tilde{n}(z,t)E(z,t) \tag{5.2}$$

where $k = \omega/c$ is the probe wavevector. To relate the change of the index of refraction to the strain field, $\eta(z,t) \equiv \partial U(z,t)/\partial z$, we assume $|\delta\tilde{n}| \ll n_{\rm b}$ and adopt the linear approximation [19]

$$\delta\tilde{n}(z,t) = \frac{\partial\tilde{n}}{\partial\eta}\eta(z,t). \tag{5.3}$$

We view Eq. (5.2) as an inhomogeneous Helmholtz equation and obtain the solution using the Green's function technique. The desired Green's function is determined by solving

$$\frac{\partial^2 G(z,z')}{\partial z^2} + (n_{\rm b}k)^2 G(z,z') = \delta(z-z') \tag{5.4}$$

and the result is

$$G(z,z') = -\frac{i}{2n_{\rm b}k}\exp\left(in_{\rm b}k|z-z'|\right). \tag{5.5}$$

Then, the solution to Eq. (5.2) can be written as

$$E(z,t) = E_{\rm h}(z,t) + \int_{-\infty}^{\infty} dz' G(z,z')\left\{-2n_{\rm b}k^2\ \delta\tilde{n}(z',t)\ E(z',t)\right\} \tag{5.6}$$

$$\approx E_{\rm h}(z,t) + \int_{-\infty}^{\infty} dz' G(z,z')\left\{-2n_{\rm b}k^2\ \delta\tilde{n}(z',t)\ E_{\rm h}(z',t)\right\} \tag{5.7}$$

where we have chosen the lowest Born series in the last line. In Eq. (5.7), $E_{\rm h}$ is the homogeneous solution which takes the form $E_{\rm h}(z,t) = \tilde{E}_{\rm h}(z,t)\exp\{i(n_{\rm b}kz-\omega t)\}$ for the probe pulse moving to the right in the sample without optical distortion.

We now apply this approximate solution to our structure where the interface between air and the sample is chosen at $z = 0$. In the air, where $z \leq 0$, there is an incident probe pulse traveling toward the sample as well as a reflected pulse. The electric field in the air, $E_<(z,t)$, can thus be written as the sum

$$E_<(z,t) = \tilde{E}_{\rm i}(z,t)\ e^{i(kz-\omega t)} + \tilde{E}_{\rm r}(z,t)\ e^{-i(kz+\omega t)} \tag{5.8}$$

where $E_{\rm i}(z,t)$ and $E_{\rm r}(z,t)$ are the slowly varying envelope functions of the incident and reflected probe fields, respectively. Inside the sample, $z \geq 0$, the solution is given as

$$\begin{aligned} E_>(z,t) &= E_{\rm h}(z,t) + \int_0^\infty dz' \exp\left(in_{\rm b}k(z'-z)\right) ik\ \delta\tilde{n}(z',t)\ E_{\rm h}(z',t) \\ &= \tilde{E}_{\rm t}(z,t)e^{i(n_{\rm b}kz-\omega t)} + \left\{\int_0^\infty dz' \exp\left(2in_{\rm b}kz'\right) ik\ \delta\tilde{n}(z',t)\right\} \tilde{E}_{\rm t}(z,t)e^{-i(n_{\rm b}kz+\omega t)} \qquad (5.9) \\ &= \tilde{E}_{\rm t}(z,t)e^{i(n_{\rm b}kz-\omega t)} + \mathcal{A}(n_{\rm b}k,t)\tilde{E}_{\rm t}(z,t)e^{-i(n_{\rm b}kz+\omega t)} \qquad (5.10) \end{aligned}$$

where we used $E_{\rm h}(z,t) = \tilde{E}_{\rm t}(z,t)\ \exp(i(n_{\rm b}kz - \omega t))$ in the second step, assuming that $\tilde{E}_{\rm t}(z,t)$ is nearly constant within the slowly varying envelope function approximation, and we define a reflected amplitude function

$$\mathcal{A}(n_{\rm b}k,t) \equiv \int_0^\infty dz'\ \exp\left(2in_{\rm b}kz'\right)\ ik\ \delta\tilde{n}(z',t). \tag{5.11}$$

The expression for the reflected amplitude function, $\mathcal{A}(n_{\rm b}k,t)$, in Eq. (5.9) says there is a frequency-dependent modulation of the amplitude in the reflected wave in the sample due to the propagating strain.

Having determined the waves on both sides of the interface, we can now calculate the reflectivity. We apply the usual boundary conditions to the slowly varying envelope functions and the results are written compactly as

$$\begin{pmatrix} -1 & 1+\mathcal{A} \\ 1 & n_{\rm b}(1-\mathcal{A}) \end{pmatrix} \begin{pmatrix} \tilde{E}_{\rm r} \\ \tilde{E}_{\rm t} \end{pmatrix} = \begin{pmatrix} \tilde{E}_{\rm i} \\ \tilde{E}_{\rm i} \end{pmatrix}. \tag{5.12}$$

We solve this equation to obtain

$$\frac{\tilde{E}_{\mathrm{r}}}{\tilde{E}_{\mathrm{i}}} = \frac{r_0 + \mathcal{A}}{1 + r_0\mathcal{A}} \approx r_0 + \mathcal{A} \tag{5.13}$$

where $r_0 = (1 - n_{\mathrm{b}})/(1 + n_{\mathrm{b}})$. To the same order, we find that $\tilde{E}_{\mathrm{t}}/\tilde{E}_i \approx t_0(1 - r_0\mathcal{A})$ where $t_0 = 2/(1 + n_{\mathrm{b}})$. It is now straightforward to calculate the differential reflectivity as

$$\frac{\Delta R}{R} = \frac{|r_0 + \Delta r|^2 - |r_0|^2}{|r_0|^2} \approx \frac{2}{r_0}\mathrm{Re}\mathcal{A}. \tag{5.14}$$

Finally, by substituting the linear law Eq. (5.3) into Eq. (5.11) and using Eq. (5.14) we get

$$\frac{\Delta R}{R} = \int_0^\infty dz\ \mathcal{F}(z,\omega)\ \frac{\partial U(z,t)}{\partial z} \tag{5.15}$$

where the sensitivity function, $\mathcal{F}(z,\omega)$, is defined as

$$\mathcal{F}(z,\omega) = -\frac{2k}{r_0}\left[\frac{\partial n}{\partial \eta}\sin(2n_{\mathrm{b}}kz) + \frac{\partial \kappa}{\partial \eta}\cos(2n_{\mathrm{b}}kz)\right] \tag{5.16}$$

In Eq. (5.15), the differential reflectivity is expressed in terms of the lattice displacement, $U(z,t)$, due to propagating coherent phonons. Sanders et al. [27, 46] developed a microscopic theory showing that the coherent phonon lattice displacement satisfies a driven string equation,

$$\frac{\partial^2 U(z,t)}{\partial t^2} - C_{\mathrm{s}}^2\ \frac{\partial^2 U(z,t)}{\partial z^2} = S(z,t), \tag{5.17}$$

where C_{s} is the LA sound speed in the medium and $S(z,t)$ is a driving term which depends on the photogenerated carrier density. The LA sound speed is related to the mass density, ρ, and the elastic stiffness constant, C_{33}, by $C_{\mathrm{s}} = \sqrt{C_{33}/\rho}$. The LA sound speed is taken to be different in the GaN/InGaN heterostructure and Sapphire substrate. For simplicity, we neglect the sound speed mismatch between the GaN and $\mathrm{In}_x\mathrm{Ga}_{1-x}\mathrm{N}$ layers.

The driving function, $S(z,t)$, is nonuniform and is given by

$$S(z,t) = \sum_{\nu} S_{\nu}(z,t), \tag{5.18}$$

where the summation index, ν, runs over carrier species, i.e., conduction electrons, heavy holes, light holes, and crystal field split holes, that are created by the pump pulse. Each carrier species makes a separate contribution to the driving function. The partial driving functions, $S_{\nu}(z,t)$, in piezoelectric wurtzite crystals depend on the density of the photoexcited carriers. Thus,

$$S_{\nu}(z,t) = \pm\frac{1}{\rho}\left\{a_{\nu}\frac{\partial}{\partial z} + 4\pi\frac{|e|\ e_{33}}{\epsilon_{\infty}}\right\}\rho_{\nu}(z,t), \tag{5.19}$$

where the plus sign is used for conduction electrons and the minus sign is used for holes. Here $\rho_{\nu}(z,t)$ is the photogenerated electron or hole number density, which is real and positive, ρ is the mass density, a_{ν} are the deformation potentials, e_{33} is the piezoelectric constant, and ϵ_{∞} is the high frequency dielectric constant.

To be more specific, we will consider a SQW sample of the type shown in Fig. 5–1(c). We adopt a simple model for photogeneration of electrons and holes in which the photogenerated electron and hole number densities are proportional to the squared ground state particle in a box wavefunctions. The exact shape of the electron and hole number density profile is not critical in the present calculation since all that really matters is that the electrons and holes be strongly localized. The carriers are assumed to be instantaneously generated by the pump pulse and are localized in the $In_xGa_{1-x}N$ quantum well. Having obtained a model expression for $\rho_{\nu}(z,t)$, it is straightforward to obtain $S(z,t)$ using Eqs. (5.18) and (5.19).

To obtain $U(z,t)$, we solve driven string equations in the GaN epilayer and the Sapphire substrate, namely

$$\frac{\partial^2\ U(z,t)}{\partial t^2} - C_0^2\ \frac{\partial^2\ U(z,t)}{\partial z^2} = S(z,t) \qquad (0 \le z \le L) \tag{5.20a}$$

and

$$\frac{\partial^2 U(z,t)}{\partial t^2} - C_1^2 \frac{\partial^2 U(z,t)}{\partial z^2} = 0 \qquad (L \le z \le Z_{\rm s}) \tag{5.20b}$$

where C_0 and C_1 are LA sound speeds in the GaN and Sapphire substrate, respectively. In Eq. (5.20b), the Sapphire substrate has finite thickness. To simulate coherent phonon propagation in an infinite Sapphire substrate, $Z_{\rm s}$ in Eq. (5.20b) is chosen large enough so that the propagating sound pulse generated in the GaN epilayer does not have sufficient time to reach $z = Z_{\rm s}$ during the simulation. If T_{sim} is the duration of the simulation, this implies $Z_{\rm s} \ge L + C_1\, T_{sim}$.

Equations (5.20a) and (5.20b) are solved subject to initial and boundary conditions. The initial conditions are

$$U(z,0) = \frac{\partial U(z,0)}{\partial t} = 0. \tag{5.21}$$

At the GaN-air interface at $z = 0$, we assume the free surface boundary condition

$$\frac{\partial U(0,t)}{\partial z} = 0 \tag{5.22a}$$

since the air exerts no force on the GaN epilayer. The phonon displacement and the force per unit area are continuous at the GaN-Sapphire interface so that

$$U(L-\epsilon,t) = U(L+\epsilon,t) \tag{5.22b}$$

and

$$\rho_0\, C_0^2 \frac{\partial U(L-\epsilon,t)}{\partial z} = \rho_1\, C_1^2 \frac{\partial U(L+\epsilon,t)}{\partial z}. \tag{5.22c}$$

The boundary condition at $z = Z_{\rm s}$ can be chosen arbitrarily since the propagating sound pulse never reaches this interface. For mathematical convenience, we choose the rigid boundary condition

$$U(Z_{\rm s},t) = 0. \tag{5.22d}$$

To obtain $U(z,t)$ for general $S(z,t)$, we first need to find the harmonic solutions in the absence of strain, i.e. $S(z,t) = 0$. The harmonic solutions are taken to be

$$U_n(z,t) = W_n(z)\ e^{-i\omega_n t} \qquad (\ \omega_n \geq 0\ ) \tag{5.23}$$

and it is easy to show that the mode functions, $W_n(z)$, satisfy

$$\frac{d^2W_n(z)}{dz^2} + \frac{\omega_n^2}{C_0^2}W_n(z) = 0 \qquad (\ 0 \leq z \leq L\ ) \tag{5.24a}$$

and

$$\frac{d^2W_n(z)}{dz^2} + \frac{\omega_n^2}{C_1^2}W_n(z) = 0 \qquad (\ L \leq z \leq Z_{\rm s}\ ) \tag{5.24b}$$

Applying the boundary conditions from Eq. (5.22) we obtain the mode functions

$$W_n(z) = \begin{cases} \cos\left(\omega_n z/C_0\right) & \text{if } \ 0 \leq z \leq L \\ B_n\ \sin\left(\omega_n(Z_{\rm s}-z)/C_1\right) & \text{if } \ L \leq z \leq Z_{\rm s} \end{cases} \tag{5.25a}$$

with

$$B_n = \frac{\cos\left(\omega_n L/C_0\right)}{\sin\left(\omega_n(Z_{\rm s}-L)/C_1\right)}. \tag{5.25b}$$

The mode frequencies, ω_n, are solutions of the transcendental equation

$$\frac{1}{\rho_0 C_0}\cot\left(\frac{\omega_n L}{C_0}\right) = \frac{1}{\rho_1 C_1}\tan\left(\frac{\omega_n(Z_{\rm s}-L)}{C_1}\right) \tag{5.26}$$

which we solve numerically to obtain the mode frequencies, ω_n $(n = 0, 1, 2, ...)$. The index, n, is equal to the number of nodes in the mode functions, $W_n(z)$.

A general displacement can be expanded in terms of the harmonic modes as

$$U(z,t) = \sum_{n=0}^{\infty}\ q_n(t)\ W_n(z). \tag{5.27}$$

Substituting Eq. (5.27) for $U(z,t)$ into Eq. (5.20) and taking the initial conditions from Eq. (5.21) into account, we find that the expansion coefficients, $q_n(t)$, satisfy a

driven harmonic oscillator equation

$$\ddot{q}_n(t) + \omega_n^2 \; \dot{q}_n(t) = Q_n(t), \tag{5.28}$$

subject to the initial conditions $q_n(0) = \dot{q}_n(0) = 0$. The harmonic oscillator driving term $Q_n(t)$ is given by

$$Q_n(t) = \frac{\int_0^{Z_s} dz \; W_n(z) \; S(z,t)}{\int_0^{Z_s} dz \; W_n(z)^2}. \tag{5.29}$$

In our simple displacive model for photogeneration of carriers, $S(z,t) = S(z) \; \Theta(t)$ where $\Theta(t)$ is the Heaviside step function. In this case, the lattice displacement is explicitly given by

$$U(z,t) = \sum_{n=0}^{\infty} \frac{S_n}{\omega_n^2}(\; 1 - \cos(\omega_n \; t) \;) \; W_n(z) \tag{5.30}$$

with S_n defined as

$$S_n = \frac{\int_0^{Z_s} dz \; W_n(z) \; S(z)}{\int_0^{Z_s} dz \; W_n(z)^2}. \tag{5.31}$$

Using the lattice displacement from Eq.(5.30), we obtain the time-dependent differential reflectivity at the probe frequency, ω, from Eq.(5.15). The result is

$$\frac{\Delta R}{R}(\omega, t) = \sum_{n=0}^{\infty} \frac{S_n}{\omega_n^2}(\; 1 - \cos(\omega_n \; t) \;) \; R_n(\omega) \tag{5.32}$$

where

$$R_n(\omega) = \int_0^{Z_s} dz \; \mathcal{F}(z,\omega) \; \frac{dW_n(z)}{dz}. \tag{5.33}$$

can be evaluated analytically.

With the above formalism, we solve for the lattice displacement, $U(z,t)$, for a coherent LA phonon pulse propagating in a multilayer structure consisting of a 1.124 μm thick GaN epilayer grown on top of an infinitely thick Sapphire substrate with the growth direction along z. We take the origin to be at the GaN-air interface and the GaN-Sapphire interface is taken to be at $z = L = 1.124$ μm. We assume that carriers are photogenerated in a single 240 Å thick $In_xGa_{1-x}N$

quantum well embedded in the GaN layer 0.1 μm below the GaN-air interface and 1 μm above the Sapphire substrate. Our structure thus resembles the SQW sample shown in Fig. 5–1(c). In the GaN epilayer, we take $C_{33} = 379$ GPa and $\rho_0 = 6.139$ gm/cm^3 [47] from which we obtain $C_0 = 7857$ m/s. For the Sapphire substrate, we take $C_{33} = 500$ GPa and $\rho_1 = 3.986$ gm/cm^3 [48] from which we find $C_1 = 11200$ m/s.

The results of our simulation are shown in Fig. 5–7. A contour map of the strain, $\partial U(z,t)/\partial z$, is shown in Fig. 5–7(a). We plot the strain as a function of the depth below the surface and the probe delay time. Photoexcitation of electrons and holes in the InGaN quantum well generates two coherent LA sound pulses traveling in opposite directions. The pulses are totally reflected off the GaN/air interface at $z = 0$ and are partially reflected at the Sapphire substrate at $z = 1.124$ μm. Approximately 95% of the pulse energy is transmitted and only 5% is reflected at the substrate. The speed of the LA phonon pulses is just the slope of the propagating wave trains seen in Fig. 5–7(a) and one can clearly see that the LA sound speed is greater in the Sapphire substrate.

From the strain the differential reflectivity can be obtained from Eq. (5.15). From Fig. 5–7(a), the strains, $\partial U(z,t)/\partial z$, associated with the propagating pulses are highly localized and travel at the LA sound speed. Each pulse contributes a term to the differential reflectivity that goes like

$$\frac{\Delta R}{R}(\omega,t) \sim \mathcal{F}(C_0 t,\omega) \propto \frac{\omega}{c}\sin\left(\frac{2n_{\rm b}\omega}{c}C_0 t + \phi\right) \tag{5.34}$$

The period of the oscillations of $\mathcal{F}$ depends on the probe wavelength, $\lambda = 2\pi c/\omega$, with the result that the observed differential reflectivity oscillates in time with period, $T = \pi c/(n_{\rm b}C_0\omega) = \lambda/(2n_{\rm b}C_0)$, where $n_{\rm b} = 2.4$ is the index of refraction, and $C_0 = 7857$ m/s is the LA sound speed in GaN. For $\lambda = 377$ nm ($\hbar\omega = 3.29$ eV), this gives us $T = 10$ ps. The sensitivity function, $\mathcal{F}(z,\omega)$, defined in Eq. (5.16)

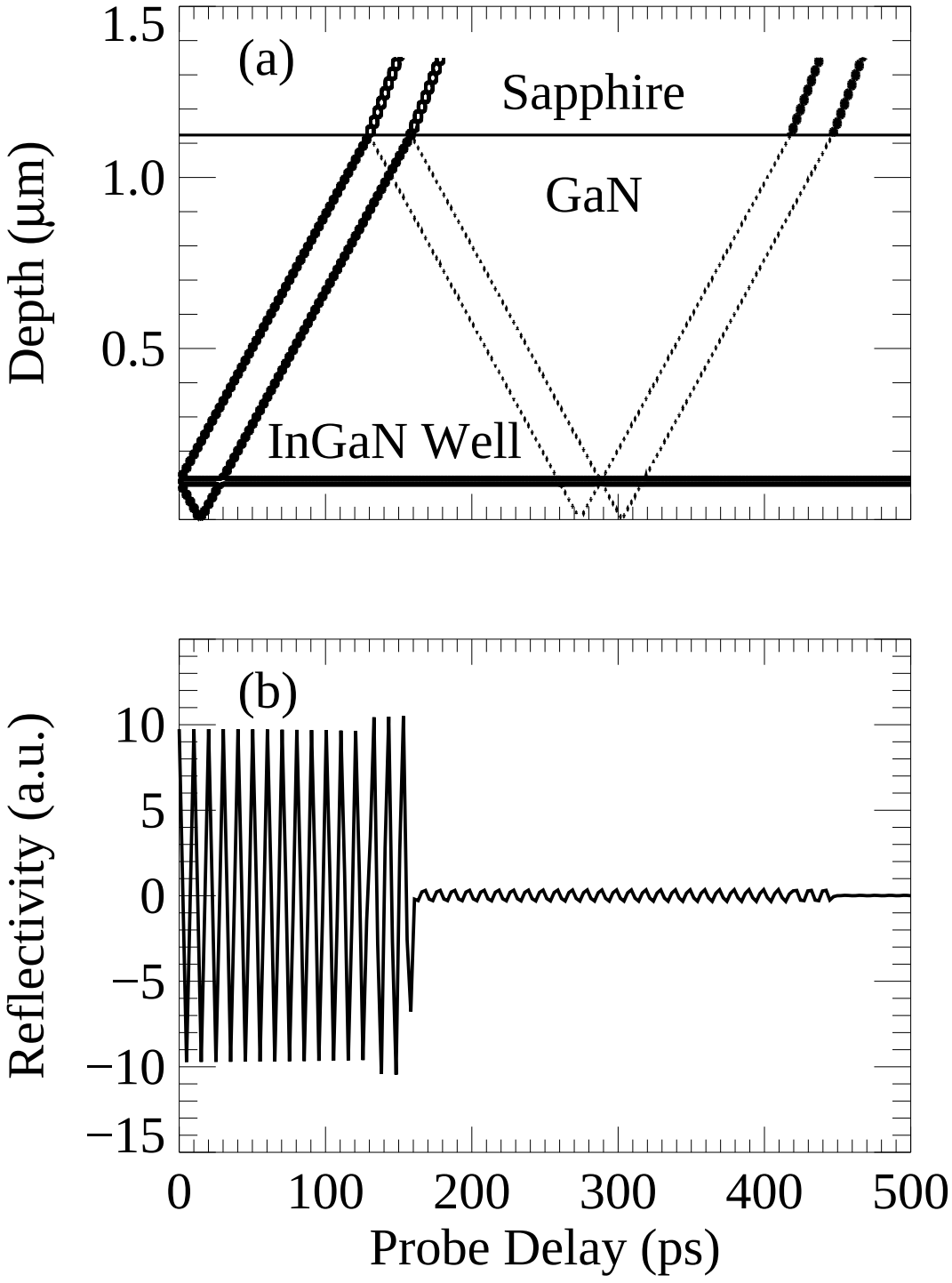

Figure 5–7: Generation and propagation of coherent acoustic phonons photogenerated in a single InGaN well embedded in a free standing 1.124μm GaN epilayer grown on top of a Sapphire substrate. In (a) a contour plot of the strain field, $\partial U(z,t)/\partial z$, is shown as a function of depth below the GaN-air interface and the probe delay. In (b), the resulting differential reflectivity induced by the strain field in (a) is shown as a function of the probe delay.

is an oscillating function in the GaN/InGaN epilayer and is assumed to vanish in the Sapphire substrate. Our computed differential reflectivity is shown in Fig. 5–7(b) for a probe wavelength of $\lambda = 377$ nm. We find that the reflectivity abruptly attenuates when the strain pulse enters the Sapphire substrate at $t = 170$ ps. The reflected strain pulses give rise to the weaker oscillations seen for $t > 170$ ps. These oscillations are predicted to continue until the reflected pulses are again partially reflected off the Sapphire substrate at $t = 430$ ps.

5.3 Simple model

Since the coherent oscillation observed in the differential reflectivity stems essentially from the strain pulse propagating into the layers, most phenomena can be understood by a simple macroscopic model that is presented in this section.

Instead of solving the loaded string equations for the strain to obtain a propagating disturbance in the refractive index, the propagating strain pulse at a given moment can be viewed as a thin strained layer in the sample, where the index of refraction is assumed to be slightly different from the rest of the sample. This situation is schematically depicted in Fig. 5–8 where a fictitious, thin GaN strained layer is located at z in the thick host GaN layer. The thickness of the strained layer, d, is approximately the width of the traveling coherent phonon strain field, $\partial U(z,t)/\partial z$, and is to be determined from the microscopic theory. From the last section, it was seen that the propagating strain field is strongly localized so that d is small. In the example of the last section, d is approximately equal to the quantum well width. Here we assume the strain pulse has been already created near the air/GaN interface and do not consider its generation procedure. We treat d as a phenomenological constant and also assume that the change in the index of refraction is constant. This strained GaN layer travels into the structure with the speed of the acoustic phonon wavepacket $C_0 = 7 \times 10^3\ m/s$, so the location of the stained layer is given as $z = C_0\tau$ where τ is the pump-probe delay time.

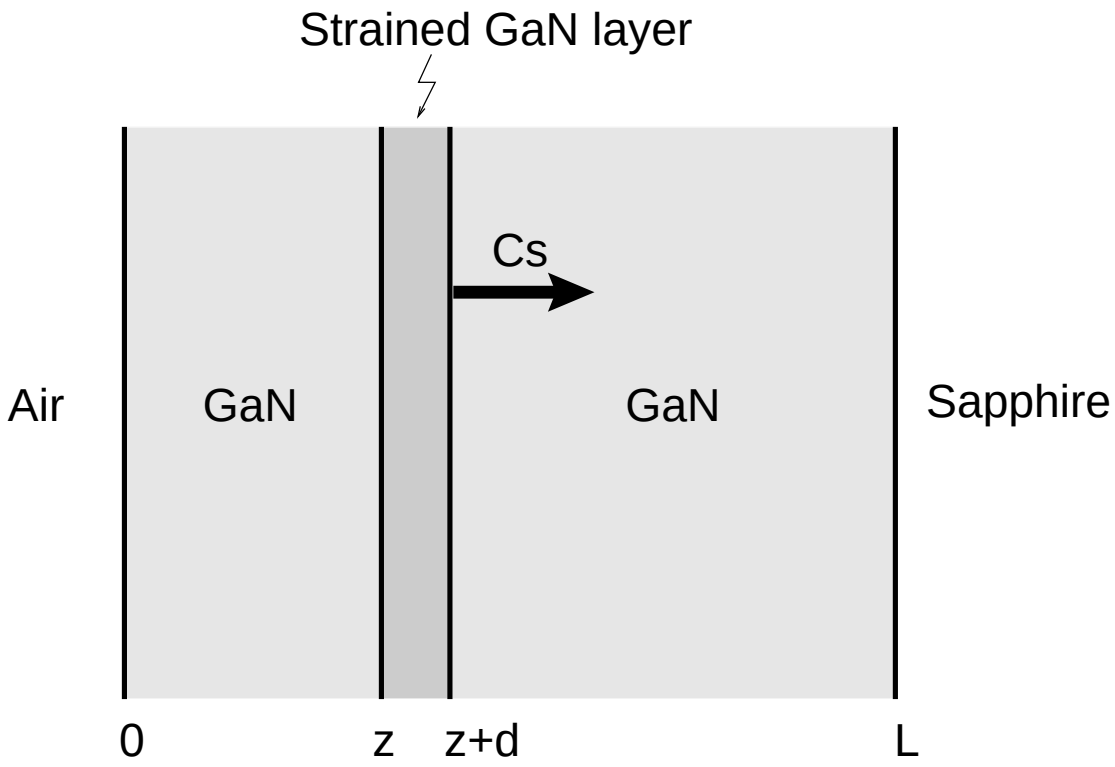

Figure 5–8: Propagating strained GaN layer in our simple model. The pump laser pulse creates a coherent acoustic phonon wavepacket in the InGaN layer near the air/GaN surface, which is modelled as a thin strained layer. The strained GaN layer propagates into the host GaN layer. The index of refraction in the strained layer is perturbed relative to the background GaN due to the strong strain induced piezoelectric field (Franz-Keldysh effect).

Within the slowly varying envelope function approximation, the solutions to the Maxwell equation can be written as plane waves in each region,

$$E_i(z,t) = a_i e^{ik_i z_i - i\omega t} + b_i e^{-ik_i z_i - i\omega t} \tag{5.35}$$

where E_i is the electric field in the left layer of ith interface, and a_i and b_i are the slowly varying amplitudes. The magnetic field is given by $B_i \sim \partial E_i/\partial z$. For a normally incident probe field, we apply the usual matching conditions on E and B to obtain

$$\begin{pmatrix} a_i \\ b_i \end{pmatrix} = \mathcal{M}_i \begin{pmatrix} a_{i+1} \\ b_{i+1} \end{pmatrix}, \tag{5.36}$$

where the transfer matrix, $\mathcal{M}_i$, is given explicitly as

$$\mathcal{M}_i = \tag{5.37}$$
$$\frac{1}{2}\begin{pmatrix} (1+\frac{k_{i+1}}{k_i})e^{i(k_{i+1}-k_i)z_i} & (1-\frac{k_{i+1}}{k_i})e^{-i(k_{i+1}+k_i)z_i} \\ (1-\frac{k_{i+1}}{k_i})e^{i(k_{i+1}+k_i)z_i} & (1+\frac{k_{i+1}}{k_i})e^{-i(k_{i+1}-k_i)z_i} \end{pmatrix}.$$

To apply this formula to our configuration, we normalize the incident amplitude to 1, let r be the reflected amplitude in the air, and impose the boundary condition that there is only a transmitted wave into the Sapphire substrate with amplitude t and no reflected wave from the GaN-Sapphire interface back into the GaN epilayer. The latter assumption is reasonable since the microscopic theory of the previous section shows that only 5% of the pulse energy is reflected from the interface between the GaN and the Sapphire substrate. The total reflection and transmission amplitudes r and t for the GaN epilayer structure are determined by

$$\begin{pmatrix} 1 \\ r \end{pmatrix} = \begin{pmatrix} \mathcal{M}_{11} & \mathcal{M}_{12} \\ \mathcal{M}_{21} & \mathcal{M}_{22} \end{pmatrix} \begin{pmatrix} t \\ 0 \end{pmatrix} \tag{5.38}$$

where $\mathcal{M} = \mathcal{M}_1\mathcal{M}_2\cdots\mathcal{M}_n$. The reflection amplitude is readily found to be

$$r = \mathcal{M}_{21}/\mathcal{M}_{11} = r_0 + \Delta r, \tag{5.39}$$

where r_0 is the background contribution without the strained layer. The total transmission amplitude is given as $t = 1/\mathcal{M}_{11}$. We can now numerically calculate the differential reflectivity by substituting r into Eq. (5.14).

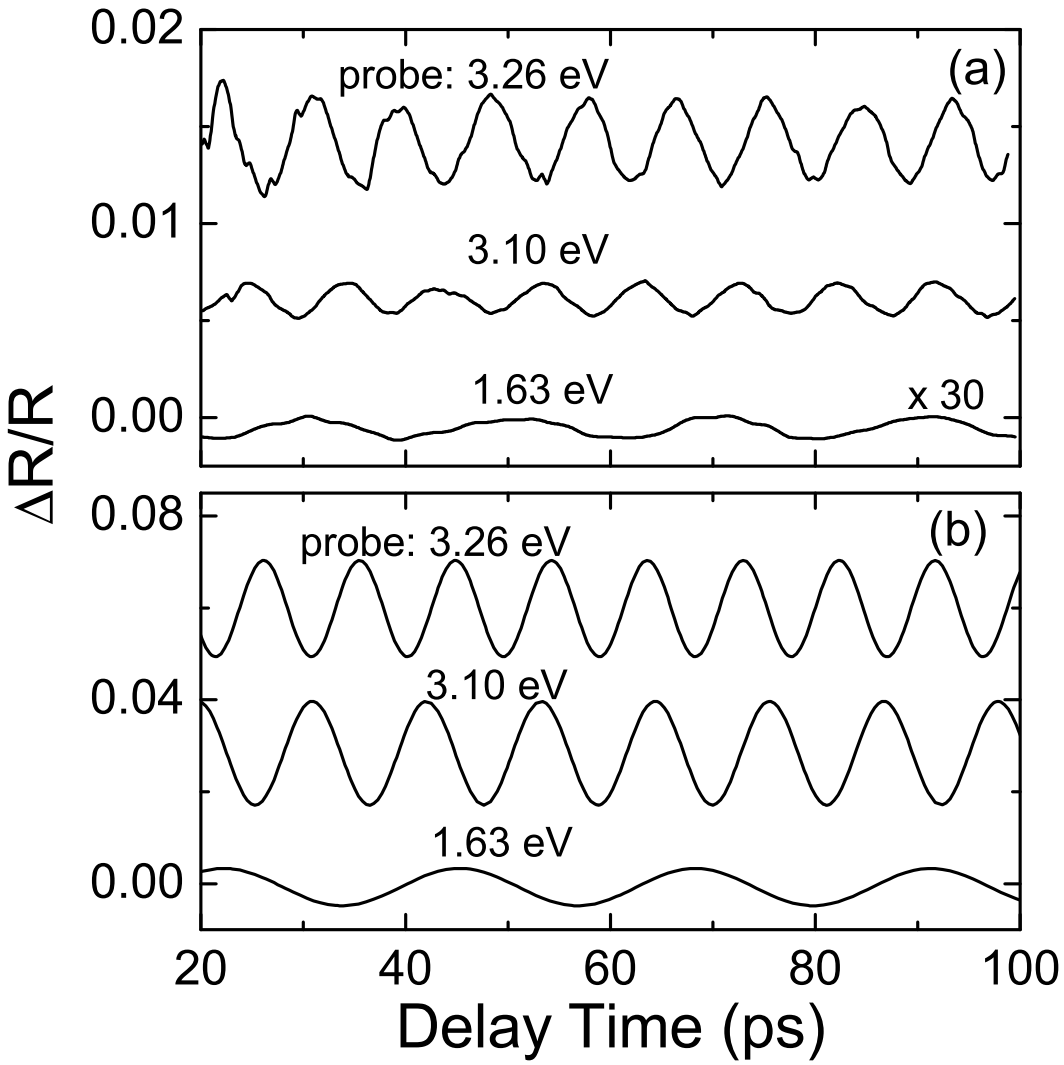

Figure 5–9: Differential reflection for different frequencies of the probe pulse. Plot (a) is experimental data and (b) comes from our calculations described in the text.

In Fig. 5–9 we compare our theoretical model with experimental results. In Fig. 5–9(a), the oscillatory part of the differential reflectivity is plotted as a function of probe delay for three values of the probe photon energy. This is the same data that was shown in Fig. 5–3 where it was seen that the oscillation period of the coherent phonon reflectivity oscillations are proportional to the probe wavelength. In Fig. 5–9(b), we plot the corresponding theoretical differential reflectivities obtained from Eq. (5.14). Comparing Figs. 5–9(a) and 5–9(b), we see that our geometrical optics model successfully explains the observed relation between the coherent phonon oscillation period and the probe wavelength. However, the calculated amplitudes of oscillation is inconsistent with the experimental data because in this case we have not taken into account of the change of index of refraction with respect to the probe wavelength which we will do later in the chapter.

In Fig. 5–10 we plot the differential reflectivity as a function of the probe delay for three different values of the change in the index of refraction in the strained layer, $\delta\tilde{n}$. As expected, the greater the change in index of refraction, the greater the amplitude of the differential reflectivity oscillations. A larger change in the index of refraction implies that more electron-hole pairs are excited near the air-GaN interface, which acts as a stronger source for the coherent acoustic phonon reflectivity oscillations. These results are qualitatively consistent with the experimental results shown in Fig. 5–2. In Fig. 5–11 we fix the change in the index of refraction, $\delta n = 0.01$, and varied the thickness of the strained layer, d. The result shows a larger amplitude for the differential reflection in wider strained layers, which is consistent with what was experimentally observed in Fig. 5–5.

Both Fig. 5–10 and Fig. 5–11 suggest that the amplitude of the differential reflectivity seems to increase monotonically with δn and d. All these features can be understood more easily using the single-reflection approximation to the full formula for the reflectivity in Eq. (5.39). Assuming the change in the index of refraction is

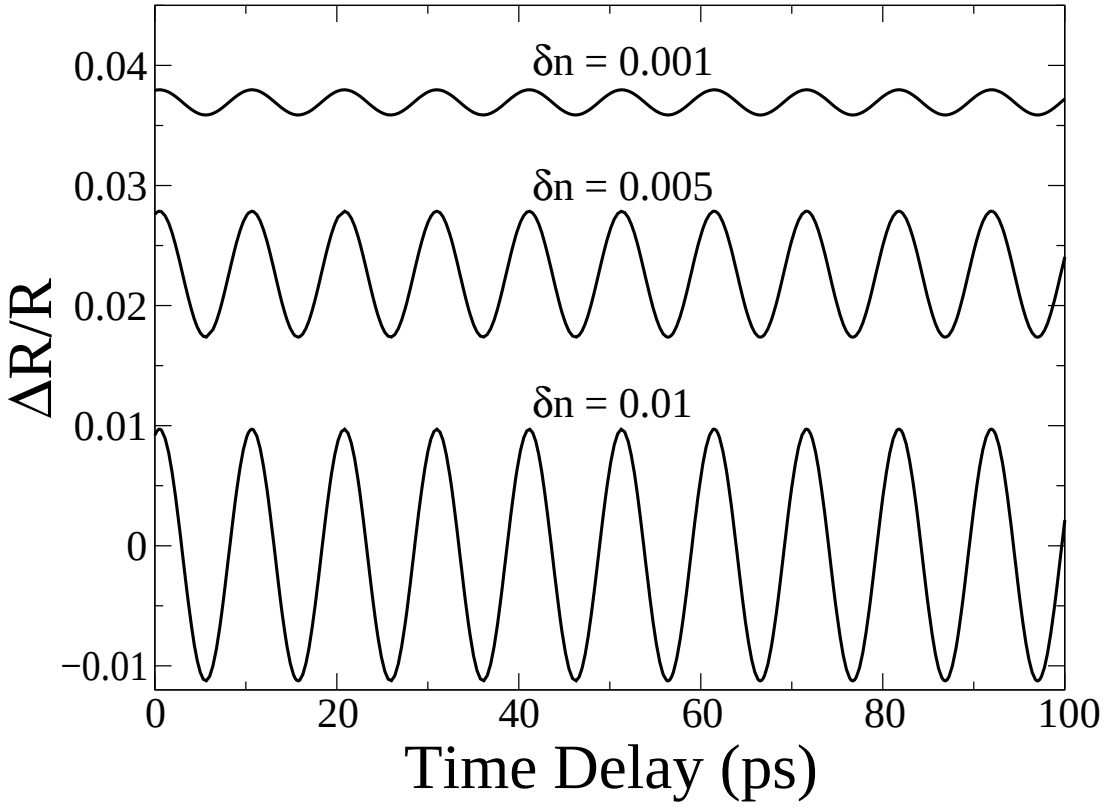

Figure 5–10: The differential reflection calculated numerically using Eq. (5.14) for three different values in the change in index of refraction. The parameters used are $n_{\mathrm{b}} = 2.65$, $\omega = 3.29\ eV$, $d = 30\ nm$, $L = 1\ \mu m$, and $C_{\mathrm{s}} = 7000\ m/s$. [Note that the curves are sifted to avoid overlapping.]

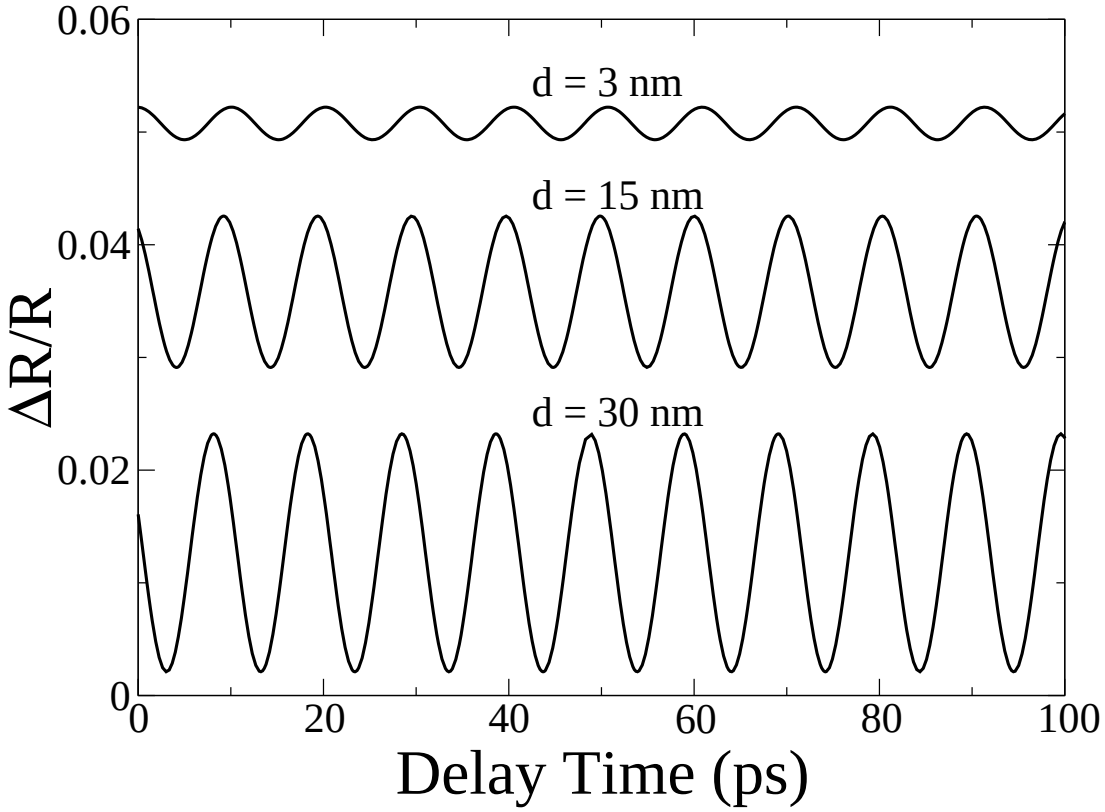

Figure 5–11: Calculated differential reflection for different values of the thickness of the strained GaN layer. The parameters are $n_{\rm b} = 2.65$, $\omega = 3.29\ eV$, $L = 1\ \mu m$, and $C_{\rm s} = 7000\ m/s$. The change in the index of refraction in the strained GaN layer was assumed to be $\delta n = 0.01$.

small, $|\delta\tilde{n}| \ll 1$, we may select contributions from only terms proportional to $\delta\tilde{n}$ in the infinite Fabry-Perot series for the total reflection amplitude. The relevant reflection processes selected are schematically depicted in Fig. 5–12. In this case the total reflection amplitude is given by the leading terms in the Fabry-Perot series

$$r = r_0 + r_1 + r_2 + \mathcal{O}\left(\delta\tilde{n}^2\right) \tag{5.40}$$

where r_0 is the background reflection amplitude, and the first order terms in $\delta\tilde{n}$ are

$$r_1 \propto -\, e^{2ikz}\delta\tilde{n}, \quad r_2 \propto e^{i2k(z+d)}\delta\tilde{n}. \tag{5.41}$$

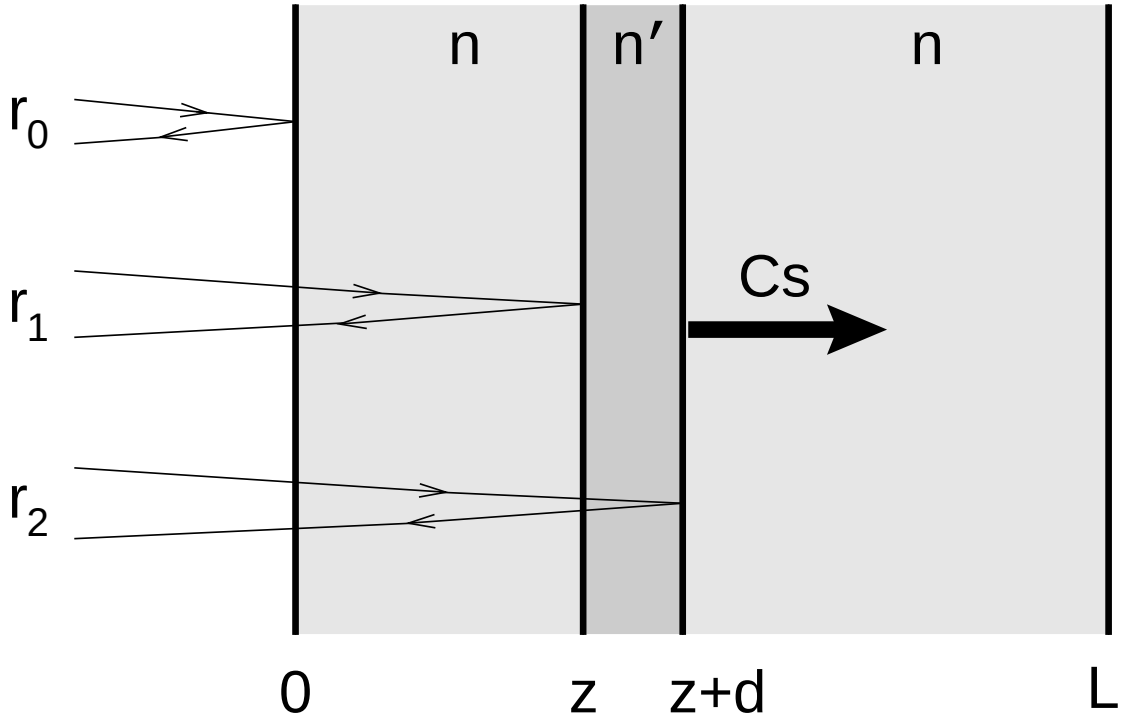

Figure 5–12: Schematic diagram of the single-reflection approximation in the Fabry-Perot reflection; where we have selected the processes only proportional to $\delta\tilde{n}$ $(= n' - n)$.

To linear order in $\delta\tilde{n}$, the differential reflectivity Eq. (5.14) becomes

$$\begin{aligned}\frac{\Delta R}{R} &= \frac{8\sin(kd)}{n^2-1}[\delta n\sin(2kz+kd)+\kappa\cos(2kz+kd)] \\ &= \frac{8\sin(kd)}{n^2-1}|\delta\tilde{n}|\sin(kd)\sin(2kz+\phi),\end{aligned} \tag{5.42}$$

where the phase ϕ is given by

$$\phi = kd + \arctan\left(\frac{\kappa}{\delta n}\right). \tag{5.43}$$

Note that for small values of kd, we can expand Eq. (5.42) in a Taylor series to obtain

$$\frac{\Delta R}{R} = \frac{8\ kd}{n^2-1}\left[\delta n\sin(2kz)+\kappa\cos(2kz)\right] \tag{5.44}$$

to first order in kd.

From Eq. (5.42) one can see that the amplitude of the oscillation scales linearly with the change of the real part and imaginary part of the index of refraction respectively.

Since the strain-pulse-front moves with the speed of sound, $z = C_0 t$, one can rewrite Eq. (5.42) as

$$\frac{\Delta R}{R}(\omega,t) \propto |\delta\tilde{n}|\sin(kd)\sin\left(2\pi\frac{t}{T}+\phi\right) \tag{5.45}$$

where $T = \pi c/(n_{\mathrm{b}}C_0\omega) = \lambda/(2C_0 n_{\mathrm{b}})$. Note that in the limit $kd \to 0$, Eq. (5.45) is equivalent to Eq. (5.34) of the microscopic theory described in the last section.

Equation (5.45) shows that the period of oscillations in the differential reflectivity is given by T, which is consistent with what was seen in the experiments. It also explains that the amplitude of the oscillation is proportional to the change in the index of refraction and that the amplitude modulates as $\sin(kd)$, so increasing linearly with the thickness of the strained layer as well as the probe frequency ω for $kd = n_{\mathrm{b}}(\omega/c)d \ll 1$.

The change of index of refraction in Eq. (5.45) comes from two effects. The first one which is small is the band gap change due to the deformational potential. The other one is the built-in piezoelectric field which leads to non-zero absorption below the band gap because of the Franz-Keldysh effect as shown in Fig. 5–13.

In general, it is difficult to determine the Franz-Keldysh field experimentally. Here we provide a way to estimate the order-of-magnitude of the built-in piezoelectric field from the differential reflectivity measurements. For a probe energy below band-gap, we read off the amplitude of the differential reflectivity from the experimental data. From this value, and an estimate for d based on information about the sample geometry, we obtain the change in the index of refraction which, in turn, gives an estimate for the absorption coefficient $\alpha(\omega)$ at the probe photon energy. In the Franz-Keldysh mechanism, $\alpha(\omega)$ is related to the piezoelectric field, F, via [12]

$$\alpha(\omega) \simeq \frac{1}{n_{\rm b}} \frac{\omega}{c} \frac{f}{E_g - \hbar\omega} \exp\left\{ -\frac{4}{3f} \left(\frac{(E_g - \hbar\omega)}{E_0 a_0^2} \right)^{3/2} \right\}. \tag{5.46}$$

Here $f = eF/(E_0 a_0^2)$ where $E_0 = 3.435$ eV and $a_0 = 39.68$ Å are the excitonic energy and length scales in GaN. From this formula, for instance, we estimate that a piezoelectric field on the order of $F \approx 0.93$ MeV/cm is responsible for a 1% change in the index of refraction.

In Fig. 5–13 we display the bulk absorption coefficient as a function of photon energy, $\hbar\omega$, in bulk GaN (dotted line) at a fixed piezoelectric field, $F = 0.93\ MV/cm$ (solid line). The inset shows the absorption coefficient at a fixed photon energy $\hbar\omega = 3.29\ eV$ as a function of the piezoelectric field, F. The change in the absorption at $\hbar\omega = 3.29\ eV$ (below the band-gap $E_g = 3.43\ eV$), can be used to estimate the piezoelectric field.

The corresponding changes in the real and imaginary parts of the dielectric function are shown in Fig. 5–14.

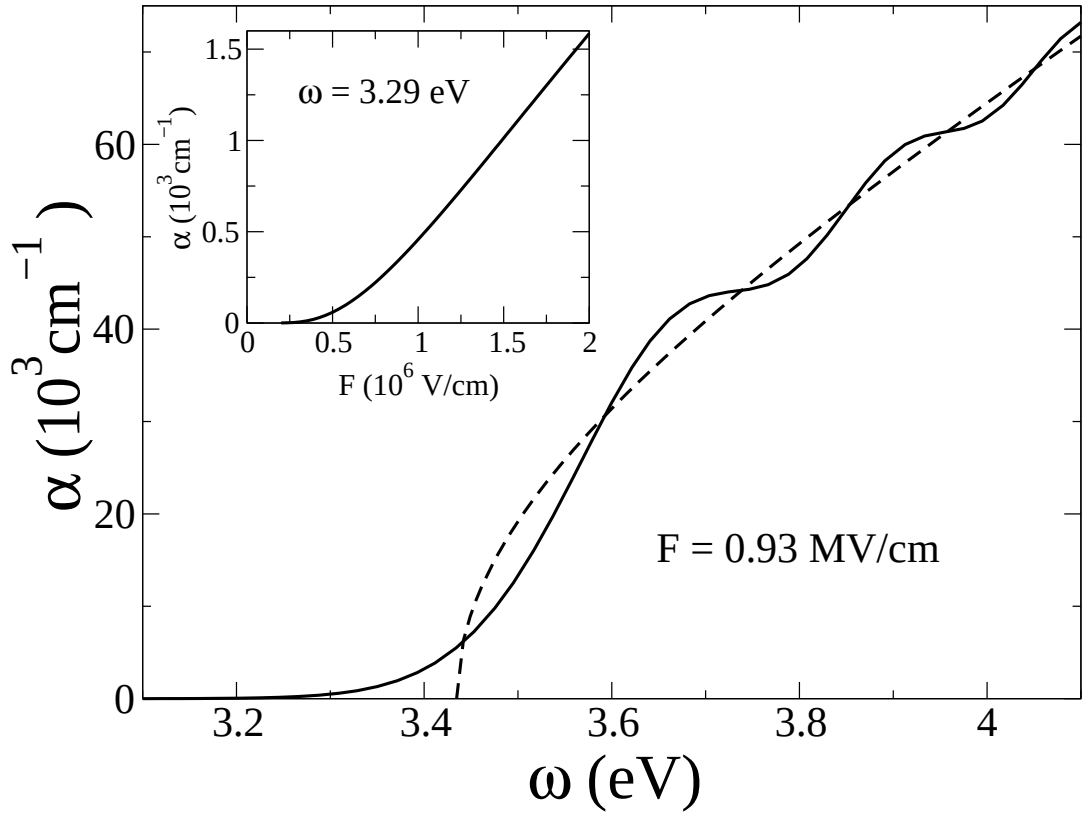

Figure 5–13: The absorption coefficient as a function of the probe energy. The absorption tail below the band gap $E_g = 3.43$ eV is due to the built-in Franz-Keldysh field. The dotted curve is the free-carrier absorption. The inset shows the absorption coefficient as a function of the piezoelectric field. The parameters used in this model calculation are: d=30 nm, n_b=2.65, a_0=4 nm, and E_0=15 meV.

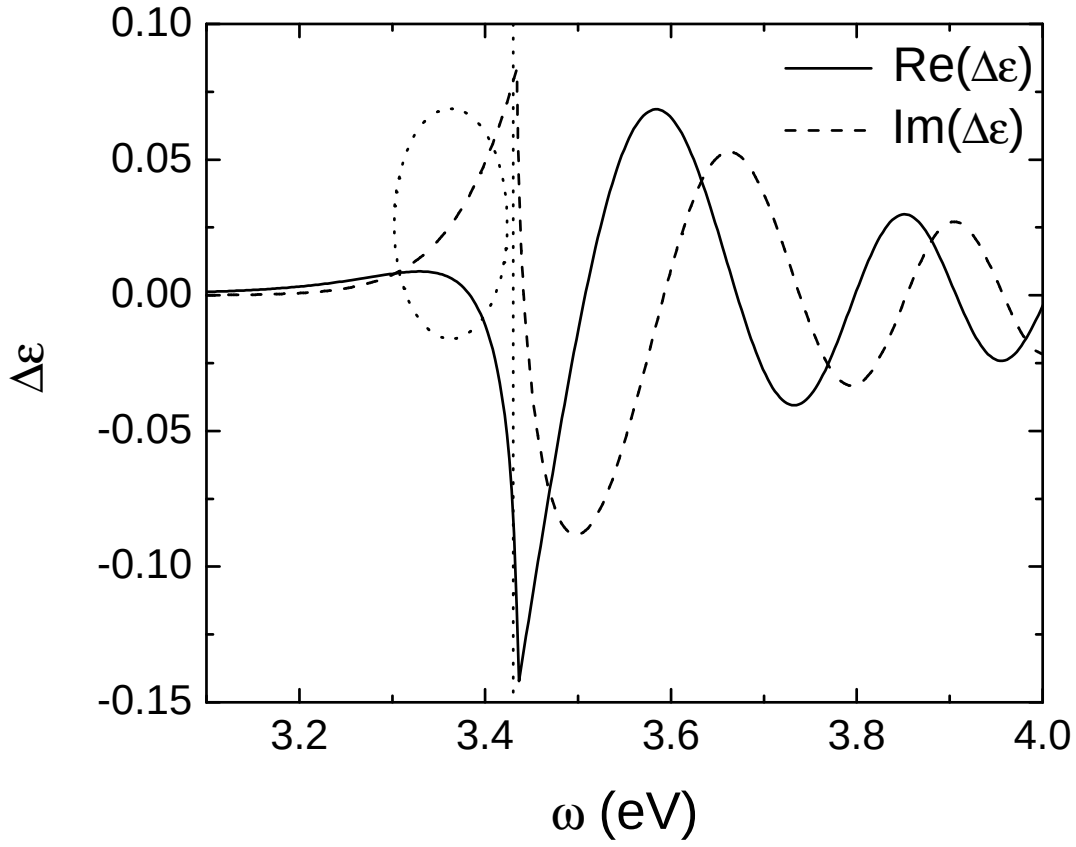

Figure 5–14: The change in the real and imaginary parts of the dielectric function in GaN as a function of the probe energy for the situation described in Fig. 5–13. The vertical dotted line at 3.43 eV is the band gap energy. Just below the band gap the change in the dielectric function is dominated by the imaginary part as indicated by the dotted oval.

5.4 Summary

We have presented a theory for the detection of a new class of large amplitude, coherent acoustic phonon wavepackets in femtosecond pump-probe experiments on $In_xGa_{1-x}N$/GaN epilayers and heterostructures. The InGaN/GaN structures are highly strained and at high In concentrations have large built in piezoelectric fields which account for the large amplitude of the observed reflectivity oscillations. This new class of coherent acoustic phonons is generated near the surface and propagates into the structure. The frequency of the reflectivity oscillations is found to be proportional to the frequency of the probe. These coherent phonon wavepackets can be used as a powerful probe of the structure of the sample.
We are able to model the generation and propagation of these acoustic phonon wavepackets using a simple string model which is derived from a microscopic model for the photogeneration and propagation of coherent acoustic phonon wavepackets in InGaN/GaN multiple quantum wells. Our model successfully predicts the observed dependence of the coherent phonon reflectivity oscillations on probe wavelength and epilayer thickness.

CHAPTER 6
CONCLUSION

I have developed a string model for coherent acoustic phonons in GaN/InGaN in GaN/InGaN multiple quantum wells which have very large built-in piezoelectric fields on the order of MeV/cm. It is a one dimensional wave equation for the lattice displacement, which describes the motion of a uniform string under a non-uniform forcing function. I also calculated differential transmission using the strain calculated from the string model. This model can be justified by a microscopic theory. Using this model, I can explain and predict many characteristics of experimentally observed oscaillations in differential reflection and transmission.

I have solved the string model using Green's function method to obtain the lattice displacement and other related physical quantities such as strain, energy density, energy, and the differential transmission. All these quantities have the oscillating property. The strain and energy density propagate in both directions along the superlattice growth axis z. The oscillations of energy and differential transmission have the same number of peaks as the number of the wells and they dies out because of the limited range of the multiple quantum well system.

I have applied the string model to the coherent control of the coherent acoustic phonons in GaN/InGaN MQWs. By using two forcing terms corresponding to two pump pulses, we can change three controllable parameters of the second forcing term with respect to the first one, the temporal phase, the spatial phase, and the relative amplitude. The temporal phase is the most effective control. We have shown both the temporally in phase constructive enhancement and out of phase destructive cancelation of the coherent phonon oscillations. To get better destructive effect the relative amplitude of the second forcing term should be small

than the first. In spatially out of phase cases the total forcing function will be zero after the starting time of the second forcing term, but there is a distinctive contrast between the temporally in phase and out of phase cases. In the former case the oscillation almost disappear, while in the latter case the oscillation persists with a dephasing time a half of the case when there is only one forcing term.

I also developed a theory for the detection of a new class of large amplitude, coherent acoustic phonon wavepackets in femtosecond pump-probe experiments on GaN/InGaN epilayers and heterostructures. The InGaN/GaN structures are highly strained and at high In concentrations have large built in piezoelectric fields which account for the large amplitude of the observed reflectivity oscillations. This new class of coherent acoustic phonons is generated near the surface and propagates into the structure. The frequency of the reflectivity oscillations is found to be proportional to the frequency of the probe. I modelled the generation and propagation of these acoustic phonon wavepackets using the simple string model developed for the coherent acoustic phonon in InGaN/GaN MQWs. By solving Maxwell's equations in the presence of spatio-temporal disturbances in the refractive index caused by the propagating coherent phonon wave packets, I can explain the sudden die out of the oscillations in the reflection. A simple macroscopic model treating the propagating strain pulse as a thin strained layer in the host material is developed, which successfully predicts the observed dependence of the coherent phonon reflectivity oscillations on probe wavelength and epilayer thickness. I also provided a way to estimate the order-of-magnitude of the bulit-in piezoelectric field from the differential reflection measurements.

Many speculations on possible applications of the coherent phonons have been discussed in the literature. I will give a few here with regards to the coherent acoustic phonons and wavepackets.

Coherent acoustic phonon dispersion relation in MQW/superlattice system can be used to obtain tunable oscillation frequencies ranging from low frequency up to several THz with one material system. The coherent control of coherent phonons may find application in the multiplexed generation of tailored THz signals. The energy dissipation by conventional diffusive heat transport could be improved or replaced by propagating nonthermal lattice excitation, which has potential application in future high power nitride field-effect transistors. The coherent phonon wavepackets can also be used in probing the semiconductor structures and in imaging surfaces and interfaces in nanostructures.

REFERENCES

[1] A. V. Kuznetsov and C. J. Stanton. Theory of coherent phonon oscillations in semiconductors. *Phys. Rev. Lett.*, 73:3243, 1994. 1, 4, 4.1, 4.2

[2] S. De Silvestri, J. G. Fujimoto, E. P. Ipen, E. B. Gamble, L. R. Williams, and K. A. Nelson. *Chem. Phys. Lett.*, 116:146, 1985. 1

[3] H. J. Zeiger, J. Vidal, T. K. Cheng, E. P. Ippen, G. Dresselhaus, and M. S. Dresselhaus. *Phys. Rev. B*, 45:768, 1992. 1, 3.1, 3.4

[4] A. G. Jolly S. Ruhman and K. A. Nelson. *J. Chem. Phys.*, 86:6563, 1987. 1

[5] J. Shah. *Ultrafast Spectroscopy of Semiconductors and Semiconductor Nanostructures*. Springer, Berlin, 1998. 1

[6] S. Nakamura, S. Pearton, and G. Fasol. *The Blue Laser Diode, the Complete Story*. Springer, Berlin, 2000. 1.1, 5

[7] J. C. Slater and G. F. Koster. *Phys. Rev.*, 94:1498, 1954. 1.1

[8] E. O. Kane. *J. Phys. Chem. Solids*, 1:249, 1957. 1.1

[9] Y. P. Varshni. *Physica (Amsterdam)*, 34:149, 1976. 1.1

[10] L. Vina, S. Logothetidis, and M. Cardona. *Phys. Rev. B*, 30:1979, 1984. 1.1

[11] I. Vurgaftman, J. R. Meyer, and L. R. Ram-Mohan. *J. Appl. Phys.*, 89:5815, 2001. 1.1

[12] H. Haug and S. W. Koch. *Quantum Theory of the Optical and Electronic Properties of Semiconductors*. World Scientific, Singapore, 1990. 1.2, 5.3

[13] E. M. Conwell. In Seitz, Turnbull, and Ehrenreich, editors, *Solid State Physics, Advances and Applications*. Academic Press, New York, 1967. 1.2

[14] John D. Jackson. *Classical Electrodynamics*. John Wiley & Sons, 1998. 2.1.2

[15] N. W. Ashcroft and N. D. Mermin. *Solid State Physics*. Harcourt College Publishers, Fort Worth, 1976. 2.2.2

[16] A. Lauberau and W. Kaiser. *Rev. Mod. Phys.*, 50:607, 1998. 3.1

[17] A. V. Kuznetsov and C. J. Stanton. Theory of coherent phonon oscillations in bulk gaas. In Frank Tsen, editor, *Ultrafast Phenomena in Semiconductors*, pages 353–403. Springer-Verlag, New York, 2001. 3.1, 3.1

[18] A.V. Kuznetsov and C.J. Stanton. *Phys. Rev. B*, 48, 1993. 3.2

[19] C. Thompsen, H. T. Grahn, H. J. Maris, and J. Tauc. *Phys. Rev. B*, 34:4129, 1986. 3.3, 5.1, 5.2, 5.2

[20] T.K. Cheng, J. Vidal, H.J. Zeiger, G. Dresselhaus, M.S. Dresselhaus, and E.P. Ippen. *Appl. Phys. Lett.*, 59:1923, 1991. 3.4

[21] T. Pfeifer, W. Kutt, H. Kurz, and R. Scholtz. *Phys. Rev. Lett.*, 69:3248, 1992. 3.4

[22] G.C. Cho, W. Kutt, and H. Kurz. Subpicosecond time-resolved coherent-phonon oscillations in gaas. *Phys. Rev. Lett.*, 65:764, 1990. 3.4

[23] C. Colvard, T. A. Grant, M. V. Klein, R. Merlin, R. Fischer, H. Morkoc, and A. C. Gossard. *Phys. Rev. B*, 31:2080, 1985. 4

[24] A. Yamamoto, T. Mishina, Y. Matsumoto, and M. Nakayama. *Phys. Rev. Lett.*, 73:740, 1994. 4, 5

[25] A. Bartels, T. Dekorsey, H. Kurz, and K. Kohler. *Phys. Rev. Lett.*, 82:1044, 1999. 4, 5

[26] C. K. Sun, J. C. Liang, and X. Y. Yu. *Phys. Rev. Lett.*, 84:179, 2000. 4, 5, 5.1

[27] G. D. Sanders, C. J. Stanton, and C. S. Kim. *Phys. Rev. B*, 64:235316, 2001. 4, 4.2, 4.2, 4.3, 5.2, 5.2

[28] S. L. Chuang and C. S. Chang. *Phys. Rev. B*, 54:2491, 1996. 4.1

[29] J. B. Jeon, B. C. Lee, M. Sirenko, K. W. Kim, and M. A. Littlejohn. *J. Appl. Phys.*, 82:386, 1997. 4.1

[30] W. C. Chow, S. W. Koch, and M. Sargent. *Semiconductor-Laser Physics*. Springer-Verlg, Berlin, 1994. 4.1

[31] C. K. Sun, Y. K. Huang, and J. C. Liang. *Appl. Phys. Lett.*, 78:1201, 2001. 4.4

[32] Ü. Özgür, C. W. Lee, and H. O. Everitt. *Phys. Rev. Lett.*, 86:5604, 2001. 4.4

[33] T. Feurer, J. C. Vaughan, and K. A. Nelson. *Science*, 299:374, 2003. 4.4

[34] T. Dekorsy, W. Kütt, T. Pfeifer, and H. Kurz. *Europhys. Lett.*, 23:223, 1993. 4.4

[35] M. Hase, K. Mizoguchi, H. Haima, and S.Nakashima. *Appl. Phys. Lett.*, 69:2474, 1996. 4.4

[36] A. Bartels, T. Dekorsy, and H. Kurz. *Appl. Phys. Lett.*, 72:2844, 1998. 4.4

[37] Ü. Özgür, C. W. Lee, and H. O. Everitt. *Phys. Status Solidi B*, 228:85, 2001. 5

[38] K. Mizoguchi, M. Hase, S. Nakashima, and M. Nakayama. *Phys. Rev. B*, 60:8262, 1999. 5

[39] P. Lefebvre, A. Morel, M. Gallart, T. Taliercio, J. Allgre, B. Gil, H. Mathieu, B. Damilano, N. grandjeau, and J. Massies. *Appl. Phys. Lett.*, 78:1252, 2001. 5

[40] T. Takeuchi, C. Wetzel, S. Yameguchi, H. Sakai, H. Amano, I. Akasaki, Y. Kaneko, S. Nakagawa, Y. Yamaoka, and N. Yamada. *Appl. Phys. Lett.*, 73:1691, 1998. 5

[41] J. S. Im, H. Kollmer, J. Off, A. Sohmer, F. Scholz, and A. Hangleiter. *Phys. Rev. B*, 57:R9435, 1998. 5

[42] S. F. Chichiba, A. C. Abane, M. S. Minsky, S. Keller, S. b. Fleichser, J. E. Bowers, E. Hu, U. K. Mishra, L. A. Coldren, S. P. DenBarrs, and T. Sota. *Appl. Phys. Lett.*, 73:2006, 1998. 5

[43] J. S. Yahng, Y. D. Jho, K. J. Yee, E. Oh, J. C. Woo, D. S. Kim, G. D. Sanders, and C. J. Stanton. *Appl. Phys. Lett.*, 80:4723, 2002. 5

[44] K. J. Yee, K. G. Lee, E. Oh, D. S. Kim, and Y. S. Lim. *Phys. Rev. Lett.*, 88:105501, 2002. 5.1

[45] Y. D. Jho, J. S. Yahng, E. Oh, and D. S. Kim. *Appl. Phys. Lett.*, 79:1130, 2001. 5.1

[46] G. D. Sanders, C. J. Stanton, and C. S. Kim. *Phys. Rev. B*, 66:079903, 2002. 5.2, 5.2

[47] O. Ambacher, J. Smart, J. R. Shealy, N. G. Weimann, K. Chu, M. Murphy, W. J. Schaff, L. F. Eastman, R. Dimitrov, L. Wittmer, M. Stutzmann, W. Rieger, and J. Hilsenbeck. *J. Appl. Phys.*, 85:3222, 1999. 5.2

[48] A. G. Every, G. L. Koos, and P. Wolfe. *Phys. Rev. B*, 29:2190, 1984. 5.2

BIOGRAPHICAL SKETCH

Rongliang Liu was born in Fengcheng, Jiangxi Province, People's Republic of China, on December 13, 1970. From 1989 to 1996 he studied in Shanghai Jiaotong University and received his B.S. and M.S. degree in summer of 1993 and spring of 1996 respectively. Then he worked as a programmer and system integration engineer in Shanghai Triman Company for two and a half years from 1996 to 1998. In the fall of 1998 he came to the United States and became a Gator. From then on he has been studying for a Ph.D. degree in the Department of Physics at the University of Florida.